

A metamorphic origin for Europa's ocean

Mohit Melwani Daswani¹, Steven Douglas Vance¹, Matthew Jason Mayne², and Christopher Glein³

¹Jet Propulsion Laboratory, California Institute of Technology

²Stellenbosch University

³Southwest Research Institute

November 23, 2022

Abstract

Europa likely contains an iron-rich metal core. For it to have formed, temperatures within Europa reached [?]1250 K. At that temperature, accreted chondritic minerals - e.g., carbonates and phyllosilicates - would partially devolatilize. Here, we compute the amounts and compositions of exsolved volatiles. We find that volatiles released from the interior would have carried solutes, redox-sensitive species, and could have generated a carbonic ocean in excess of Europa's present-day hydrosphere, and potentially an early CO₂ atmosphere. No late delivery of cometary water was necessary. Contrasting with prior work, CO₂ could be the most abundant solute in the ocean, followed by Ca²⁺, SO₄²⁻, and HCO₃⁻. However, gypsum precipitation going from the seafloor to the ice shell decreases the dissolved S/Cl ratio, such that Cl>S at the shallowest depths, consistent with recently inferred endogenous chlorides at Europa's surface. Gypsum would form a 3 - 10 km thick sedimentary layer at the seafloor.

A metamorphic origin for Europa's ocean

Mohit Melwani Daswani¹, Steven D. Vance¹, Matthew J. Mayne², Christopher R. Glein³

¹Jet Propulsion Laboratory, California Institute of Technology, Pasadena, CA, USA

²Department of Earth Sciences, Stellenbosch University, RSA

³Space Science and Engineering Division, Southwest Research Institute, San Antonio, TX, USA

Key Points:

- Devolatilization of early Europa's rocky interior may have generated a mildly acidic ocean
- Heating drove outgassing of up to 1–270 bar CO₂, perhaps as an early atmosphere since lost, or captured as a large clathrate reservoir
- Calcium, sulfate and carbonate salts precipitate at the seafloor, while chloride is abundant nearer the ice shell

Corresponding author: M. Melwani Daswani, mohit.melwani.daswani@jpl.caltech.edu

Abstract

Europa likely contains an iron-rich metal core. For it to have formed, temperatures within Europa reached ≥ 1250 K. At that temperature, accreted chondritic minerals—e.g., carbonates and phyllosilicates—would partially devolatilize. Here, we compute the amounts and compositions of exsolved volatiles. We find that volatiles released from the interior would have carried solutes, redox-sensitive species, and could have generated a carbonic ocean in excess of Europa’s present-day hydrosphere, and potentially an early CO_2 atmosphere. No late delivery of cometary water was necessary. Contrasting with prior work, CO_2 could be the most abundant solute in the ocean, followed by Ca^{2+} , SO_4^{2-} , and HCO_3^- . However, gypsum precipitation going from the seafloor to the ice shell decreases the dissolved S/Cl ratio, such that $\text{Cl} > \text{S}$ at the shallowest depths, consistent with recently inferred endogenous chlorides at Europa’s surface. Gypsum would form a 3–10 km thick sedimentary layer at the seafloor.

1 Introduction

Key to understanding the past and present habitability of Jupiter’s moon Europa is its composition and evolution. Europa hosts a $\gtrsim 100$ km deep liquid water ocean beneath its 3–30 km ice shell (e.g., Schubert et al., 2009). Water, solutes and possible oxidants needed to carry out metabolic processes (Gaidos et al., 1999; Hand et al., 2007) in Europa’s ocean were delivered through some combination of Europa’s accreted materials, release by chemical reactions, and subsequently by meteoritic or Io-genic influx.

Surface spectra were initially interpreted as hydrated surface salts from a sulfate-rich ocean (McCord et al., 1998), consistent with models of brine evolution in CI chondrite bodies (Kargel, 1991; Kargel et al., 2000; Zolotov & Shock, 2001). These models propose that Europa’s ocean evolved from a reduced NaCl-dominated composition to a more oxidized Mg-sulfate ocean as a result of: 1) thermodynamic equilibrium (including by hydrothermal activity) between the ocean and silicate interior, while reduced volatiles H_2 and CH_4 produced by water-rock interaction escaped (Zolotov & Shock, 2001, 2004; Zolotov & Kargel, 2009); and/or 2) large fluxes of surface-derived oxidants delivered into the ocean through overturning of the icy lithosphere (Hand et al., 2007; Pasek & Greenberg, 2012). Recently, however, a sulfate-rich ocean has been challenged because the interpretation of hydrated sulfate salts on the surface as an oceanic signature is not apparently consistent with more recent spectroscopic observations. These observations favor instead chloride salts on the most geologically disrupted surfaces; surface sulfate salts and hydrated sulfuric acid are interpreted as radiolytic end-products (Brown & Hand, 2013; Ligier et al., 2016; Trumbo et al., 2019, 2017; Fischer et al., 2016, but cf. Dalton et al., 2013). Alternatively, the ocean may have remained reduced and sulfidic if H_2 and CH_4 escape to space was limited (McKinnon & Zolensky, 2003).

Here, we use geochemical and petrologic models to assess whether planetary-scale thermal processes were responsible for the build-up of Europa’s ocean, and whether thermal evolution of the deep interior had a significant impact on the composition of the ocean. While plausible models of Europa have been constructed without a solid iron-rich core (Table S1), Europa’s high density and the inferred molten iron core in neighboring Ganymede (Bland et al., 2008) strongly suggest a high-temperature history for Europa’s interior (e.g., Greeley et al., 2004; Tobie et al., 2003, 2005) consistent with the formation of an iron-rich core (Anderson et al., 1998; Schubert et al., 2009; Moore & Hussmann, 2009). The decay of short-lived radionuclides in the accreting material could have heated the silicate interior sufficiently for partial melting to separate silicate and metal (c.f. Barr & Canup, 2008), or to at least expel volatiles, as occurred during the thermal metamorphism of some chondrites (e.g., Huss et al., 2006). Additionally, tidal dissipation during Europa’s orbital evolution may have affected early heating and differentiation of the

interior at a level comparable to radiogenic heating, but disentangling the influence of tidal dissipation from other early sources of heat is difficult (Hussmann & Spohn, 2004).

If Europa has an Fe-rich core, then a fraction of the deep interior was heated at least to the Fe \pm S eutectic temperature during differentiation. Accordingly, we hypothesize that prograde metamorphism (i.e., metamorphic changes caused by increasing temperature) and associated chemical reactions in the deep interior were the driving forces behind the ocean's formation and its composition. Based on this prograde assumption for Europa's evolution we: 1) establish a starting bulk composition of Europa immediately after accretion using an accretion model and compositional endmember scenarios; 2) use a Gibbs free energy minimization petrologic model to constrain a range of compositions for the changing ocean and deep interior during thermal excursions that could be caused by differentiation and/or thermal-orbital evolution (e.g., Tobie et al., 2005; Hussmann & Spohn, 2004); 3) use a chemical equilibrium model to calculate the composition of Europa's ocean after its generation by metamorphic reactions; and 4) constrain the present composition and interior structure of Europa by using mass balance and a 1D interior structure model consistent with Europa's gravitational coefficients and moment of inertia (MoI).

2 Methods

A flow chart summarizing the methods below is shown in Figure S1.

2.1 Bulk composition of the accreted body

To date, accretion models have suggested that Europa's bulk water content was derived from dust, pebbles or satellitesimals composed of non-hydrated silicate, plus varying amounts of water ice as a function of the (possibly migrating) position of the circumjovian snow line towards the late stages of accretion (e.g. Lunine & Stevenson, 1982; Makalkin et al., 1999; Canup & Ward, 2002, 2009; Ronnet et al., 2017), and/or capture and impact processing (e.g. Estrada et al., 2009; Mosqueira et al., 2010; Ronnet & Johansen, 2020). Both scenarios can lead to bodies consistent with models of the density gradient in the Galilean satellites and orbital properties, but rely on the fortuitous delivery of the exact mass of water as ice to explain the present-day hydrosphere (8–12 wt. %) despite widely different sizes ($\sim 10^{-3}$ – 10^5 m radius) and water ice contents (0.571–50 wt. %; Ronnet et al., 2017; Ronnet & Johansen, 2020) of the accreting particles. A recent reappraisal of hydrodynamic escape during accretion also yields water contents and densities consistent with present day observations (Bierson & Nimmo, 2020). The alternative that we explore here is one where variable amounts of water and volatiles are already present in Europa's accreting particles, based on the compositions of the proposed silicate-rich building blocks of Europa (i.e., chondrites) according to geophysical and geochemical models (Kargel et al., 2000; Zolotov & Shock, 2001; McKinnon & Zolensky, 2003; Kuskov & Kronrod, 2005; Zolotov & Kargel, 2009), and tie the subsequent thermal evolution of the accreted body to present-day Europa's spherical structure and gravitational moment of inertia. Chondrites contain various amounts of volatiles in minerals and organics (Table S2), the thermal processing of which could yield sufficient mass to form the present-day hydrosphere and still fulfill the geophysical constraints. (A present-day hydrated silicate interior for Europa is implausible given gravity and density measurements (Anderson et al., 1998; Sohl et al., 2002; Schubert et al., 2009; Kuskov & Kronrod, 2005; Vance et al., 2018), so subsequent thermal processing, nominally *differentiation* of the body will be necessary to meet the constraints.)

The composition and water mass fraction for the initial state of Europa before differentiation (*MC-Scale*) are estimated using a Monte Carlo accretion model (*AccretR*). Additionally, we consider two endmember compositions: one in which Europa accreted

114 entirely from CI carbonaceous chondrites (*EM-CI*), and another in which Europa ac-
 115 creted from CM chondrites only (*EM-CM*).

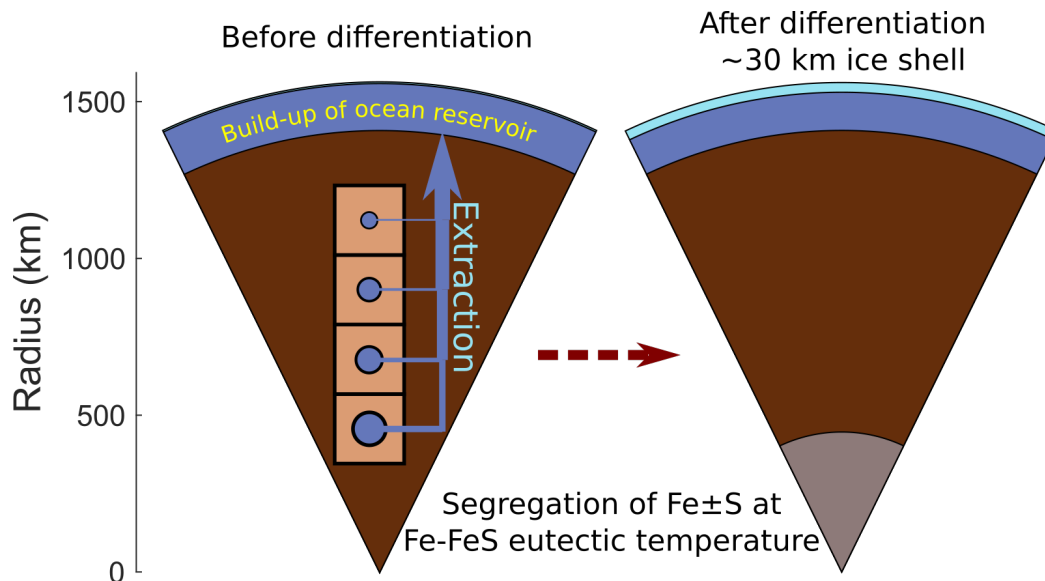
116 The models are insensitive to the mineralogy of the initial pebbles/satellitesimals
 117 and whether these were in thermochemical equilibrium prior to accretion (McKinnon &
 118 Zolensky, 2003) because our calculations of the subsequent geochemical evolution of these
 119 materials depend on the bulk composition, not the mineralogy. Nevertheless, hydrous
 120 minerals in planetesimal collisions are predicted to survive without substantial dehydra-
 121 tion (Wakita & Genda, 2019). Further details about the accretion and composition mod-
 122 els, and an additional model exploring a hypothetical reduced CI chondrite body are shown
 123 in Text S1 and Figures S4-S5, and the initial bulk compositions are summarized in Ta-
 124 ble S3.

125 **2.2 Ocean build-up by prograde metamorphism until the onset of core** 126 **formation**

127 To determine the mass and composition of an ocean produced during heating, de-
 128 volatilization, and differentiation of the deep interior, we use the `Perple_X` Gibbs free
 129 energy minimization program, which leverages experimental and modeled thermodynamic
 130 data, including non-aqueous solvents, and the Deep Earth Water model optimized for
 131 computing aqueous fluid speciation at high pressure (e.g. Connolly, 2005, 2009; Connolly
 132 & Galvez, 2018; Pan et al., 2013). For each initial bulk composition (§2.1), we model a
 133 0-dimensional heating pathway throughout the deep interior using `Rcrust` (Mayne et al.,
 134 2016), which provides an interface to model complex phase fractionation. We construct
 135 a 1D column spanning the radius of Europa discretized into a number of vertical cells
 136 that experience isobaric heating steps, and track the composition and mass of the equi-
 137 librium mineral-plus-volatile assemblage. At each heating step (ΔT), the Gibbs energy
 138 of the assemblage in each cell is minimized, resulting in a new equilibrium assemblage
 139 that depends on the heating step directly prior to it, but is not affected by the adjacent
 140 vertical cells.

141 We simulate the build-up of the ocean by imposing a limit on the fraction of volatiles
 142 retained in the assemblage for each heating step. That is, if fluids (except silicate melt,
 143 see below) are thermodynamically stable, a specified portion is irreversibly fractionated
 144 from the equilibrium assemblage of the particular cell to go into the growing ocean reser-
 145 voir (Fig. 1). As a limiting case, for each bulk composition computed (§2.1) we apply
 146 our thermodynamic models with a retained-to-extracted (R/E) fluid mass ratio of 0, i.e.,
 147 all fluids (including gases, liquids and their dissolved species) produced during heating
 148 are extracted from the interior. Buoyancy drives fluids upward, with transport being par-
 149 ticularly rapid in permeable materials in the direction of maximum compressive stress
 150 (e.g. Richard et al., 2007). Long-term retention of fluids at high pressure would lead to
 151 an unstable solution that is out of hydrostatic equilibrium. Thus, the only path for free
 152 low density fluids is up. This efficient extraction of volatiles from Europa’s interior is con-
 153 sistent with findings for the more limiting case of Titan (Leitner & Lunine, 2019) where
 154 a volatile-rich hydrosphere and atmosphere were formed endogenously (Miller et al., 2019;
 155 Néri et al., 2020) despite higher overburden pressure and gravity, and reduced tidal heat-
 156 ing, that would more efficiently prevent their escape.

157 A CI chondrite Europa’s bulk composition would contain water in excess of Eu-
 158 ropa’s present hydrosphere (§2.1), so for *EM-CI*, we also test the effect of varying the
 159 R/E fluid mass ratio, and carry out a model with a R/E ratio of 0.1 at each heating step,
 160 i.e., at each ΔT , thermodynamic equilibrium is computed, and subsequently 1 part of
 161 fluid is retained for 10 parts of fluid extracted. For *EM-CI* we also test the effect of a
 162 constant mass of fluid present in the rocky interior by retaining 5 wt. % fluid and ex-
 163 tracting any fluid in excess, similar to how magma chambers reach a critical size thresh-
 164 old prior to eruption (e.g. Townsend & Huber, 2020). (See Text S2 for model param-



172 **Figure 1.** Schematic of the thermodynamic + extraction + structure model to simulate the
 173 build-up of Europa's ocean from exsolved volatiles. After each heating step before differentiation,
 174 Gibbs energy minimization is carried out, resulting in an equilibrium assemblage in each cell
 175 (left figure). A portion of the fluid phase(s) is then extracted according to a specified rule (see
 176 §2.2), joins the ocean reservoir, and no longer affects the chemistry of the deep interior. Fe \pm S is
 177 extracted from the bulk composition from the deep interior once the interior reaches the Fe-FeS
 178 eutectic temperature (§2.3). Finally, Europa's structure is resolved (§2.4), here assuming a 30 km
 179 ice shell, requiring a temperature of 270.8 K at the ice-ocean interface.

165 eters and validation, and Table S4 for activity-composition models used.) As discussed,
 166 Europa likely contains a Fe-rich core, so the lowest maximum temperature the interior
 167 reached during prograde metamorphism is the melting temperature of the Fe-rich phase(s)
 168 that eventually formed the core (§2.3). Therefore, the resulting concentrations we report
 169 here represent a lower limit of the exsolved and extracted volatiles that formed Europa's
 170 proto-ocean. The onset of differentiation occurs at a temperature lower than the tem-
 171 perature of silicate melting (§2.3), hence silicate partial melting does not occur here.

180 2.3 Core composition

181 In our model we assume that prograde metamorphism proceeded at least up to the
 182 Fe-FeS eutectic temperature in order for core formation to proceed. Since this occurs at
 183 temperatures higher than volatile-releasing metamorphic reactions (see §2.2), we further
 184 assume that core formation does not sequester volatiles that would build the ocean. Our
 185 calculations are performed in the simplified Fe-S system as an initial approximation for
 186 an expected core composition, mass and density, until a future mission can constrain the
 187 deep interior composition of Europa from its seismic properties and improved gravity data.
 188 For further details on assumptions taken for modelled temperatures and the chemical
 189 system considered see Text S3.

190 2.4 Post-differentiation structure, mineralogy and geochemistry

191 We obtain our final predictions for Europa's interior structure after the formation
 192 of the ocean and differentiation using PlanetProfile, a program for constructing 1D

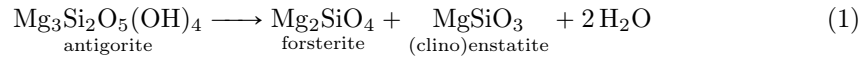
193 planetary structure models, in which the self-consistent gridded thermodynamic prop-
 194 erties from `Perple_X` and `Rcrust` are used as inputs (Vance et al., 2018). To construct
 195 the inputs, we first use `Rcrust` to perform isobaric heating simulations as described in
 196 §2.2 and Figure 1 to obtain the thermodynamic properties. We then remove the appro-
 197 priate Fe \pm S mass from the silicate layer for each model Europa to form a core with 24
 198 mass % sulfur (the minimum amount of sulfur in melt at the Fe-FeS eutectic within Eu-
 199 ropa, see §2.3) for *EM-CI*, *EM-CM* and *MC-Scale* after fluid extraction up to the Fe-
 200 FeS eutectic temperature (§2.2). Finally, we fold the separate silicate layer and Fe \pm S
 201 core (§2.3) thermodynamic properties into `PlanetProfile` and obtain structures con-
 202 sistent with Europa’s radius, density and MoI. Text S4 describes inputs and modifica-
 203 tions to `PlanetProfile` for this work. The results form a baseline against which space-
 204 craft observations may be compared to elucidate the effects of ~ 4.5 Gyr of orbital-ge-
 205 ologic history.

206 2.5 Ocean column composition

207 We use the bulk extracted ocean compositions and masses (§2.2) as inputs into geo-
 208 chemical model `CHIM-XPT` (Reed, 1998) to compute ocean depth dependent mineral-aque-
 209 ous solution-gas equilibria using the self-consistent thermodynamic database `SOLTHERM`,
 210 which includes thermodynamic properties of water and equilibrium constants up to 0.5 GPa.
 211 We carry out a 1D `CHIM-XPT` model for the bulk fluids extracted by prograde metamor-
 212 phism of *EM-CI*, *EM-CM*, and *MC-Scale* (§2.2), varying the pressure from the seafloor
 213 (200 MPa; Vance et al., 2018) up to a hypothetical ice-free surface. This way, we quan-
 214 tify gas saturation and mineral precipitation out of the primordial ocean (i.e., fraction-
 215 ation), and the effects on the water column’s composition, pH and redox potential. Fur-
 216 ther details about `CHIM-XPT` and validation of the model are found in Text S2.

217 3 Results and discussion

218 Prograde metamorphism up to the Fe-FeS eutectic temperature has the effect of
 219 dehydrating, dehydroxylating, decarbonizing and desulfurizing the deep interior, irre-
 220 versibly changing the mineralogy (e.g., Glein et al., 2018). The main volatile-releasing
 221 generalized reactions are:



224 Large amounts of volatiles are released at low temperature (< 300 K): the start-
 225 ing rock compositions (namely volatile-rich carbonaceous chondrites) are thermally un-
 226 equilibrated, so the thermodynamic model predicts that excess volatiles (mainly water
 227 and CH_4) and dissolved solutes are unbound from minerals and organics. At moderate
 228 temperatures (300–600 K), only small amounts of fluid are released because lizardite, antig-
 229 orite, chlorite and magnesite are stable; these are phyllosilicate or carbonate minerals
 230 with structurally bound water and OH^- , or CO_3^{2-} . At $\gtrsim 650$ K, antigorite and mag-
 231 nesite break down, releasing H_2O and CO_2 . Higher pressure stabilizes magnesite and antig-
 232 orite, whereas lower pressure favors their breakdown at that temperature. Analogous volatile-
 233 releasing reactions occur presently in Earth’s subducting oceanic plates, for example, which
 234 experience dewatering and decarbonization with increasing pressure and temperature (e.g.,
 235 Manthilake et al., 2016; Gorce et al., 2019). Further details about the pressures and tem-
 236 peratures of the reactions and the changing mineralogy along the prograde metamorphic
 237 path are found in Text S5 and Figures S12–S13.

238

3.1 Extracted fluid compositions and ocean masses

239

240

241

242

243

244

245

Prograde metamorphism of the *EM-CI* and *EM-CM* initial compositions supplies a fluid mass that exceeds the present ~ 10 wt. % hydrosphere for all tested R/E ratios. The *MC-Scale* composition however, is unable to supply sufficient fluid mass, despite a R/E ratio = 0, since the maximal water content of this composition (3.5 ± 0.6 wt %, assuming all H is in H₂O) falls short of Europa's present hydrosphere mass, indicating that additional water was co-accreted or delivered if Europa formed from the materials nearest to Jupiter ~ 4.5 Ga according to the MC accretion model (§2.1).

246

247

248

249

250

251

252

253

254

255

256

257

258

259

260

261

The pattern of volatile release at different pressures and temperatures is broadly similar for all prograde metamorphism models of the initial compositions tested. We focus on solutes and solvents from *EM-CM* shown in Fig. 2, and include additional subtleties of the exsolved fluid compositions in Text S5, Table S5 and Figures S6–S11. In all cases, the most significant contributors to the ocean reservoir mass are oxygen and hydrogen, as water (e.g., Fig. 2). Carbon is the third most abundant element comprising the ocean reservoir of the *EM-CI* and *EM-CM* models, particularly at relatively high temperatures where CO₂ becomes a major component, and acts as the solvent, in the fluid phase (Fig. 2) as a result of carbonate destabilization (see also §3.3). However, while carbon, hydrogen, oxygen, sulfur and calcium abundances in the exsolved ocean reservoirs of *EM-CI* and *EM-CM* are comparable, the total mass of silicon, sodium, magnesium, chlorine, potassium and aluminum extracted from *EM-CM* is significantly higher, and only the extracted mass of iron is lower after prograde metamorphism of *EM-CM* compared to *EM-CI*. For *MC-Scale*, the most abundant solutes in the extracted ocean are calcium and sulfur, especially exsolved at <650 K and >6 GPa in the form of CaSO₄, although some calcium is present as CaCl₂.

272

273

3.2 Composition of the ocean column, precipitated minerals and exsolved gases

274

275

276

277

278

279

280

281

282

Distinct ocean compositions from seafloor to surface (Fig. 3) result from isothermal 1D decompression CHIM-XPT models equilibrating the bulk compositions of the extracted fluids for *EM-CI*, *EM-CM* and *MC-Scale* (§3.1). In all cases, gypsum (CaSO₄) saturates and precipitates as pressure decreases. Additionally, for *EM-CM*, dolomite is stable throughout the water column, while for *MC-Scale*, dolomite is stable at < 30 MPa, which may correspond to a depth within the present ice shell (Fig. 3). (Since prograde metamorphism of the *MC-Scale* composition did not yield a sufficiently massive hydrosphere (§3.1), we consider the effects of compensating the difference with late delivery of cometary material in Text S7 and Fig. S15.)

291

292

293

294

295

296

297

298

299

Gypsum precipitation throughout the water column steadily decreases the S/Cl molar ratio with decreasing depth in all cases, such that the total concentrations of chlorine and sulfur become comparable ($\Sigma\text{Cl} \approx \Sigma\text{S}$) at shallow depths for *EM-CI* and *EM-CM* (Fig. 3), and chlorine exceeds sulfur at $\lesssim 124$ MPa for *EM-CI*. Similarly, the dissolved calcium concentration decreases as a result of gypsum precipitation, decreasing the Ca/Mg molar ratio with decreasing depth in all models. No Na- or K-bearing minerals saturate, so the Na/K molar ratio remains constant at all depths. In the limiting assumption of zero porosity, the globally averaged thickness of all mineral precipitates at Europa's seafloor is 2.7–9.5 km (Table 1).

300

301

302

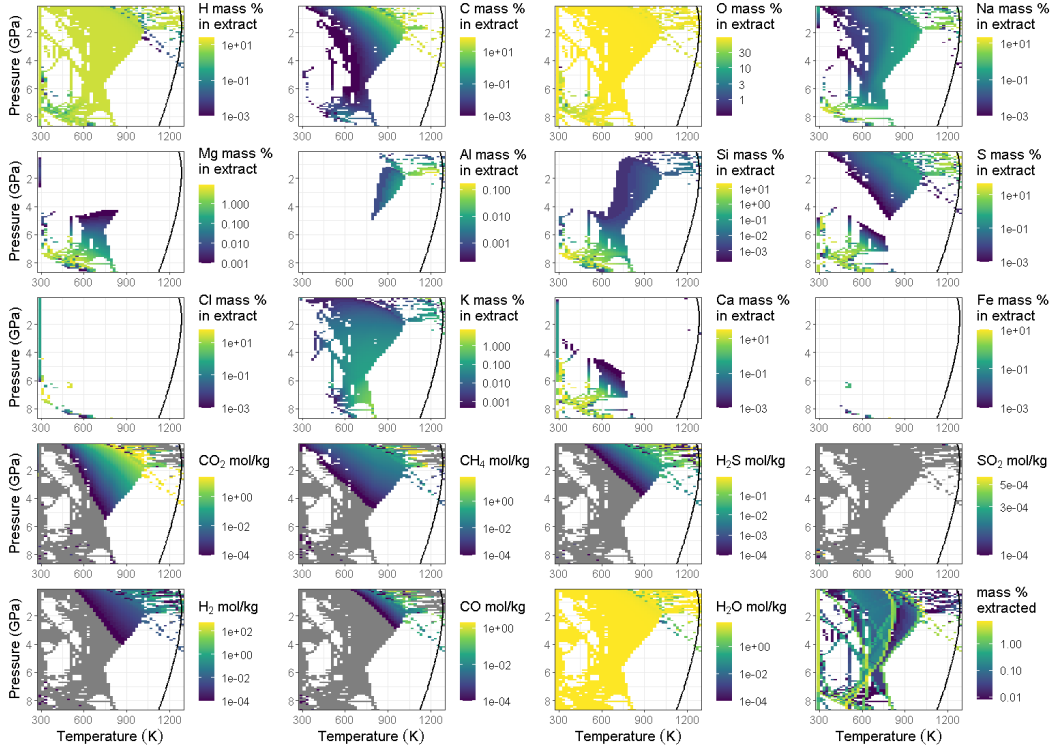
303

304

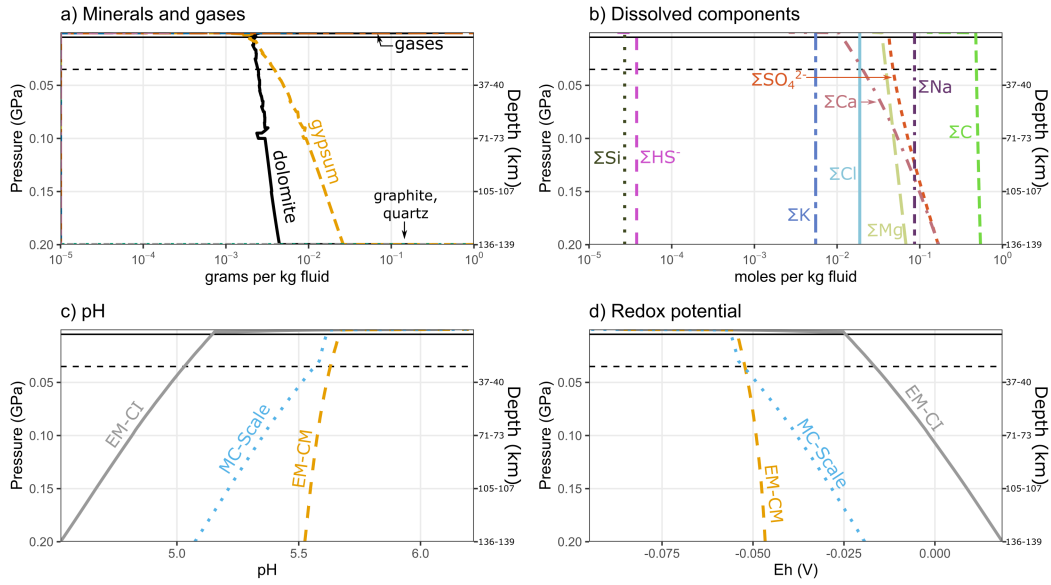
305

306

The combined mass of gases (particularly CO₂) that would boil out of the ocean at low pressure (i.e., at < 20 MPa for a hypothetical non-ice covered surface) is comparable to the mass of precipitated minerals (Fig. 3 and Table 1). The massive outgassing of volatiles (0.06–1.33 % Europa's mass; Table 1) may have led to an early CO₂-rich atmosphere of considerable thickness, on the order of 1–27 MPa for the mass of exsolved gases calculated if they were released all at once. (We note that 5–25 MPa of H₂O and in excess of 1–5.5 MPa of CO₂ are calculated to have been lost from Mars < 12 Myr



262 **Figure 2.** Composition of the fluid extracted from the deep interior at different pressures with
 263 increasing temperature for the *EM-CM* $R/E=0$ model. Solid curves show the Fe-FeS eutectic
 264 temperature. Integrating up to the eutectic yields the total amounts exsolved from the deep in-
 265 terior. Blank areas signify that no fluids containing the specific element shown in the plot were
 266 extracted at those pressures and temperatures. Rows 1–3: elemental abundance of the extracted
 267 fluid (solvents and solutes). Rows 4–5: molecular solvent moles per kilogram of extracted fluid.
 268 Grey areas in the solvent plots signify that fluids were extracted at those pressures and tempera-
 269 tures, but did not contain the specific solvent shown in the plot. Bottom-right plot: total (solvent
 270 + solute) extracted mass. For corresponding figures of the broadly similar patterns of exsolution
 271 in the *EM-CI* and *MC-Scale* models, see Figures S7–S10



283 **Figure 3.** Ocean column compositions from the seafloor to the surface, for *EM-CM*. Solid and
 284 horizontal lines show the pressure at the base of a current 5 km and 30 km ice shell respectively
 285 (see §3.3). a) Minerals precipitated and gases exsolved with decreasing depth in the water col-
 286 umn. b) Total dissolved components in the water column. Dissolved components shown here are
 287 the sum of those particular components distributed among all species in solution. For example,
 288 component ΣC represents the sum of carbon in aqueous HCO_3^- , CH_4 , CO_2 , and organics, among
 289 other species. Concentrations $< 10^{-5}$ mol/kg not shown. c) pH, and d) redox potential of the
 290 ocean column for the $R/E = 0$ models of *EM-CI*, *EM-CM* and *MC-Scale*.

307 after accretion (Erkaev et al., 2014; Odert et al., 2018). Massive primordial atmospheres
 308 have also been predicted for Triton (~ 16 MPa $p\text{CO}_2$; Lunine & Nolan, 1992), Titan,
 309 Ganymede and Callisto (Kuramoto & Matsui, 1994.) With such a thick atmosphere,
 310 greenhouse trapping of heat generated by insolation (Zahnle & Catling, 2017), radioac-
 311 tive decay or tides would likely vaporize Europa's hydrosphere, although exceedingly high
 312 rates of atmospheric escape by ionization in Jupiter's magnetosphere, or solar energetic
 313 particles and galactic cosmic rays, would have likely either prevented atmospheric build-
 314 up, or allowed recondensation of the hydrosphere.

315 More likely, the rate of heating (radioactive or tidal) would control the rate of ex-
 316 solution from the deep interior, ocean build-up, and the subsequent mass outgassed from
 317 the ocean. Based on mass ejection rates from tentative plume detections (Roth et al.,
 318 2014; Sparks et al., 2016), plumes could output up to 7.2×10^{19} – 7.2×10^{20} kg of H_2O
 319 over the lifetime of the solar system, or about 1.4–24 % of Europa's present ocean mass
 320 (Text S6). Alternatively, clathrate hydrates could trap dissolved carbon and limit CO_2
 321 outgassing. Whether CO_2 clathrates are stable in Europa's ocean depends on the pres-
 322 sure and temperature, assuming sufficient CO_2 feedstock is present. For the large amounts
 323 of CO_2 produced here we predict structure I clathrates with a $\text{CO}_2/\text{H}_2\text{O}$ molar ratio of
 324 0.159 at 273.15 K and equilibrium pressure (1.24 MPa), with a density of 1106 kg/m^3
 325 (see Text S6 for details). This exceeds the ocean's density, so these clathrates would sink,
 326 forming a 3.4–77 km layer on the seafloor. However, the long term stability of such a clathrate
 327 layer may be unfavorable because: 1) temperatures > 277 K preclude CO_2 clathrate sta-
 328 bility in Europa's ocean (Text S6 and Fig. S14), and magmatic episodes are predicted
 329 at Europa's seafloor over geologic time (Běhouňková et al., 2021), and 2) formation of
 330 the ice shell would further increase the salinity and density of the ocean, inhibiting the
 331 formation of clathrates or making them buoyant.

340 We find major differences between the ocean compositions predicted here and those
 341 presented previously. On the basis of thermodynamic equilibrium and extensive water-
 342 rock interaction between the ocean and the seafloor, Zolotov and Kargel (2009) predicted
 343 a "low pH" fluid that rapidly ($\sim 10^6$ yr) evolved to a reduced and basic primordial ocean
 344 ($\text{pH} = 13$ – 13.6) rich in H_2 , Na^+ , K^+ , Ca^+ , OH^- , and Cl^- . The escape of H_2 may have
 345 then led to a progressively oxidized, sulfate-rich ocean today. On the other hand, work
 346 by Zolotov and Shock (2001) and Kargel et al. (2000) on the low temperature aqueous
 347 differentiation, brine evolution, and freezing of the european ocean broadly coincides with
 348 our predictions for a sulfate- and carbonate-rich ocean, although they predict that the
 349 most abundant cation in solution would be Mg^{2+} instead of Ca^{2+} . Hansen and McCord
 350 (2008) also favored a CO_2 -rich ocean based on spectroscopic observations.

351 We also find it significant that the composition of the ocean column is depth-de-
 352 pendent, such that anion and cation concentrations, pH, and redox conditions close to
 353 the seafloor are not apparently reflective of the composition nearer to the surface or at
 354 the base of the ice shell. A caveat is that the results presented here do not account for
 355 homogenizing or unmixing of the ocean column's composition by advection or convec-
 356 tion, or latitudinal changes; a comprehensive ocean circulation model (e.g. Lobo et al.,
 357 2021) would be required to place such constraints.

358 **3.3 Consequences of fluid extraction on the silicate mantle and struc-** 359 **ture of Europa**

360 Removal of $\text{Fe} \pm \text{S}$ from the devolatilized deep interior at the Fe-FeS eutectic (§2.3),
 361 and calculation of Europa's structure with `PlanetProfile` using the resulting core and
 362 residual silicate mantle thermodynamic properties (§2.4) yields a spherical shell struc-
 363 ture, MoI (0.3455–0.3457) and density consistent with present-day Europa observations,
 364 assuming a ~ 30 km ice shell (Fig. 1; Text S4). (Further details about the predicted

365 deep mineralogy are found in Text S5 and Figures S12–S13. Figure S16 shows the den-
 366 sity, heat capacity, and bulk and shear moduli of resulting profiles.)

367 4 Concluding remarks

368 We find that the resulting volatile mass evolved from Europa’s deep interior is con-
 369 sistent with, and can even exceed, the hydrosphere’s present mass. The size and com-
 370 position of the ocean depend on the assumed accreted composition of Europa. Differ-
 371 ent bulk compositions lead to different mineralogies in the thermodynamic model, that
 372 mediate the escape of volatiles and solutes. To elaborate:

- 373 1. Building a volatile mass equivalent to that of Europa’s current hydrosphere by pro-
 374 grade metamorphism prior to core formation was probable if Europa accreted a
 375 disproportionately large amount of CI or CM chondrite material, water, and/or
 376 cometary material relative to the expected abundance of these materials at Jupiter’s
 377 location in the early Solar System (c.f. Desch et al., 2018). Other known chon-
 378 dritic materials have insufficient volatile mass extractable by metamorphism to
 379 account for Europa’s present hydrosphere mass (§2.1 & §3.1).
- 380 2. Europa’s ocean, if derived from thermal evolution of the interior as shown here,
 381 was carbon and sulfur-rich (§3.1). If thermal excursions in the interior (from ra-
 382 dioactive decay and tidal dissipation) were unimportant since differentiation, geo-
 383 chemical equilibrium models predict that the ocean would remain CO₂, carbon-
 384 ate and CaSO₄-rich (§3.2). However, pressure has a first order effect on the ocean’s
 385 composition: decreasing pressure precipitates gypsum, removing calcium and sul-
 386 fur from solution, thereby increasing the relative concentration of chlorine further
 387 up the water column, such that Cl > S at $\lesssim 10$ MPa. Thickening of the ice shell
 388 preferentially freezes in SO₄²⁻, rejecting and concentrating Cl at the base of the
 389 ice shell in time (Marion et al., 2005), leaving the relative concentration of SO₄²⁻
 390 unchanged at depth.
- 391 3. While the volatile mass in the initially accreted bulk body was high (§3.1), the deep
 392 interior must be relatively volatile-free at present to meet the MoI and density con-
 393 straints (§3.3). Therefore, prograde metamorphism and fluid migration into the
 394 hydrosphere was necessarily efficient in order to remove volatile mass from the in-
 395 terior. Volatile loss from the rocky interior in excess of the present hydrosphere
 396 mass can be accommodated by early loss to space, especially because of the high
 397 pCO₂ outgassed. Alternatively, a large portion of volatiles (particularly CO₂) would
 398 be retained in clathrates, and their periodic destabilization by tidal heating may
 399 provide oxidants and buoyant pressure at the ice-ocean interface. We rule out com-
 400 plete ocean freeze-out enabled by the thermal blanketing effect of a stable seafloor
 401 clathrate layer: even if a thick clathrate layer is stable at the seafloor over geo-
 402 logic time, $\lesssim 80$ km thick high pressure ice layers at Ganymede and Titan with
 403 heat fluxes > 6 mW/m² from the silicate interior are able to maintain a liquid
 404 ocean (Kalousová & Sotin, 2020). Melt and heat transport from the bottom of the
 405 clathrate layer to the ocean would occur either through hot plume conduits or solid
 406 state convection (Choblet et al., 2017; Kalousová & Sotin, 2020).
- 407 4. The CO₂-rich ocean delivered by metamorphism may facilitate life’s emergence
 408 by contributing to the generation of a proton gradient between acidic ocean wa-
 409 ter and alkaline hydrothermal fluids (Camprubí et al., 2019), if the latter are present
 410 in Europa.

411 While these updated models are enabled by modern computational thermodynam-
 412 ics and data, we expect that further work will refine these results prior to the arrival of
 413 the *JUICE* and *Europa Clipper* missions in the coming decade. In particular, 4.5 Gyr
 414 of tidally-mediated magmatism may have continued to modify the deep interior, possi-
 415 bly driving solid-state mantle convection, volcanism, and volatile element redistribution

416 and loss (Běhounková et al., 2021). The oxidized ocean may have reduced in time with
 417 hydrogen generated by serpentinization enabled by thermal cracking (Vance et al., 2016),
 418 but better constraints on the conditions of fracture formation and propagation are re-
 419 quired (Klimczak et al., 2019). Further improvements to the thermodynamic data of high
 420 pressure H₂O-CO₂ phases (Abramson et al., 2018) and their integration with thermo-
 421 dynamic models (e.g., `Perple_X`) are also needed to assess the build-up of the ocean: the
 422 stability of such phases can be the factor dictating whether an ocean world will be hab-
 423 itable (Marounina & Rogers, 2020). Finally, we have also made the simplifying assump-
 424 tion that fluid percolation from depth was efficient. A coupled tidal-thermodynamic-geo-
 425 dynamic model would more accurately determine fluid retained-to-extracted ratios.

426 Data Availability Statement

427 All data are available though Zenodo ([doi to be generated prior to publication](#)).
 428 `AccretR` is available through Melwani Daswani (2020). `PlanetProfile` is available through
 429 Vance, Styczinski, Melwani Daswani, and Vega (2020). `Rcrust` is available through Mayne
 430 et al. (2016) and <https://tinyurl.com/rcrust>.

431 Acknowledgments

432 MMD thanks Jinping Hu, Paul Byrne, Orenthal Tucker, Evan Carnahan and the
 433 Origins and Habitability Laboratory (JPL) for discussions, Saikiran Tharimena for codes,
 434 Hauke Hussmann for tidal dissipation data, and James Connolly for help with the `Perple_-`
 435 `X` code. We thank JPL research interns Marika Leitner and Garret Levine for early con-
 436 tributions to this work. This work was supported by NASA through the Europa Clip-
 437 per Project to MMD, SV and CRG, and NASA grant NNH18ZDA001N-HW:Habitable
 438 Worlds awarded to MMD and SV. A part of this research was carried out at the Jet Propul-
 439 sion Laboratory, California Institute of Technology, under a contract with the National
 440 Aeronautics and Space Administration (80NM0018D0004). ©2021. All rights reserved.

441 References

- 442 Abramson, E. H., Bollengier, O., Brown, J. M., Journaux, B., Kaminsky, W.,
 443 & Pakhomova, A. (2018, September). Carbonic acid monohydrate.
 444 *American Mineralogist*, 103(9), 1468–1472. Retrieved 2020-07-22, from
 445 <https://doi.org/10.2138/am-2018-6554> doi: 10.2138/am-2018-6554
- 446 Anderson, J. D., Schubert, G., Jacobson, R. A., Lau, E. L., Moore, W. B., & Sjo-
 447 gren, W. L. (1998). Europa’s differentiated internal structure: Inferences
 448 from four Galileo encounters. *Science*, 281(5385), 2019–2022. Retrieved
 449 from <http://science.sciencemag.org/content/281/5385/2019> doi:
 450 10.1126/science.281.5385.2019
- 451 Barr, A. C., & Canup, R. M. (2008). Constraints on gas giant satellite formation
 452 from the interior states of partially differentiated satellites. *Icarus*, 198(1), 163
 453 - 177. Retrieved from [http://www.sciencedirect.com/science/article/
 454 pii/S0019103508002595](http://www.sciencedirect.com/science/article/pii/S0019103508002595) doi: <https://doi.org/10.1016/j.icarus.2008.07.004>
- 455 Bierson, C. J., & Nimmo, F. (2020, July). Explaining the Galilean Satellites’ Density
 456 Gradient by Hydrodynamic Escape. *The Astrophysical Journal*, 897(2), L43.
 457 Retrieved from <http://dx.doi.org/10.3847/2041-8213/aba11a> (Publisher:
 458 American Astronomical Society) doi: 10.3847/2041-8213/aba11a
- 459 Bland, M. T., Showman, A. P., & Tobie, G. (2008, December). The production of
 460 Ganymede’s magnetic field. *Icarus*, 198(2), 384–399. Retrieved from [http://
 461 www.sciencedirect.com/science/article/pii/S0019103508002807](http://www.sciencedirect.com/science/article/pii/S0019103508002807) doi: 10
 462 .1016/j.icarus.2008.07.011
- 463 Brown, M. E., & Hand, K. P. (2013). Salts and radiation products on the surface

- 464 of Europa. *The Astronomical Journal*, 145(4), 110. Retrieved from [http://](http://dx.doi.org/10.1088/0004-6256/145/4/110)
 465 [dx.doi.org/10.1088/0004-6256/145/4/](http://dx.doi.org/10.1088/0004-6256/145/4/110)
 466 [110](http://dx.doi.org/10.1088/0004-6256/145/4/110) doi: 10.1088/0004-6256/145/4/
- 467 Běhouňková, M., Tobie, G., Choblet, G., Kervazo, M., Melwani Daswani, M.,
 468 Dumoulin, C., & Vance, S. D. (2021, February). Tidally Induced Mag-
 469 matic Pulses on the Oceanic Floor of Jupiter’s Moon Europa. *Geophysi-*
 470 *cal Research Letters*, 48(3), e2020GL090077. Retrieved 2021-02-05, from
 471 <https://doi.org/10.1029/2020GL090077> (Publisher: John Wiley & Sons,
 472 Ltd) doi: 10.1029/2020GL090077
- 473 Camprubí, E., de Leeuw, J. W., House, C. H., Raulin, F., Russell, M. J., Spang,
 474 A., . . . Westall, F. (2019, December). The Emergence of Life. *Space Sci-*
 475 *ence Reviews*, 215(8), 56. Retrieved from [https://doi.org/10.1007/](https://doi.org/10.1007/s11214-019-0624-8)
 476 [s11214-019-0624-8](https://doi.org/10.1007/s11214-019-0624-8) doi: 10.1007/s11214-019-0624-8
- 477 Canup, R. M., & Ward, W. R. (2002, December). Formation of the Galilean Satel-
 478 lites: Conditions of Accretion. *The Astronomical Journal*, 124(6), 3404–3423.
 479 Retrieved from <http://dx.doi.org/10.1086/344684> doi: 10.1086/344684
- 480 Canup, R. M., & Ward, W. R. (2009). Origin of Europa and the Galilean satellites.
 481 In R. T. Pappalardo, W. B. McKinnon, & K. Khurana (Eds.), *Europa* (pp.
 482 59–83). Tucson, AZ: University of Arizona Press.
- 483 Choblet, G., Tobie, G., Sotin, C., Kalousová, K., & Grasset, O. (2017, March). Heat
 484 transport in the high-pressure ice mantle of large icy moons. *Icarus*, 285, 252–
 485 262. Retrieved from [http://www.sciencedirect.com/science/article/pii/](http://www.sciencedirect.com/science/article/pii/S0019103516302524)
 486 [S0019103516302524](http://www.sciencedirect.com/science/article/pii/S0019103516302524) doi: 10.1016/j.icarus.2016.12.002
- 487 Connolly, J. A. D. (2005). Computation of phase equilibria by linear program-
 488 ming: A tool for geodynamic modeling and its application to subduction zone
 489 decarbonation. *Earth and Planetary Science Letters*, 236(1-2), 524–541. Re-
 490 trieved 2018-08-08, from [http://linkinghub.elsevier.com/retrieve/pii/](http://linkinghub.elsevier.com/retrieve/pii/S0012821X05002839)
 491 [S0012821X05002839](http://linkinghub.elsevier.com/retrieve/pii/S0012821X05002839) doi: 10.1016/j.epsl.2005.04.033
- 492 Connolly, J. A. D. (2009). The geodynamic equation of state: What and how.
 493 *Geochemistry, Geophysics, Geosystems*, 10(10). Retrieved 2018-03-22,
 494 from [https://agupubs.onlinelibrary.wiley.com/doi/abs/10.1029/](https://agupubs.onlinelibrary.wiley.com/doi/abs/10.1029/2009GC002540)
 495 [2009GC002540](https://agupubs.onlinelibrary.wiley.com/doi/abs/10.1029/2009GC002540) doi: 10.1029/2009GC002540
- 496 Connolly, J. A. D., & Galvez, M. E. (2018). Electrolytic fluid speciation by Gibbs
 497 energy minimization and implications for subduction zone mass transfer. *Earth*
 498 *and Planetary Science Letters*, 501, 90–102. Retrieved 2019-01-07, from
 499 <https://linkinghub.elsevier.com/retrieve/pii/S0012821X18304904>
 500 doi: 10.1016/j.epsl.2018.08.024
- 501 Desch, S. J., Kalyaan, A., & Alexander, C. M. O. (2018). The Effect of Jupiter’s
 502 Formation on the Distribution of Refractory Elements and Inclusions in Me-
 503 teorites. *The Astrophysical Journal Supplement Series*, 238(1), 11. Retrieved
 504 from <http://stacks.iop.org/0067-0049/238/i=1/a=11>
- 505 Erkaev, N., Lammer, H., Elkins-Tanton, L., Stökl, A., Odert, P., Marcq, E., . . .
 506 Güdel, M. (2014, August). Escape of the martian protoatmosphere and initial
 507 water inventory. *Planetary evolution and life*, 98, 106–119. Retrieved from
 508 <http://www.sciencedirect.com/science/article/pii/S0032063313002353>
 509 doi: 10.1016/j.pss.2013.09.008
- 510 Estrada, P. R., Mosqueira, I., Lissauer, J. J., D’Angelo, G., & Cruikshank, D.
 511 (2009). Formation of Jupiter and conditions for accretion of the Galilean satel-
 512 lites. In R. T. Pappalardo, W. B. McKinnon, & K. Khurana (Eds.), *Europa*
 513 (pp. 27–58). Tucson, AZ: University of Arizona Press.
- 514 Fischer, P. D., Brown, M. E., Trumbo, S. K., & Hand, K. P. (2016). Spatially
 515 resolved spectroscopy of Europa’s large-scale compositional units at 3–4
 516 μm with Keck NIRSPEC. *The Astronomical Journal*, 153(1), 13. Re-
 517 trieved from <http://dx.doi.org/10.3847/1538-3881/153/1/13> doi:
 518 [10.3847/1538-3881/153/1/13](http://dx.doi.org/10.3847/1538-3881/153/1/13)

- 519 Gaidos, E. J., Neelson, K. H., & Kirschvink, J. L. (1999, June). Life in Ice-
 520 Covered Oceans. *Science*, *284*(5420), 1631. Retrieved from [http://](http://science.sciencemag.org/content/284/5420/1631.abstract)
 521 science.sciencemag.org/content/284/5420/1631.abstract doi:
 522 10.1126/science.284.5420.1631
- 523 Glein, C. R., Postberg, F., & Vance, S. D. (2018). The Geochemistry of Ence-
 524 ladus: Composition and Controls. In *Enceladus and the Icy Moons of Sat-*
 525 *urn*. The University of Arizona Press. Retrieved 2020-07-30, from [https://](https://uapress.arizona.edu/book/enceladus-and-the-icy-moons-of-saturn)
 526 uapress.arizona.edu/book/enceladus-and-the-icy-moons-of-saturn
 527 doi: 10.2458/azu_uapress_9780816537075-ch003
- 528 Gorce, J., Caddick, M., & Bodnar, R. (2019, August). Thermodynamic con-
 529 straints on carbonate stability and carbon volatility during subduction.
 530 *Earth and Planetary Science Letters*, *519*, 213–222. Retrieved from [https://](https://www.sciencedirect.com/science/article/pii/S0012821X19302596)
 531 www.sciencedirect.com/science/article/pii/S0012821X19302596 doi:
 532 10.1016/j.epsl.2019.04.047
- 533 Greeley, R., Chyba, C. F., Head, J., McCord, T., McKinnon, W. B., Pappalardo,
 534 R. T., ... others (2004). Geology of Europa. In *Jupiter: The Planet, Satellites*
 535 *and Magnetosphere* (pp. 329–362). (Publisher: Cambridge Univ. Press New
 536 York)
- 537 Hand, K., Carlson, R., & Chyba, C. (2007). Energy, chemical disequilibrium, and ge-
 538 ological constraints on Europa. *Astrobiology*, *7*(6), 1006–1022.
- 539 Hansen, G. B., & McCord, T. B. (2008, January). Widespread CO₂ and other
 540 non-ice compounds on the anti-Jovian and trailing sides of Europa from
 541 Galileo/NIMS observations. *Geophysical Research Letters*, *35*(1). Retrieved
 542 2020-10-08, from <https://doi.org/10.1029/2007GL031748> (Publisher: John
 543 Wiley & Sons, Ltd) doi: 10.1029/2007GL031748
- 544 Huss, G. R., Rubin, A. E., & Grossman, J. N. (2006). Thermal Metamorphism
 545 in Chondrites. In D. S. Lauretta & H. Y. McSween (Eds.), *Meteorites and*
 546 *the Early Solar System II* (pp. 567–586). Tucson, AZ: University of Arizona
 547 Press.
- 548 Hussmann, H., & Spohn, T. (2004). Thermal-orbital evolution of Io and Europa.
 549 *Icarus*, *171*(2), 391 - 410. Retrieved from [http://www.sciencedirect.com/](http://www.sciencedirect.com/science/article/pii/S0019103504001952)
 550 [science/article/pii/S0019103504001952](http://www.sciencedirect.com/science/article/pii/S0019103504001952) doi: [https://doi.org/10.1016/](https://doi.org/10.1016/j.icarus.2004.05.020)
 551 [j.icarus.2004.05.020](https://doi.org/10.1016/j.icarus.2004.05.020)
- 552 Kalousová, K., & Sotin, C. (2020, September). Dynamics of Titan’s high-pressure
 553 ice layer. *Earth and Planetary Science Letters*, *545*, 116416. Retrieved from
 554 <http://www.sciencedirect.com/science/article/pii/S0012821X20303605>
 555 doi: 10.1016/j.epsl.2020.116416
- 556 Kargel, J. S. (1991, December). Brine volcanism and the interior structures of as-
 557 teroids and icy satellites. *Icarus*, *94*(2), 368–390. Retrieved from [http://](http://www.sciencedirect.com/science/article/pii/001910359190235L)
 558 www.sciencedirect.com/science/article/pii/001910359190235L doi: 10
 559 .1016/0019-1035(91)90235-L
- 560 Kargel, J. S., Kaye, J. Z., Head, J. W., Marion, G. M., Sassen, R., Crowley, J. K.,
 561 ... Hogenboom, D. L. (2000). Europa’s Crust and Ocean: Origin, Compo-
 562 sition, and the Prospects for Life. *Icarus*, *148*(1), 226–265. Retrieved from
 563 <http://www.sciencedirect.com/science/article/pii/S0019103500964716>
 564 doi: 10.1006/icar.2000.6471
- 565 Klimczak, C., Byrne, P. K., Regensburger, P. V., Bohnenstiehl, D. R., Hauck,
 566 S. A., II, Dombard, A. J., ... Elder, C. M. (2019, March). Strong Ocean
 567 Floors Within Europa, Titan, and Ganymede Limit Geological Activ-
 568 ity There; Enceladus Less So. In (p. 2912). Retrieved from [https://](https://ui.adsabs.harvard.edu/abs/2019LPI....50.2912K)
 569 ui.adsabs.harvard.edu/abs/2019LPI....50.2912K
- 570 Kuramoto, K., & Matsui, T. (1994, October). Formation of a hot proto-
 571 atmosphere on the accreting giant icy satellite: Implications for the origin
 572 and evolution of Titan, Ganymede, and Callisto. *Journal of Geophysi-*
 573 *cal Research: Planets*, *99*(E10), 21183–21200. Retrieved 2021-01-29, from

- 574 <https://doi.org/10.1029/94JE01864> (Publisher: John Wiley & Sons, Ltd)
 575 doi: 10.1029/94JE01864
- 576 Kuskov, O., & Kronrod, V. (2005). Internal structure of Europa and Callisto.
 577 *Icarus*, 177(2), 550 - 569. Retrieved from [http://www.sciencedirect.com/
 578 science/article/pii/S0019103505001806](http://www.sciencedirect.com/science/article/pii/S0019103505001806) doi: [https://doi.org/10.1016/
 579 j.icarus.2005.04.014](https://doi.org/10.1016/j.icarus.2005.04.014)
- 580 Leitner, M. A., & Lunine, J. I. (2019, November). Modeling early Titan's
 581 ocean composition. *Icarus*, 333, 61–70. Retrieved 2020-07-08, from
 582 <https://linkinghub.elsevier.com/retrieve/pii/S0019103518303312>
 583 doi: 10.1016/j.icarus.2019.05.008
- 584 Ligier, N., Poulet, F., Carter, J., Brunetto, R., & Gourgeot, F. (2016, may).
 585 VLT/SINFONI Observations of Europa: New insights into the surface
 586 composition. *The Astronomical Journal*, 151(6), 163. Retrieved from
 587 [https://doi.org/10.3847/
 588 0004-6256/151/6/163](https://doi.org/10.3847/2F0004-6256/2F151%2F6%2F163) doi: 10.3847/
 0004-6256/151/6/163
- 589 Lobo, A. H., Thompson, A. F., Vance, S. D., & Tharimena, S. (2021, April). A
 590 pole-to-equator ocean overturning circulation on Enceladus. *Nature Geo-
 591 science*, 14(4), 185–189. Retrieved from [https://doi.org/10.1038/
 592 s41561-021-00706-3](https://doi.org/10.1038/s41561-021-00706-3) doi: 10.1038/s41561-021-00706-3
- 593 Lunine, J. I., & Nolan, M. C. (1992, November). A massive early atmosphere on
 594 Triton. *Icarus*, 100(1), 221–234. Retrieved from [http://www.sciencedirect
 595 .com/science/article/pii/0019103592900312](http://www.sciencedirect.com/science/article/pii/0019103592900312) doi: 10.1016/0019-1035(92)
 596 90031-2
- 597 Lunine, J. I., & Stevenson, D. J. (1982, October). Formation of the galilean satel-
 598 lites in a gaseous nebula. *Icarus*, 52(1), 14–39. Retrieved from [https://
 599 www.sciencedirect.com/science/article/pii/001910358290166X](https://www.sciencedirect.com/science/article/pii/001910358290166X) doi: 10
 600 .1016/0019-1035(82)90166-X
- 601 Makalkin, A. B., Dorofeeva, V. A., & Ruskol, E. L. (1999, January). Modeling
 602 the Protosatellite Circum-Jovian Accretion Disk: An Estimate of the Basic
 603 Parameters. *Solar System Research*, 33, 456.
- 604 Manthilake, G., Bolfan-Casanova, N., Novella, D., Mookherjee, M., & Andrault, D.
 605 (2016, May). Dehydration of chlorite explains anomalously high electrical con-
 606 ductivity in the mantle wedges. *Science Advances*, 2(5), e1501631. Retrieved
 607 from <http://advances.sciencemag.org/content/2/5/e1501631.abstract>
 608 doi: 10.1126/sciadv.1501631
- 609 Marion, G. M., Kargel, J. S., Catling, D. C., & Jakubowski, S. D. (2005, January).
 610 Effects of pressure on aqueous chemical equilibria at subzero temperatures
 611 with applications to Europa. *Geochimica et Cosmochimica Acta*, 69(2),
 612 259–274. Retrieved 2018-09-30, from [http://linkinghub.elsevier.com/
 613 retrieve/pii/S0016703704004880](http://linkinghub.elsevier.com/retrieve/pii/S0016703704004880) doi: 10.1016/j.gca.2004.06.024
- 614 Marounina, N., & Rogers, L. A. (2020, February). Internal Structure and CO2
 615 Reservoirs of Habitable Water Worlds. *The Astrophysical Journal*, 890(2), 107.
 616 Retrieved from <http://dx.doi.org/10.3847/1538-4357/ab68e4> (Publisher:
 617 American Astronomical Society) doi: 10.3847/1538-4357/ab68e4
- 618 Mayne, M. J., Moya, J.-F., Stevens, G., & Kaislaniemi, L. (2016, May). Rcrust: a
 619 tool for calculating path-dependent open system processes and application to
 620 melt loss. *Journal of Metamorphic Geology*, 34(7), 663–682. Retrieved 2018-
 621 07-25, from <https://doi.org/10.1111/jmg.12199> doi: 10.1111/jmg.12199
- 622 McCord, T. B., Hansen, G. B., Fanale, F. P., Carlson, R. W., Matson, D. L., John-
 623 son, T. V., ... Granahan, J. C. (1998, May). Salts on Europa's Surface De-
 624 tected by Galileo's Near Infrared Mapping Spectrometer. *Science*, 280(5367),
 625 1242. Retrieved from [http://science.sciencemag.org/content/280/5367/
 626 1242.abstract](http://science.sciencemag.org/content/280/5367/1242.abstract) doi: 10.1126/science.280.5367.1242
- 627 McKinnon, W. B., & Zolensky, M. E. (2003). Sulfate Content of Europa's Ocean
 628 and Shell: Evolutionary Considerations and Some Geological and Astrobio-

- 629 logical Implications. *Astrobiology*, 3(4), 879–897. Retrieved 2020-04-06, from
 630 <https://doi.org/10.1089/153110703322736150> (Publisher: Mary Ann
 631 Liebert, Inc., publishers) doi: 10.1089/153110703322736150
- 632 Melwani Daswani, M. (2020, May). *AccretR*. Zenodo. Retrieved 2021-05-08, from
 633 <https://zenodo.org/record/3827540> doi: 10.5281/ZENODO.3827540
- 634 Miller, K. E., Glein, C. R., & Waite, J. H. (2019, Jan). Contributions from ac-
 635 creted organics to Titan’s atmosphere: New insights from cometary and chon-
 636 dritic data. *The Astrophysical Journal*, 871(1), 59. Retrieved from [http://](http://dx.doi.org/10.3847/1538-4357/aaf561)
 637 dx.doi.org/10.3847/1538-4357/aaf561 doi: 10.3847/1538-4357/aaf561
- 638 Moore, W. B., & Hussmann, H. (2009). Thermal evolution of Europa’s silicate in-
 639 terior. In R. T. Pappalardo, W. B. McKinnon, & K. Khurana (Eds.), *Europa*
 640 (pp. 369–380). Tucson: University of Arizona Press.
- 641 Mosqueira, I., Estrada, P., & Turrini, D. (2010, June). Planetesimals and Satellites-
 642 imals: Formation of the Satellite Systems. *Space Science Reviews*, 153(1-4),
 643 431–446. Retrieved 2021-04-13, from [http://link.springer.com/10.1007/](http://link.springer.com/10.1007/s11214-009-9614-6)
 644 [s11214-009-9614-6](http://link.springer.com/10.1007/s11214-009-9614-6) doi: 10.1007/s11214-009-9614-6
- 645 Néri, A., Guyot, F., Reynard, B., & Sotin, C. (2020, Oct). A carbonaceous chondrite
 646 and cometary origin for icy moons of Jupiter and Saturn. *Earth and Planetary*
 647 *Science Letters*, 115920. Retrieved from [http://dx.doi.org/10.1016/j.epsl](http://dx.doi.org/10.1016/j.epsl.2019.115920)
 648 [.2019.115920](http://dx.doi.org/10.1016/j.epsl.2019.115920) doi: 10.1016/j.epsl.2019.115920
- 649 Odert, P., Lammer, H., Erkaev, N., Nikolaou, A., Lichtenegger, H., Johnstone, C.,
 650 ... Tosi, N. (2018, June). Escape and fractionation of volatiles and noble gases
 651 from Mars-sized planetary embryos and growing protoplanets. *Icarus*, 307,
 652 327–346. Retrieved from [http://www.sciencedirect.com/science/article/](http://www.sciencedirect.com/science/article/pii/S0019103517301677)
 653 [pii/S0019103517301677](http://www.sciencedirect.com/science/article/pii/S0019103517301677) doi: 10.1016/j.icarus.2017.10.031
- 654 Pan, D., Spanu, L., Harrison, B., Sverjensky, D. A., & Galli, G. (2013, April).
 655 Dielectric properties of water under extreme conditions and transport of car-
 656 bonates in the deep Earth. *Proceedings of the National Academy of Sciences*,
 657 110(17), 6646. Retrieved from [http://www.pnas.org/content/110/17/](http://www.pnas.org/content/110/17/6646.abstract)
 658 [6646.abstract](http://www.pnas.org/content/110/17/6646.abstract) doi: 10.1073/pnas.1221581110
- 659 Pasek, M. A., & Greenberg, R. (2012). Acidification of Europa’s subsurface ocean as
 660 a consequence of oxidant delivery. *Astrobiology*, 12(2), 151–159.
- 661 Reed, M. H. (1998). Calculation of simultaneous chemical equilibria in aqueous-
 662 mineral-gas systems and its application to modeling hydrothermal processes.
 663 In J. P. Richards (Ed.), *Techniques in Hydrothermal Ore Deposits Geology*
 664 (Vol. 10, pp. 109–124). Littleton, CO: Society of Economic Geologists, Inc.
- 665 Richard, G., Monnereau, M., & Rabinowicz, M. (2007, March). Slab dehydra-
 666 tion and fluid migration at the base of the upper mantle: implications for
 667 deep earthquake mechanisms. *Geophysical Journal International*, 168(3),
 668 1291–1304. Retrieved 2020-06-27, from [https://doi.org/10.1111/](https://doi.org/10.1111/j.1365-246X.2006.03244.x)
 669 [j.1365-246X.2006.03244.x](https://doi.org/10.1111/j.1365-246X.2006.03244.x) doi: 10.1111/j.1365-246X.2006.03244.x
- 670 Ronnet, T., & Johansen, A. (2020, January). Formation of moon systems around gi-
 671 ant planets: Capture and ablation of planetesimals as foundation for a pebble
 672 accretion scenario. *Astronomy & Astrophysics*, 633, A93. Retrieved 2021-
 673 04-13, from <https://www.aanda.org/10.1051/0004-6361/201936804> doi:
 674 [10.1051/0004-6361/201936804](https://www.aanda.org/10.1051/0004-6361/201936804)
- 675 Ronnet, T., Mousis, O., & Vernazza, P. (2017). Pebble Accretion at the Origin of
 676 Water in Europa. *The Astrophysical Journal*, 845(2), 92. Retrieved 2018-12-
 677 18, from [http://stacks.iop.org/0004-637X/845/i=2/a=92?key=crossref](http://stacks.iop.org/0004-637X/845/i=2/a=92?key=crossref.e075ce27e4a38f6e8b1624cbb3608530)
 678 [.e075ce27e4a38f6e8b1624cbb3608530](http://stacks.iop.org/0004-637X/845/i=2/a=92?key=crossref.e075ce27e4a38f6e8b1624cbb3608530) doi: 10.3847/1538-4357/aa80e6
- 679 Roth, L., Saur, J., Retherford, K. D., Strobel, D. F., Feldman, P. D., Mc-
 680 Grath, M. A., & Nimmo, F. (2014, January). Transient Water Va-
 681 por at Europa’s South Pole. *Science*, 343(6167), 171. Retrieved from
 682 <http://science.sciencemag.org/content/343/6167/171.abstract> doi:
 683 [10.1126/science.1247051](http://science.sciencemag.org/content/343/6167/171.abstract)

- 684 Schubert, G., Sohl, F., & Hussmann, H. (2009). Interior of Europa. In R. T. Pappalardo, W. B. McKinnon, & K. Khurana (Eds.), *Europa* (pp. 353–367). Tucson: University of Arizona Press.
- 685
686
- 687 Sohl, F., Spohn, T., Breuer, D., & Nagel, K. (2002). Implications from galileo observations on the interior structure and chemistry of the galilean satellites.
- 688
689 *Icarus*, 157(1), 104 - 119. Retrieved from <http://www.sciencedirect.com/science/article/pii/S0019103502968284> doi: <https://doi.org/10.1006/icar.2002.6828>
- 690
691
- 692 Sparks, W. B., Hand, K. P., McGrath, M. A., Bergeron, E., Cracraft, M., & Deustua, S. E. (2016, September). Probing for evidence of plumes on Europa with HST/STIS. *The Astrophysical Journal*, 829(2), 121. Retrieved from <http://dx.doi.org/10.3847/0004-637X/829/2/121> (Publisher: American Astronomical Society) doi: 10.3847/0004-637x/829/2/121
- 693
694
695
696
- 697 Tobie, G., Choblet, G., & Sotin, C. (2003). Tidally heated convection: Constraints on Europa's ice shell thickness. *Journal of Geophysical Research: Planets*, 108(E11). Retrieved 2019-01-08, from <https://doi.org/10.1029/2003JE002099> doi: 10.1029/2003JE002099
- 698
699
700
- 701 Tobie, G., Mocquet, A., & Sotin, C. (2005). Tidal dissipation within large icy satellites: Applications to Europa and Titan. *Europa Icy Shell*, 177(2), 534–549. Retrieved from <http://www.sciencedirect.com/science/article/pii/S0019103505001582> doi: 10.1016/j.icarus.2005.04.006
- 702
703
704
- 705 Townsend, M., & Huber, C. (2020, February). A critical magma chamber size for volcanic eruptions. *Geology*, 48(5), 431–435. Retrieved 2020-05-20, from <https://doi.org/10.1130/G47045.1> doi: 10.1130/G47045.1
- 706
707
- 708 Trumbo, S. K., Brown, M. E., Fischer, P. D., & Hand, K. P. (2017). A new spectral feature on the trailing hemisphere of Europa at 3.78 μm . *The Astronomical Journal*, 153(6), 250. Retrieved from <https://doi.org/10.3847/1538-3881/aa6d80> doi: 10.3847/1538-3881/aa6d80
- 709
710
711
- 712 Trumbo, S. K., Brown, M. E., & Hand, K. P. (2019). Sodium chloride on the surface of Europa. *Science Advances*, 5(6). Retrieved from <https://advances.sciencemag.org/content/5/6/eaaw7123> doi: 10.1126/sciadv.aaw7123
- 713
714
- 715 Vance, S. D., Hand, K. P., & Pappalardo, R. T. (2016, May). Geophysical controls of chemical disequilibria in Europa. *Geophysical Research Letters*, 43(10), 4871–4879. Retrieved 2019-03-27, from <https://doi.org/10.1002/2016GL068547> doi: 10.1002/2016GL068547
- 716
717
718
- 719 Vance, S. D., Panning, M. P., Stähler, S., Cammarano, F., Bills, B. G., Tobie, G., ... Banerdt, B. (2018). Geophysical investigations of habitability in ice-covered ocean worlds. *Journal of Geophysical Research: Planets*, 123(1), 180-205. Retrieved from <https://agupubs.onlinelibrary.wiley.com/doi/abs/10.1002/2017JE005341> doi: 10.1002/2017JE005341
- 720
721
722
723
- 724 Vance, S. D., Styczinski, M., Melwani Daswani, M., & Vega, K. (2020, September). *vancesteven/PlanetProfile: Supplementary Data: Magnetic Induction Responses of Jupiter's Ocean Moons Including Effects from Adiabatic Convection*. Zenodo. Retrieved 2021-05-08, from <https://zenodo.org/record/4052711> doi: 10.5281/ZENODO.4052711
- 725
726
727
728
- 729 Wakita, S., & Genda, H. (2019, August). Fates of hydrous materials during planetesimal collisions. *Icarus*, 328, 58–68. Retrieved from <http://www.sciencedirect.com/science/article/pii/S0019103518306523> doi: 10.1016/j.icarus.2019.03.008
- 730
731
732
- 733 Zahnle, K. J., & Catling, D. C. (2017, July). The Cosmic Shoreline: The Evidence that Escape Determines which Planets Have Atmospheres, and what this May Mean for Proxima Centauri B. *The Astrophysical Journal*, 843(2), 122. Retrieved from <http://dx.doi.org/10.3847/1538-4357/aa7846> (Publisher: American Astronomical Society) doi: 10.3847/1538-4357/aa7846
- 734
735
736
737
- 738 Zolotov, M. Y., & Kargel, J. S. (2009). On the chemical composition of Europa's icy

- 739 shell, ocean, and underlying rocks. In R. T. Pappalardo, W. B. McKinnon, &
740 K. Khurana (Eds.), *Europa* (p. 431). University of Arizona Press Tucson, AZ.
741 Retrieved from <https://uapress.arizona.edu/book/europa>
- 742 Zolotov, M. Y., & Shock, E. L. (2001). Composition and stability of salts on
743 the surface of Europa and their oceanic origin. *Journal of Geophysical*
744 *Research: Planets*, 106(E12), 32815–32827. Retrieved 2018-10-19, from
745 <https://doi.org/10.1029/2000JE001413> doi: 10.1029/2000JE001413
- 746 Zolotov, M. Y., & Shock, E. L. (2004). A model for low-temperature biogeochem-
747 istry of sulfur, carbon, and iron on Europa. *Journal of Geophysical Research:*
748 *Planets*, 109(E6). Retrieved 2018-10-19, from [https://doi.org/10.1029/](https://doi.org/10.1029/2003JE002194)
749 2003JE002194 doi: 10.1029/2003JE002194

Figure 1.

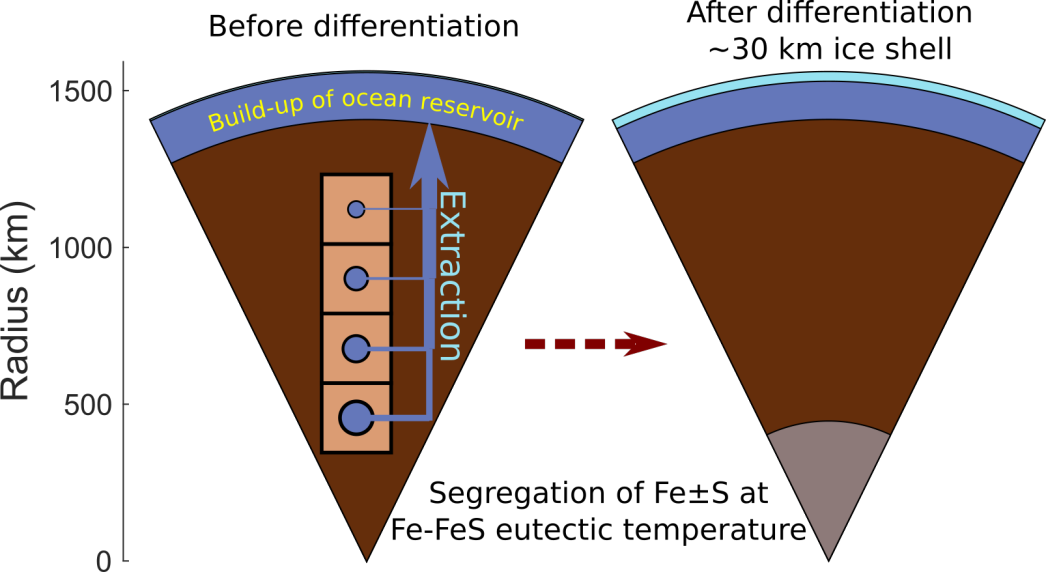


Figure 2.

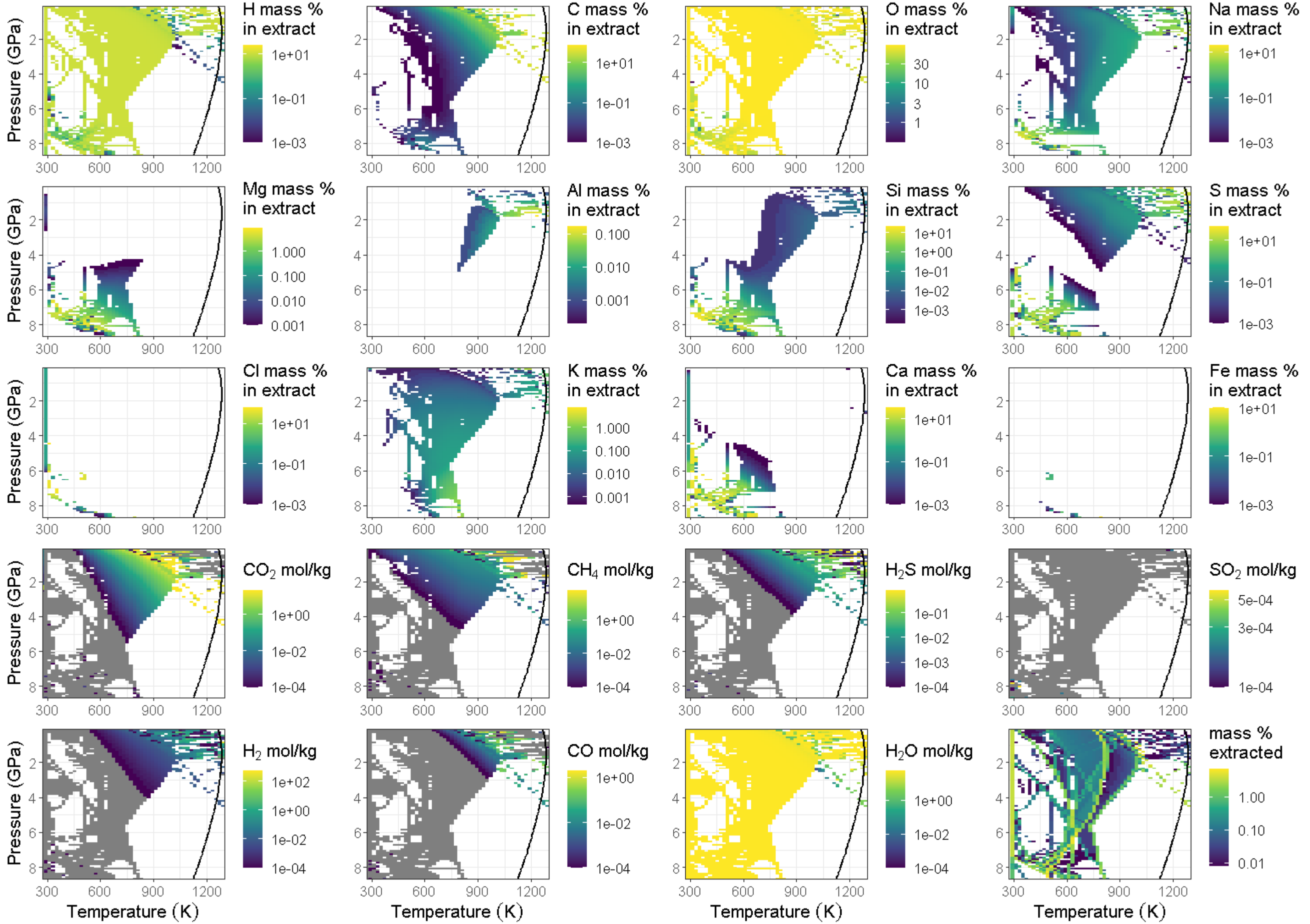
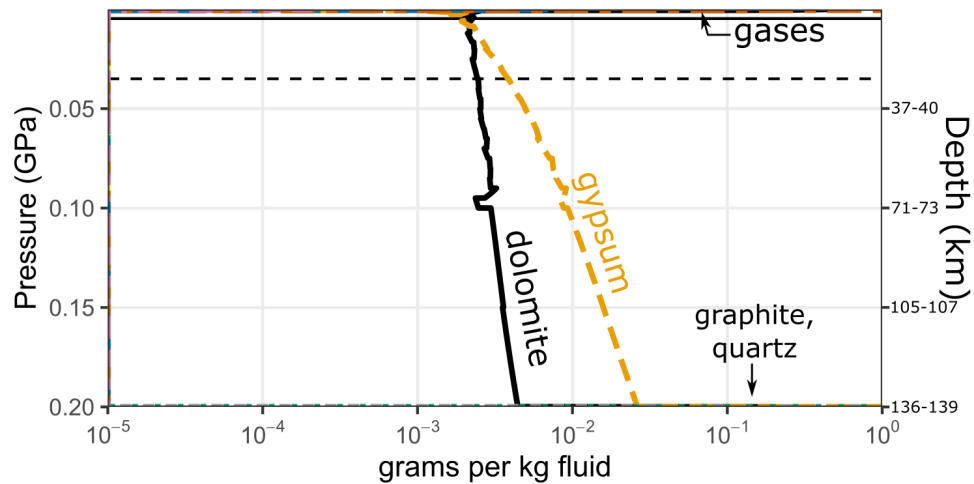
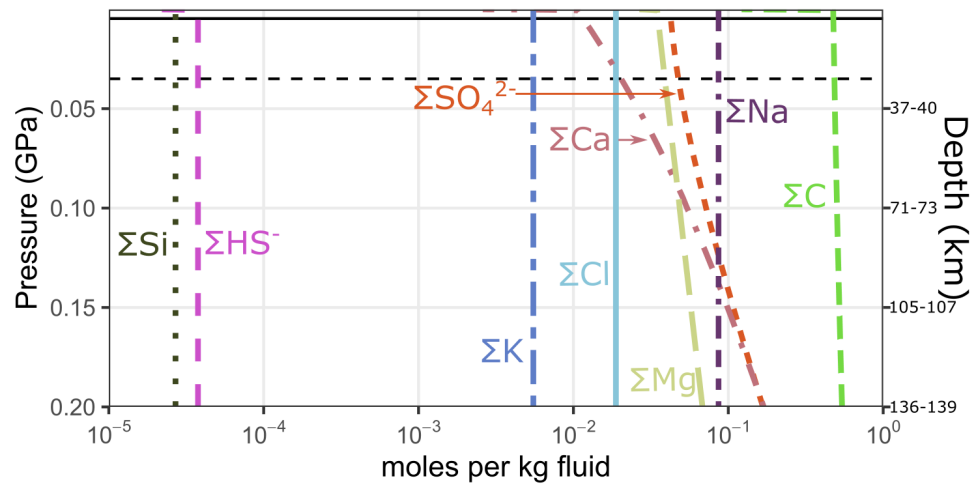


Figure 3.

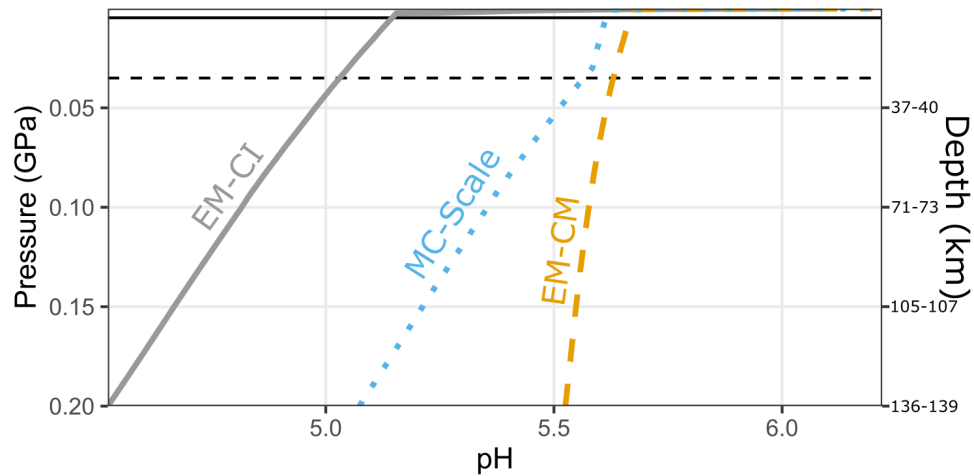
a) Minerals and gases



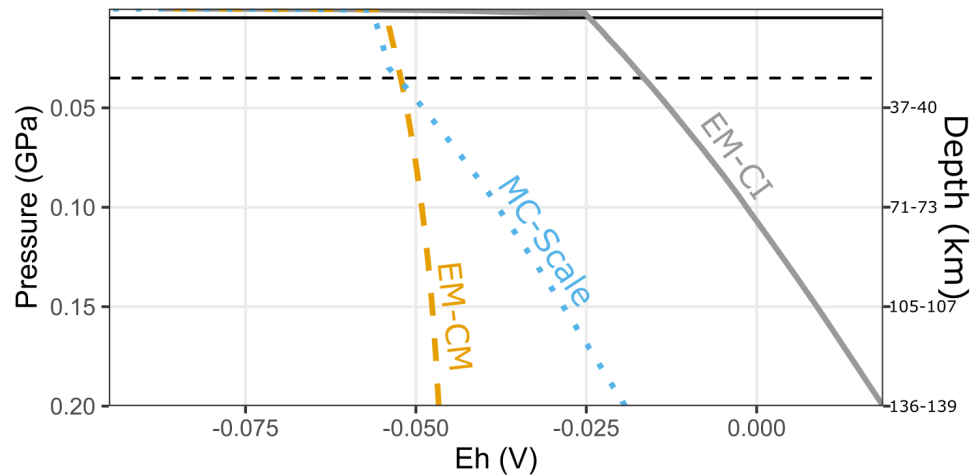
b) Dissolved components



c) pH



d) Redox potential



Supporting Information for “A metamorphic origin for Europa’s ocean”

Mohit Melwani Daswani¹, Steven D. Vance¹, Matthew J. Mayne², Christopher R. Glein³

¹Jet Propulsion Laboratory, California Institute of Technology, Pasadena, CA, USA

²Department of Earth Sciences, Stellenbosch University, RSA

³Space Science and Engineering Division, Southwest Research Institute, San Antonio, TX, USA

Contents

1. Table S1: Review of reported post-*Galileo* nested spherical shell models for Europa
2. Figure S1: Method flowchart
3. Table S2: Compositions of the satellitesimals used in the accretion model
4. Text S1: Additional details about the initial bulk composition models
5. Table S3: Initial bulk compositions for *EM-CI*, *EM-CM* and *MC-Scale*
6. Text S2: Isobaric heating/prograde metamorphism fluid extraction model parameters
7. Table S4: *Perple_X* solution models used
8. Text S3: Core composition
9. Figure S2: Pseudosections of Fe \pm S for core formation
10. Figure S3: Quantification of Fe \pm S melt for core formation
11. Text S4: Modifications to *PlanetProfile*
12. Text S5: Additional results of the coupled prograde metamorphism-plus-fluid extraction models
13. Figure S4: Extracted fluid composition for *EM-CI*, *FMQ-2*, R/E = 0
14. Figure S5: Ocean column composition for *EM-CI*, *FMQ-2*, R/E = 0
15. Figure S6: Absolute mass of elements extracted for all prograde metamorphism models
16. Table S5: Mass and elemental composition of the extracted bulk fluid in context
17. Figure S7: Extracted fluid composition for *EM-CI* R/E = 0
18. Figure S8: Extracted fluid composition for *EM-CI* R/E = 0.1
19. Figure S9: Extracted fluid composition for *EM-CI*, Retaining 5 % fluid
20. Figure S10: Extracted fluid composition for *MC-Scale* R/E = 0
21. Figure S11: Effect of fluid extraction on the deep interior’s density
22. Figure S12: Changing mineralogy at 500 MPa in prograde metamorphism/fluid extraction
23. Figure S13: Changing mineralogy at 3 GPa in prograde metamorphism/fluid extraction
24. Text S6: Mechanisms and limits of volatile sequestration and loss to space
25. Figure S14: Density of CO₂ clathrates in Europa’s ocean
26. Text S7: Compensating for insufficient volatiles extracted from *MC-Scale* with comets
27. Figure S15: Ocean column composition for *MC-Scale* plus cometary material
28. Table S6: Adjusted mass of Europa’s hydrosphere for *MC-Scale* plus cometary material
29. Figure S16: Final radial properties of Europa

Corresponding author: M. Melwani Daswani, mohit.melwani.daswani@jpl.caltech.edu

Table S1: Review of reported post-*Galileo* nested spherical shell models for Europa

Analysis of gravitational coefficients inferred from *Galileo* radio science data permit only radial models of composition (Anderson et al., 1998; Zhang, 2003; Sotin & Tobie, 2004; Kuskov & Kronrod, 2005; Schubert et al., 2009; Vance et al., 2018). Such models are non-unique and subject to uncertainty about the bulk composition and mineralogy of the deep interior of Europa (e.g., Zolotov & Kargel, 2009), for which mantle and core densities must be assumed (e.g., Schubert et al., 2009). The following table summarizes plausible spherical shell models from the literature consistent with *Galileo* data.

Table 1. Review of reported post-*Galileo* nested spherical shell models for Europa.

Source	Core ρ kg/m ³	Core radius km	Mantle ρ kg/m ³	Mantle radius km	Ocean ρ kg/m ³	Ocean depth km	Ice ρ kg/m ³	Ice thickness km
A1998 ^a	5150	0–827	3080–3800	660–1400	900–1300 ^b	80–200 ^b	b	b
A1998	8000	0–593	3000–3800	860–1400	900–1270 ^b	80–200 ^b	b	b
T2003 ^c	5500	650	3500	1415	1000	120–130	920	20–30
H2004 ^d	5150	599	3542	1421	1000	40–120	1000	20–100
K2005 ^e	5700	555–660	3320–3400	1435–1450	$f(P, T)$ EOS	115–130 ^b	$f(P, T)$ EOS	b
K2005	5700	505–630	3400–3480	1425–1440 ^f	$f(P, T)$ EOS	125–140 ^b	$f(P, T)$ EOS	b
K2005	5700	470–610	3450–3520	1425–1435	$f(P, T)$ EOS	130–140 ^b	$f(P, T)$ EOS	b
K2005	4700	455–670	3600–3670	1405–1420 ^f	$f(P, T)$ EOS	145–160 ^b	$f(P, T)$ EOS	b
K2005	5700	560–670	3320–3400	1450–1465	$f(P, T)$ EOS	100–115 ^b	$f(P, T)$ EOS	b
K2005	5700	510–640	3400–3480	1440–1460 ^f	$f(P, T)$ EOS	105–125 ^b	$f(P, T)$ EOS	b
K2005	5700	490–620	3450–3520	1440–1455	$f(P, T)$ EOS	110–125 ^b	$f(P, T)$ EOS	b
K2005	4700	470–670	3600–3670	1425–1440 ^f	$f(P, T)$ EOS	125–140 ^b	$f(P, T)$ EOS	b
T2005 ^g	5150		3300		1000		1000	
T2005	5150		3300		1000		1000	
T2005	8000		3300		1000		1000	
T2005	8000		3300		1000		1000	
S2009 ^h	8000	706	2500	1561	1000 ^b	0.7 ^b		
S2009	4700	1012	2500	1529	1000 ^b	33 ^b		
S2009	8000	437	3500	1427	1000 ^b	135 ^b		
S2009	4700	702	3500	1425	1000 ^b	137 ^b		
S2009	8000	245	3760	1401	1000 ^b	161 ^b		
S2009	4700	409	3760	1401	1000 ^b	162 ^b		
V2018 ⁱ	8000	479	3426	1428	1130	103		30
V2018	8000	478	3426	1426	1130 ^h	131		5
V2018	8000	475	3427	1434	1020 ^h	97		30
V2018	8000	476	3426	1433	1020 ^h	124		5
V2018	8000	478	3427	1432	1060 ^h	99		30
V2018	8000	478	3426	1431	1060 ^h	126		5

^aAnderson et al. (1998).

^bIncludes both liquid ocean and ice.

^cTobie, Choblet, and Sotin (2003).

^dHussmann and Spohn (2004).

^eKuskov and Kronrod (2005).

^fIncludes differentiated crust.

^gTobie, Mocquet, and Sotin (2005), for a generic Europa with mantle + core radius = 1600 km and average density = 3000 kg/m³.

^hSchubert et al. (2009). Silicate density and core density are independent variables.

ⁱVance et al. (2018). Ice thickness and core density are independent variables. Ocean density is a function of depth and composition of the ocean; mean values reported here are taken from Figure 7 in V2018.

Figure S1: Method flowchart

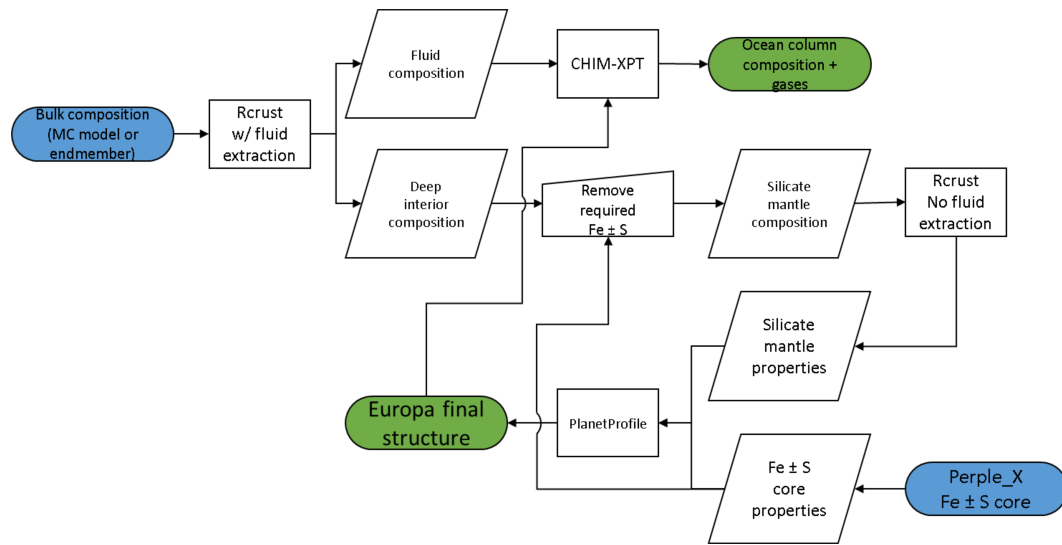


Figure 1. Method flowchart. Blue = start. Green = end results.

Table S2: Compositions of the satellitesimals used in the accretion model

Table 2. Adopted compositions of the satellitesimals used in the accreted composition model (*MC-Scale*), based on the compositions of carbonaceous chondrites and comet 67/Churyumov-Gerasimenko. Element concentrations in wt. %, total normalized to 100 wt. %. Compositions for chondrites are from Lodders and Fegley (1998), except for CI chondrites, which are from Palme et al. (2014). Chlorine concentrations for chondrites are from Clay et al. (2017). Comet 67P/Churyumov-Gerasimenko’s composition and density is a synthesis from Pätzold et al. (2016); Dhooghe et al. (2017); Le Roy et al. (2015); Bardyn et al. (2017), using a dust-to-ice mass ratio of 4 from Pätzold et al. (2016). Densities of chondrites are from Flynn et al. (2018). Nitrogen in the resulting composition from the accretion model was not included in the input for the geochemical evolution model. Sulfate salts found in CI chondrites have been attributed to terrestrial alteration of native sulfides (Fredriksson & Kerridge, 1988; Airieau et al., 2005; Zolensky et al., 1993; Gounelle & Zolensky, 2001; Brearley, 2006), but note that: 1) the thermodynamic models are insensitive to initial mineralogy, and in fact predicts sulfides and not sulfates at initial equilibration (§, and Fig. S12–S13), and 2) the CI chondrite composition from Palme et al. (2014) represents a careful compilation of best values from multiple studies, compares excellently to solar photosphere abundances, and is a standard for CI chondrite compositions. Note that there is more uncertainty in the oxygen abundance of the solar photosphere than the CI chondrites (Palme et al., 2014).

Element (wt. %)	CI	CV	CM	CK	CR	CO	67P/C-G
H	2.006	0.287	1.428	0.285	0.319	0.071	11.283
C	3.543	0.544	2.244	0.224	2.038	0.447	27.814
N	0.300	0.008	0.155	0.008	0.063	0.009	1.021
O	46.737	37.980	44.073	39.802	39.280	37.578	41.652
Na	0.505	0.349	0.398	0.315	0.336	0.427	0.696
Mg	9.714	14.679	11.733	14.942	13.961	14.727	0.985
Al	0.855	1.725	1.153	1.494	1.172	1.422	0.178
Si	10.895	16.116	12.957	16.060	15.286	16.047	10.434
S	5.448	2.258	2.755	1.728	1.937	2.234	1.789
Cl	0.012	0.005	0.019	0.005	0.007	0.005	0.031
K	0.057	0.037	0.038	0.029	0.032	0.037	0.031
Ca	0.928	1.889	1.316	1.728	1.315	1.605	0.082
Fe	19.000	24.123	21.731	23.379	24.254	25.391	6.035
Density (kg/m ³)	1570	2970	2270	2900	3110	3100	533
Distance from Jupiter (AU)	12	0.6	0.76	0.6	0.84	0.72	12–27

Text S1: Additional details about the initial bulk composition models.

To establish what the composition (including water mass fraction) of the building blocks might have been, we use the hydrodynamic–geochemical sorting model of Desch, Kalyaan, and Alexander (2018), which provides an independent constraint on the distribution of materials in the early solar system, and specifically, the location of the formation of carbonaceous chondrites beyond the pressure bump created by Jupiter’s formation. This pressure bump would have impeded the transport of non-carbonaceous material from the inner solar system to Jupiter’s circumplanetary disk (~ 3 AU Desch et al., 2018). We assume that Europa’s formation entailed preferential gravitational attraction of materials closest to its location, so we apply a Monte Carlo accretion model (*MC-Scale*) in which the prior probability of different accreting chondritic particle compositions is scaled by the reciprocal of their squared distance from Jupiter, according to the model by (Desch et al., 2018). We also include cometary satellitesimals. Compositions and formation distances for each of the compositional endmembers are given in Table S2.

We assume that Europa’s mass and radius have not changed significantly since accretion. Here, the radius of the growing embryo of Europa scales with mass, modifying the power law from Sotin, Grasset, and Mocquet (2007) to fit Europa’s current mass and radius¹:

$$r_e = r_{\oplus}(1.072(M_e/M_{\oplus})^{0.306}) \quad (1)$$

where r_e and M_e are the radius and mass of Europa’s embryo at any one time during accretion, and r_{\oplus} and M_{\oplus} are the radius and mass of Earth.

1. *MC-Scale*, where we assume that Europa’s formation entailed preferential gravitational attraction of materials closest to its location (see Canup & Ward, 2009; Estrada et al., 2009; McKinnon & Zolensky, 2003). We carry out 10^4 iterations, where the probability of different chondritic satellitesimal compositions is scaled by their distance of formation beyond the pressure bump created by Jupiter’s formation, according to the hydrodynamic/geochemical sorting model of Desch et al. (2018). We also consider cometary satellitesimals, which we assume form initially at 15–30 AU. The prior probability for accreting particle compositions is scaled by the reciprocal of their squared distance from Jupiter. Compositions and formation distances for each of the compositional endmembers are given in Table S2.
2. *EM-CI*, where the only satellitesimals are CI carbonaceous chondrites, which are the most water-rich chondrites. To explore the volatile evolution of a geochemically reduced but volatile-rich Europa, we additionally explored a hypothetical reduced CI chondrite at 2 log units below the Fayalite-Magnetite-Quartz redox buffer (FMQ–2).
3. *EM-CM*, where the only satellitesimals are CM carbonaceous chondrites.

The accretion model assumes a spherical Europa constructed with satellitesimals formed from uniform pebbles 0.005–0.5 m in radius, consistent with accretion from mostly dehydrated material (0–50 % water) of otherwise solar composition (i.e., approximately chondritic) inside of the circumjovian snowline (Ronnet et al., 2017). The small size of the pebbles matters because: 1) the impact energy of single particles will not raise the growing body’s temperature to the extent that volatile loss during accretion is substantial, 2) small particles are less likely to have been thermally processed

¹ 4.80×10^{22} kg $\pm 1.26 \times 10^{20}$, and 1560.8 ± 0.5 km, respectively. Radius retrieved from NASA/JPL SSD (https://ssd.jpl.nasa.gov/?sat_phys_par). Mass calculated from GM (3202.739 ± 0.009 km³/s²) reported in the same source.

prior to accretion by the decay of short-lived radionuclides if accretion was protracted, and 3) the large number of pebbles required to form Europa’s mass decreases the likelihood of statistical outliers dominating Europa’s bulk composition. We use these simple models only to resolve the plausible range of initial bulk compositions—not the accretion process itself, nor the timing of Europa’s formation beyond that implied by using known carbonaceous chondrite and comet compositions as building blocks. This assumption is reasonable because either the accretion of the jovian satellites (Canup & Ward, 2009) or the delivery of solids to the circumjovian disk (Estrada et al., 2009) were protracted. If the Galilean satellites formed earlier than the carbonaceous chondrites, the non-carbonaceous parent bodies of primitive achondrites that predated the formation of carbonaceous chondrites probably had a similar volatile content to carbonaceous chondrites (e.g., Day et al., 2019). The resulting initial bulk compositions are summarized in Table S3.

Table S3: Initial bulk compositions for *EM-CI*, *EM-CM* and *MC-Scale*

Table 3. Bulk initial compositions of Europa, post-accretion, used as inputs in the geochemical evolution models. Compositions based on CI and CM carbonaceous chondrites, and a Monte Carlo accretion model. The composition of the FMQ–2 CI chondrite (*EM-CI*, *FMQ–2*) is pressure dependent, calculated at 273 K, from 1 bar to 86700 bar, adjusting the oxygen concentration of *EM-CI* with the equilibrium expression $\log_{10} f\text{O}_2 = -26455.3/T + 8.344 + 0.092 \times ((P - 1)/T)$, from Frost (1991), where T is temperature in K and P is pressure in bar. The composition for *EM-CI*, *FMQ–2* shows the minimum and maximum throughout the pressure range.

Element (wt. %)	<i>EM-CI</i>	<i>EM-CM</i>	<i>MC-Scale</i>	<i>EM-CI</i> , <i>FMQ–2</i>
H	2.01	1.43	0.391	2.421–2.562
C	3.56	2.25	0.874	4.288–4.537
O	46.92	44.14	39.360	32.365–36.071
Na	0.51	0.40	0.360	0.614–0.650
Mg	9.79	11.75	14.297	11.793–12.477
Al	0.87	1.15	1.452	1.048–1.109
Si	10.94	12.98	15.586	13.179–13.943
S	5.47	2.76	2.133	6.589–6.971
Cl	0.01	0.02	0.007	0.012–0.013
K	0.06	0.04	0.001	0.072–0.076
Ca	0.94	1.32	1.636	1.132–1.198
Fe	18.91	21.76	23.903	22.779–24.100

Text S2: Isobaric heating/prograde metamorphism fluid extraction model parameters

Buoyancy drives fluids away from Europa’s center, with transport being particularly rapid in permeable materials in the direction of maximum compressive stress (e.g. Richard et al., 2007). Fluids resulting from mineral devolatilization increase pore fluid pressures (e.g. Leclère et al., 2018) which can propagate porosity waves under compaction (Connolly & Podladchikov, 1998), and also hydrofractures (e.g. Miller et al., 2003) and stresses that embrittle the overburden (Ferrand et al., 2017) and facilitate fluid migration. Gravitational settling of solids in Europa’s interior creates resistance to deformation caused by increased pore fluid pressure, and this produces compaction pressure gradients that force fluids up through the most permeable paths. Focused channelization of fluids connecting disparate fluid production depths may also occur under compaction (Wilson et al., 2014; Miller et al., 2003), especially if the devolatilized fluid is less viscous than the medium. Retention of fluids at high pressure would lead to an unstable solution that is out of hydrostatic equilibrium. Thus, the only path for free low density fluids is up.

Perple_X

The composition and abundance of volatile elements released and extracted from the silicate interior during the thermal evolution of Europa were calculated using version 6.8.7 of the `Perple_X` Gibbs free energy minimization code (Connolly, 2009) together with a lagged speciation algorithm (Connolly & Galvez, 2018) and the Deep Earth Water model (DEW; Pan et al., 2013; Sverjensky et al., 2014) to quantify electrolytic fluids produced. We also use a generic hybrid molecular fluid equation of state model including $\text{CO}_2\text{-CH}_4\text{-H}_2\text{-CO-H}_2\text{O-H}_2\text{S-SO}_2$ fluid with non-linear subdivisions (COH-Fluid+). Activity-composition models, and solution model thermodynamic data for mineral phases and silicate melt phases were mainly selected from the “igneous set” implemented in `Perple_X`, adapted mainly from Holland, Green, and Powell (2018), shown in Table 4, and which is also used in the phase equilibrium software THERMOCALC. The “igneous set” of equations of state (the other two families are the “metapelite set” and the “metabasite set”) is calibrated up to 6 GPa, and is the most appropriate for the pressure and temperature range, and the wide compositional space, explored here (García-Arias, 2020). For carbonates, we use the solution models Do(HP) and M(HP) derived from Holland, Baker, and Powell (1998), including the calcite (CaCO_3), aragonite (CaCO_3), magnesite (MgCO_3), dolomite ($\text{CaMg}(\text{CO}_3)_2$), ankerite ($\text{CaFe}(\text{CO}_3)_2$) and siderite (FeCO_3) endmembers. Some mineral, organic and melt end-members (e.g., fo8L, qjL) were excluded because of their incompatibility with the solution models used, or suspect stability. The h2oL melt end-member was also excluded because of overstabilizing melt at low temperature.

`Perple_X` has been used extensively to constrain the decarbonation and dehydration of mantle rocks and subducting crust on Earth, and validation of thermodynamic models and code are available in the literature. The most relevant calibration and validation of the dehydration and decarbonation reactions are found in Connolly (2005); Bjerga (2014); Bjerga, Konopásek, and Pedersen (2015); Bretscher, Hermann, and Pettker (2018). Gorce, Caddick, and Bodnar (2019) verified that thermodynamic models of decarbonation and dehydration with `Perple_X` approximate field volatile flux measurements closely: like in the models presented in this work, carbon release is facilitated by low to moderate temperature deserpentinization, or high temperature destabilization of carbonates. Recent tests with `Perple_X` for serpentine stability and the devolatilization of talc-carbonate rocks relevant to those presented in this work can be found in Nozaka, Wintsch, and Meyer (2017) and Menzel, Garrido, and López Sánchez-Vizcaíno (2020). `Perple_X` may underestimate the stability of hydrated phases at high pressure (6–8 GPa) and moderately high temperature (873–1073 K) (Cerpa et al., 2020),

but our differentiation thermodynamic models proceed to temperatures high enough (~ 1250 K) to offset dehydration overestimations at moderate temperatures.

Rcrust

The **Rcrust** program (version 2019-12-04) (Mayne et al., 2016) was used to calculate the isobaric prograde heating paths from 273.15 K up to 1473.15 K in 20 K increments (ΔT). No fluids were extracted at the 273.15 K isotherm to equilibrate the composition at all pressures initially; fluid extraction is first allowed to occur at the first temperature increment (293.15 K). At each depth (93 MPa increments from the surface to the core-silicate boundary) in the silicate interior, where pressure is assumed to remain constant, prograde reactions with increasing temperature are net fluid-producing, therefore fluids permeating from underlying layers are assumed to not have significant interactions with overlying layers, as fluids are already in excess. The spacing of the temperature and pressure increments was chosen to obtain accurate results while keeping model run times and output file sizes reasonable ($\lesssim 30$ h and $\lesssim 1$ GB respectively). Given the wide PT space explored here, the model PT spacing is reasonable in order to constrain volatile mass fluxes, instead of the precise PT location of potentially thousands of phase reactions and relations.

Rcrust was used to retain and extract fluids during metamorphism. A retention-to-extraction ratio equal to zero does not signify that all volatiles are extracted, but that all free fluids are extracted. The retention of much free fluid at depth is unstable and geophysically implausible, and we find that even the “*EM-CI*, Retain 5 wt. %” model allows for excessive free fluid at depth (Fig. S9 and S11), which would be expelled in geologically short timescales under compaction as occurs on Earth (e.g. Warner, 2004). For context, the majority of water in Earth’s lower crust and mantle is in minerals, not in free fluids. Minerals may have a high volatile retention capacity (as seen in the phase abundance plots in Figures S12 and S13). Retention of free fluids causes much of the silicate layer to have a density that is too low for Europa (< 3000 kg/m³; Fig. S11); a present-day hydrated silicate interior for Europa is implausible given gravity and density measurements, and thermal history implied by a metallic core (Anderson et al., 1998; Sohl et al., 2002; Schubert et al., 2009; Kuskov & Kronrod, 2005; Vance et al., 2018).

CHIM-XPT

For the ocean column compositions, we do not use the DEW because it is not calibrated for low pressures (from the seafloor to the surface). Instead we use the **CHIM-XPT** model and **SOLTHERM** database (Reed, 1998, see main text). We equilibrate (respeciate) the extracted metamorphic fluids at the seafloor at 273.16 K and do not suppress minerals, gases or species on the basis of kinetic inhibition at low temperature (e.g., dolomite, reduced carbon species, etc.), since the fluids were produced and extracted at high temperature during metamorphism. **CHIM-XPT** is a multiphase equilibrium mass action code, used here to compute the speciation of fluids from 200 MPa (assumed maximum pressure at the seafloor) to 0.1 MPa (the surface of a hypothetical ice-free ocean), including mineral precipitation and gas boiling. These are tasks for which **CHIM-XPT** is particularly well-suited, given its validation against samples obtained in the same pressure range, including borehole and petrologic data in hydrothermal/geothermal systems (Freedman et al., 2009; Fowler et al., 2019), seafloor alteration by diverse fluid compositions (Palandri & Reed, 2004) and experiments simulating CO₂ injection into natural and synthetic samples (Verba et al., 2014). We caution that as with other geochemistry/thermodynamic equilibrium programs, **CHIM-XPT** results may be non-unique. For example, **CHIM-XPT** predicts that any of various mineral-water reactions would yield the serpentine mineral assemblage observed in altered ophiolites (Sonzogni et al., 2017).

Table S4: Perple_X solution models used**Table 4.** Solution models used in the `Perple_X` thermodynamic phase equilibrium calculations using the `DEW17HP622ver_elements` thermodynamic data. For the core, we use the `SE15ver` (Saxena & Eriksson, 2015) data instead.

Solution model	Type	Source
Atg(PN)	Antigorite	Padrón-Navarta et al. (2013)
Bi(HGP)	Biotite	Holland et al. (2018)
Chl(HP)	Chlorite	Holland et al. (1998)
COH-Fluid+	CO ₂ -CH ₄ -H ₂ -CO-H ₂ O-H ₂ S-SO ₂ fluid with non-linear subdivisions	Connolly and Galvez (2018)
Cpx(HGP)	Clinopyroxene	Holland et al. (2018)
Do(HP)	Dolomite-ankerite	Holland et al. (1998)
Gt(HGP)	Garnet	Holland et al. (2018)
M(HP)	Magnesite-siderite-rhodochrosite	Holland et al. (1998)
melt(HGP)	Generic silicate melt	Holland et al. (2018)
Mica(CF)	Fe-Mg-K-Na mica	Chatterjee and Froese (1975); Holland et al. (1998)
O(HGP)	Olivine	Holland et al. (2018)
Omph(GHP)	Omphacite	Green, Holland, and Powell (2007)
Opx(HGP)	Orthopyroxene	Holland et al. (2018)
Pl(JH)	Plagioclase	Jennings, Holland, Shorttle, MacLennan, and Gibson (2016)
Pu	Pumpellyite	DEW17HP622ver_elements
Sp(HGP)	Spinel	Holland et al. (2018)
Stlp	Stilpnomelane	DEW17HP622ver_elements
T	Talc	DEW17HP622ver_elements

Text S3: Core composition

Europa’s core has variously been approximated as a body composed entirely of Fe (Anderson et al., 1998; Vance et al., 2018), stoichiometric FeS (Kuskov & Kronrod, 2005), 90 wt. % Fe + 10 wt. % S (Kuskov & Kronrod, 2005), or a Fe-SeS eutectic composition (Anderson et al., 1998). However, experimental work has suggested that the core of Europa may be pyrrhotite-rich (Scott et al., 2002). In addition, the pyrrhotite group (Fe_(0.8–1)S), including its stoichiometric endmember troilite (FeS), is the most abundant Fe-sulfide in chondrite meteorites (e.g. Bland et al., 2004; Singerling & Brearley, 2018). Therefore, we assume that prograde metamorphism proceeded at least up to the Fe-SeS eutectic temperature in order for core formation to proceed. Additionally, pyrrhotite polymorphs are the thermodynamically stable sulfide phases up to the Fe-SeS eutectic temperature under the range of pressures of Europa’s interior (Figures S2–S3). Since core formation occurs at higher temperatures than volatile-releasing metamorphic reactions (see Main Text §2.2), core formation does not sequester volatiles that would build the ocean.

The Fe ± S melt phase contains 24–32 mass % sulfur at the < 8 GPa range of pressures within Europa (Figures S2–S3). We do not find a compelling reason on the basis of cosmochemistry to disallow other light elements (oxygen, silicon, carbon, hydrogen) from partitioning into the core, in addition to or in substitution of sulfur, as has been postulated for Earth and Mars (e.g., Wood et al., 2013; Li & Fei, 2014; Badro et al., 2015; Steenstra & van Westrenen, 2018). However, the Fe–S system is simple and well-studied (e.g., Walder & Pelton, 2005) and can provide an initial approximation for an expected core composition, mass and density, until a future mission can constrain the deep interior composition of Europa from its seismic properties and improved gravity data.

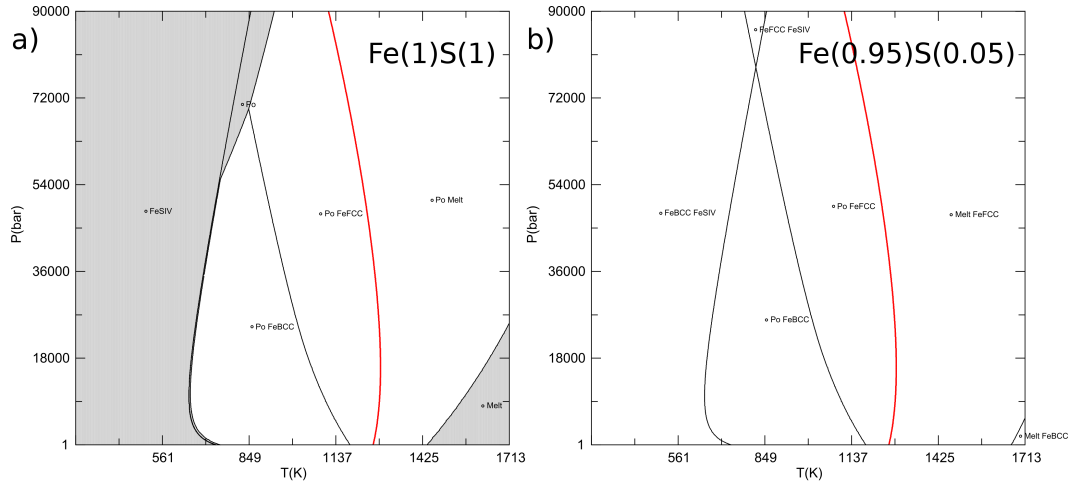
Figure S2: Pseudosections of $\text{Fe} \pm \text{S}$ for core formation

Figure 2. Pseudosection diagrams of a) stoichiometric FeS, and b) $\text{Fe}_{0.95}\text{S}_{0.05}$ calculated with *Perple_X* 6.8.7. and thermodynamic constraints from Saxena and Eriksson (2015). Red curve is the Fe–S solidus, also the location of the Fe–SeS eutectic temperature. We assume that prograde metamorphism proceeded at least up to the Fe–SeS eutectic temperature (also the location of the solidus of $\text{Fe}_{(1,0.5)}\text{S}_{(0,0.5)}$) in order to lead to the formation of a Fe-rich core, since Fe–SeS melt pockets must percolate through the body to coalesce separately from silicates. Pyrrhotite polymorphs are the thermodynamically stable sulfide phases up to the Fe–SeS eutectic temperature under the range of pressures of Europa’s interior. FeSIV = polymorph IV of stoichiometric FeS, Po = pyrrhotite, FeBCC = body-centered cubic allotrope of Fe, FeFCC = face-centered cubic allotrope of Fe.

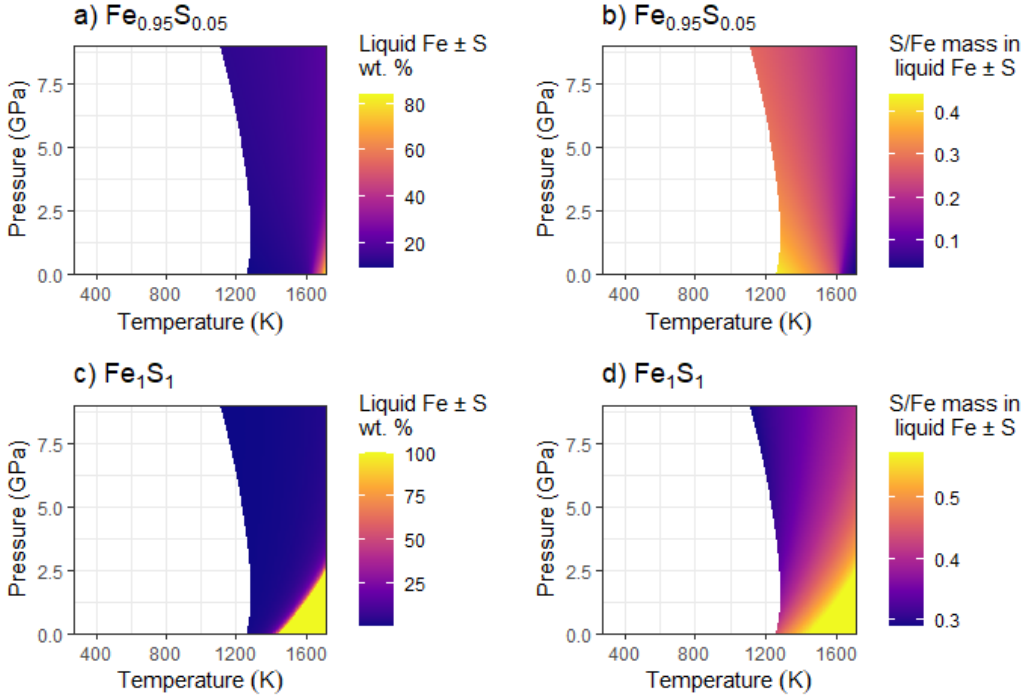
Figure S3: Quantification of Fe \pm S melt for core formation

Figure 3. Weight % of Fe \pm S melt, and mass fraction of sulfur in Fe \pm S melt at and above the Fe-SeS eutectic temperature for pressure conditions relevant to Europa’s interior, calculated with *Perple_X* 6.8.7. and thermodynamic constraints from Saxena and Eriksson (2015). We find that Fe \pm S melt phase contains 24–32 mass % sulfur at the Fe-SeS eutectic at range of pressures within Europa. a) and b) bulk composition = $\text{Fe}_{0.95}\text{S}_{0.05}$; c) and d) bulk composition = stoichiometric FeS.

Text S4: Modifications to PlanetProfile

PlanetProfile calculations were made using the newly computed mantle and core properties from this work. Interior properties shown in Figure S11 are for the CM model, assuming a seawater composition (36.165 g/kg), with temperatures at the bottom of the icy lithosphere set at {270.8,268.2} K for ice thicknesses of {5,30} km. Corresponding core and mantle radii are 450 km and 1410 km, and output moments of inertia (MoI) C/MR^2 are {0.3455,0.3457} for the applied precision of the model. Geotherms in the solid interior are computed for the assumption of 100 GW heat at the seafloor.

Text S5: Additional results of the coupled prograde metamorphism-plus-fluid extraction models

Here we describe additional details about the results of the prograde metamorphism models leading to fluid production and extraction. Figure S6 summarizes the absolute mass of elements delivered into the hydrosphere by prograde metamorphism. Table S5 puts those results into context relative to the accreted composition and mass of Europa. Figures S7–S10 show the composition and source of the fluid extracted from the deep interior at different pressures with increasing temperature for all the *EM-CI* models and the *MC-Scale* model, equivalent to the *EM-CM* model shown in the main text.

The colored areas in the solvent plots (Figs. S7–S10) show regions in pressure-temperature space where that particular solvent (whether extracted or retained) is stable, and what the concentration of that solvent is, in units of moles of the specific solvent per kilogram of total solvents. The element concentration plots show the regions in pressure-temperature space where particular elements (existing in solvents and solutes) are extracted, in weight % of the total fluid extracted. In certain regions of pressure-temperature space, fluid (solvents and solutes) may be thermodynamically stable but may not end up being extracted, i.e., fluids are near their saturation point. For example, the plot for water as a solvent in Figure S9 (*EM-CI*, R/E = 5 wt. %) shows water to be present in a wider pressure and temperature space than the combined extracted H and extracted O plots do, or even the “mass % extracted” plot. This is because of the imposed retention-to-extraction rule: only free fluids that exceed 5 wt. % of the total assemblage are extracted. In other models where no fluid retention rules are imposed, minimal amounts of free fluids may exist at the end of a heating step, but be resorbed into the mineral phases when the model thermodynamically equilibrates the phase assemblage again.

Prograde metamorphic heating paths and how to read them: a walk-through using results

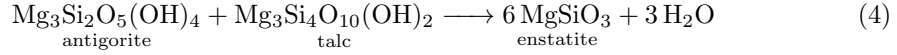
Here we relate further details about the deep interior’s mineralogical composition post-differentiation. The effect of prograde metamorphism and associated fluid extraction on the density of the interior is shown in Figure S11. Figures S12 and S13 show the mineralogy at 500 MPa and 3 GPa with increasing temperature respectively, for the *EM-CI* R/E = 0, *EM-CM* R/E = 0, and *MC-Scale* R/E = 0 models.

Compared to *MC-Scale*, fluids begin to be extracted at lower temperature (<400 K) in the *EM-CI* and *EM-CM* models. This comes about because the initial bulk *EM-CI* and *EM-CM* compositions contain excess water that cannot be fully accommodated by hydrous minerals. Most fluid in the thermal evolution of *MC-Scale* is extracted during the decomposition of carbonates (magnesite and dolomite) and phyllosilicates (antigorite and chlorite), leading to high masses of Al and Mg extracted together with water and CO₂ (Figs. S6 & S10). Additionally, large concentrations of Na (up to 10 wt. % of the fluid phase) and Si are exsolved at specific pressures and temperatures (Fig. S10) as Na-bearing clinopyroxene is transformed to Na-free clinopyroxene + olivine at 550 to 1050 K (Fig. S12 & S13).

We describe one of the heating paths here to walk the reader through the results, including the mineralogical changes, fluids generated and extracted, and the effects of fluid extraction on Europa’s density. We focus on the *EM-CM* R/E = 0 model as an example. Firstly, Figure 11g shows that the heating of the *EM-CM* body releases free fluids at all depths from the surface of Europa to the center, starting from 293 K. Higher amounts of fluids extracted denote points in P-T space where a volatile-bearing phase begins to transform to a volatile-free phase. The overall results of heating up to

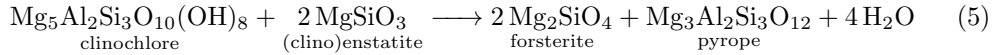
the Fe-SeS solidus (left to right on Fig. 11g) has the overall effect of increasing density as volatiles are released and extracted (Fig. 11i).

At the start (273.15 K) of an isobaric heating path at 500 MPa, the most abundant phase in the *EM-CM* body (Fig. 12b) is antigorite ($\text{Mg}_3\text{Si}_2\text{O}_5(\text{OH})_4$). Other stable volatile-bearing phases are calcite (CaCO_3), Mg-chlorite/clinochlore ($\text{Mg}_5\text{Al}_2\text{Si}_3\text{O}_{10}(\text{OH})_8$), greenalite ($(\text{Fe}^{\text{II}}, \text{Fe}^{\text{III}})_3\text{Si}_2\text{O}_5(\text{OH})_4$), dolomite ($\text{CaMg}(\text{CO}_3)_2$), goethite ($\text{FeO}(\text{OH})$), pyrite (FeS_2), and graphite (C). In addition, free fluid is thermodynamically stable, before fluid extraction is allowed to proceed. By ~ 340 K, goethite has transformed into spinel/magnetite (Fe_3O_4), releasing water; antigorite abundance increases at the expense of greenalite, and calcite is transformed into dolomite by ~ 400 K. At ~ 510 K, pyrite transforms to troilite, releasing sulfur ($\text{FeS}_2 \rightarrow \text{FeS} + \text{S}$), and talc forms at the expense of antigorite. At 780–840 K, antigorite, dolomite, magnesite (MgCO_3) and talc ($\text{Mg}_3\text{Si}_4\text{O}_{10}(\text{OH})_2$) destabilize completely in a series of reactions yielding clinochlore, clinoenstatite (MgSiO_3), forsterite (Mg_2SiO_4), H_2O and CO_2 :

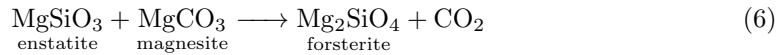


Finally, at 880–900 K, clinochlore reacts with clinoenstatite to yield forsterite, the amphibole pargasite ($\text{NaCa}_2(\text{Mg}_4\text{Al})(\text{Si}_6\text{Al}_2)\text{O}_{22}(\text{OH})_2$), and fluid. A small amount of water remains in pargasite, until it destabilizes to form nepheline ($\text{NaAlSi}_3\text{O}_8$) + clinopyroxene at ~ 1180 K.

The stable phase assemblage evolves differently at higher pressure. Taking the 3 GPa isobaric heating path as an example (Fig. 13b), the low temperature phases of the *EM-CM* body consist mainly of goethite, lizardite ($\text{Mg}_3\text{Si}_2\text{O}_5(\text{OH})_4$) and talc, and minor amounts of lawsonite ($\text{CaAl}_2\text{Si}_2\text{O}_7(\text{OH})_2\text{H}_2\text{O}$), clinoenstatite, pyrite and pumpellyite ($\text{Ca}_4\text{MgAl}_5\text{Si}_6\text{O}_{21}(\text{OH})_7$). The mineral hosts of carbon are diamond, and to a lesser extent, magnesite. At ~ 420 K, antigorite replaces lizardite, and chlorite replaces lawsonite. Goethite destabilizes at ~ 540 K, yielding spinel/magnetite and water. Pyrite transforms to troilite at ~ 700 K, releasing sulfur. Talc destabilizes completely at ~ 720 K to enstatite, and at ~ 780 – 800 K, antigorite, magnetite and diamond transform to graphite, magnesite and olivine, releasing water. At ~ 930 K, clinochlore dehydrates to garnet/pyrope:



Finally, a carbon-rich fluid is released at ~ 1150 K, when most magnesite destabilizes:



Effect of redox state on fluids extracted during prograde metamorphism

Contrary to preventing carbon from being released from the interior, the reduced conditions (*EM-CI*, *FMQ-2*, $R/E = 0$) prevent the stabilization of carbonates that would act as a carbon sink; carbon is released at low temperatures as CH_4 (Fig. S4). At high temperatures where graphite would be stable, no carbon remains to form it. Hence, reduced conditions actually promote the extraction of carbon during the early stages of Europa's differentiation. Figure S5 shows the composition of the ocean column, including precipitating minerals and exsolving gases. The total mass of CH_4 plus H_2 released from the interior and ocean (CO_2 is unstable) amounts to $\sim 10^{22}$ kg, equivalent to a 356 MPa $\text{CH}_4 + \text{H}_2$ volatile envelope. The liquid water ocean then amounts to $\sim 7.8 \times 10^{21}$ kg, about 0.16 wt. % of Europa's total mass. Thus, reduced conditions for the building material of Europa were unlikely because they yield a small ocean, inconsistent with observations.

Effect of fluid retention on extracted fluid compositions

Retaining exsolved fluids between temperature steps affects the pattern of volatile release and extraction by spreading the range at which fluids are extracted to higher temperatures at all pressures. However, lower total masses are extracted (Figs. S6 and S7–S9). For example, Ca + Cl are extracted at higher temperatures and lower pressures when fluid is retained ($R/E = 0.1$; Fig. S8) than when all exsolved fluids are extracted ($R/E = 0$; Fig. S7). The exsolution and extraction of sulfur are also shifted to higher temperatures if fluid is retained (Fig. S8). The effect is subtle for the $R/E = 0.1$ and clearer for the flat retention of 5 wt. % fluid (Figs. S8 and S8). Fluid retention significantly decreases the amount of dissolved Si (as aqueous SiO_2 , NaHSiO_3 and $\text{Mg}(\text{HSiO}_3)_2$); Na (as aqueous NaCl , NaHSiO_3 and Na^+), K (as aqueous KCl , KOH and K^+), Mg (as dissolved Mg^{2+} , MgCl_2 , $\text{Mg}(\text{HSiO}_3)_2$, MgOH^+ and MgCO_3), and Al (as AlO_2^-) (Fig. S4) since these are transferred from the retained fluid into rock-forming minerals in subsequent heating steps (see also Figs. S12–S13 and main text Equations 2–8). The opposite holds true for iron: retaining fluids causes Fe to increase in solution, where it is found as aqueous FeCl_2 , FeCl_3 , Fe^{2+} and FeCl^+ (Fig. S6, and S7–S8).

Chlorine and sulfur extracted into the hydrosphere

While the mass of chlorine extracted relative to the mass of chlorine in all bulk accreted compositions far exceeds the mass of sulfur extracted relative to the mass of initially accreted sulfur (mass chlorine extracted/mass chlorine accreted \gg mass sulfur extracted/mass sulfur accreted), in all models the absolute mass of sulfur in the extracted ocean exceeds the mass of extracted chlorine by an order of magnitude (Table S5).

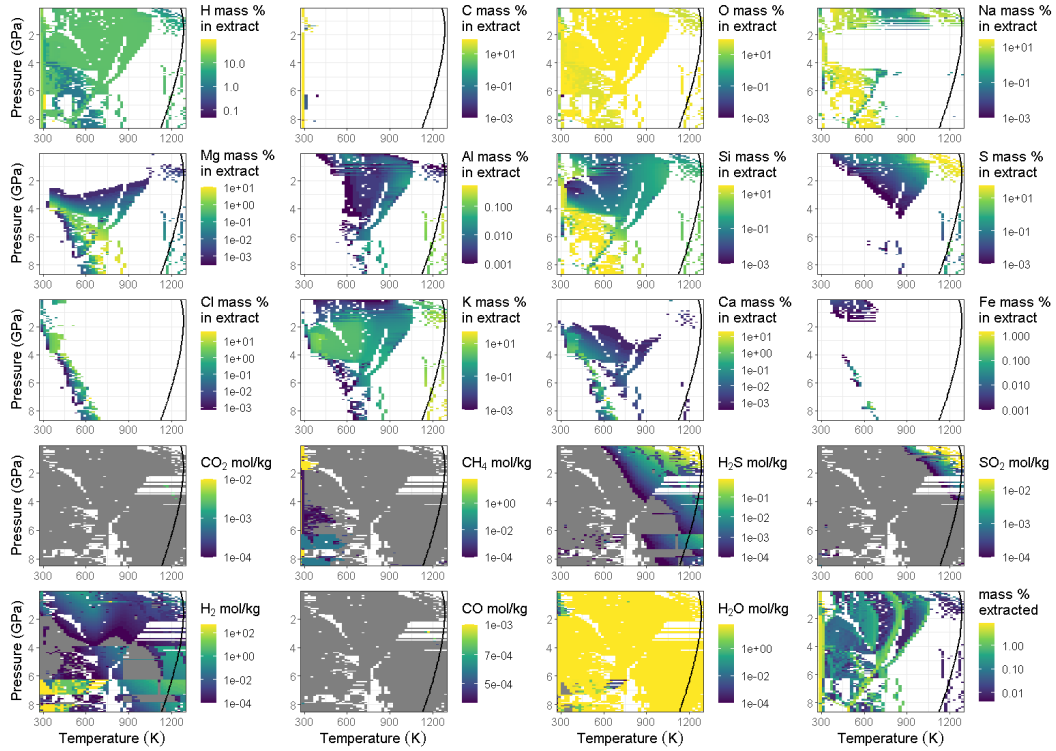
Figure S4: Extracted fluid composition for *EM-CI*, FMQ-2, R/E = 0

Figure 4. Composition of the fluid extracted from the deep interior at different pressures with increasing temperature for the *EM-CI*, *FMQ-2* R/E = 0 model. The solid curve shows the Fe-SeS eutectic temperature. Integrating up to the eutectic yields the total amounts exsolved from the deep interior. Blank areas signify that no fluids containing the specific element shown in the plot were extracted at those pressures and temperatures. Rows 1–3: elemental abundance of the extracted fluid (solvents and solutes). Rows 4–5: molecular solvent moles per kilogram of extracted fluid. Grey areas in the solvent plots signify that fluids were extracted at those pressures and temperatures, but did not contain the specific solvent shown in the plot. Bottom-right plot: total extracted mass.

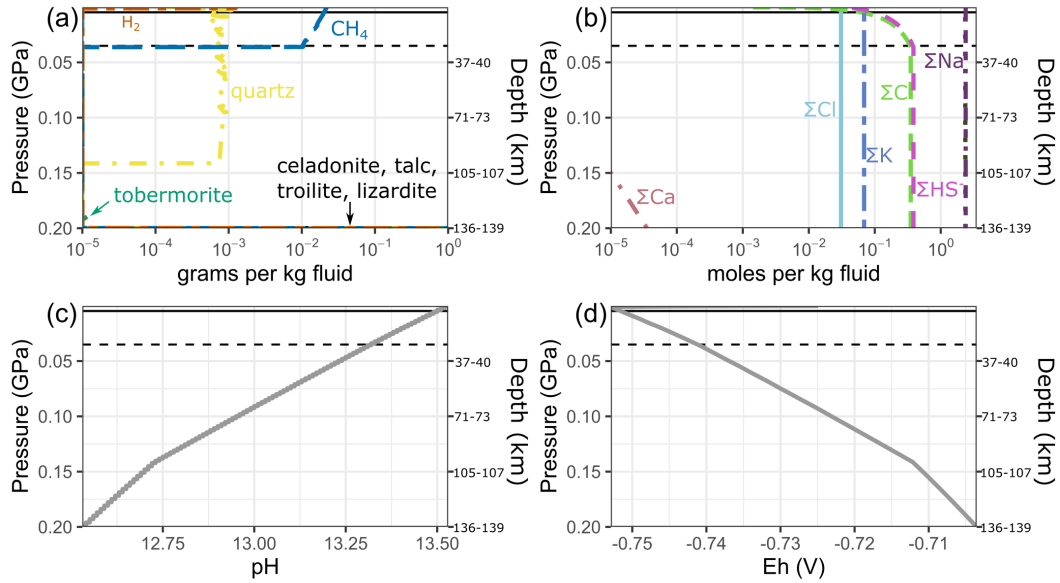
Figure S5: Ocean column composition for *EM-CI* FMQ-2, R/E = 0

Figure 5. Ocean column compositions from the seafloor to the surface, for *EM-CI*, *FMQ-2*, R/E = 0. Solid and horizontal lines show the pressure at the base of a current 5 km and 30 km ice shell respectively (see Main Text §3.3). a) Minerals precipitated and gases exsolved with decreasing depth in the water column. b) Total dissolved components in the water column. Dissolved components shown here are the sum of those particular components distributed among all species in solution. For example, component ΣC represents the sum of carbon in aqueous HCO_3^- , CH_4 , CO_2 , and organics, among other species. Concentrations $< 10^{-5}$ mol/kg not shown. c) pH, and d) redox potential of the ocean column.

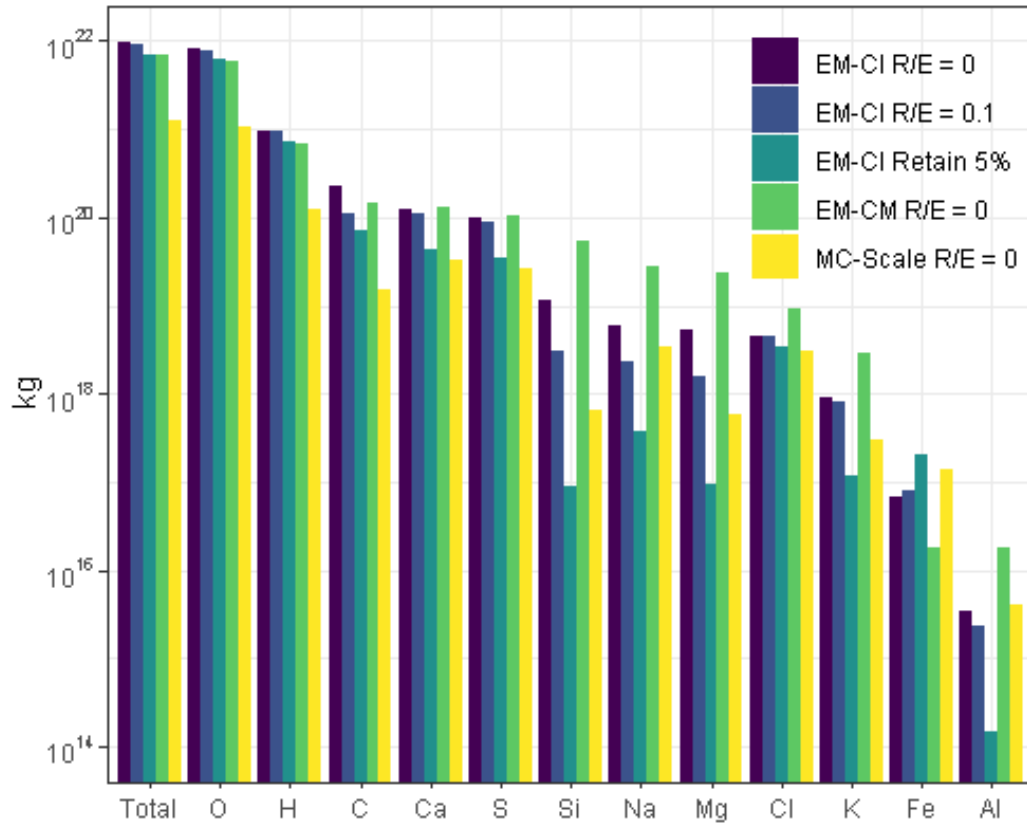
Figure S6: Absolute mass of elements extracted for all prograde metamorphism models**Figure 6.** Absolute mass of elements in the extracted hydrosphere reservoir during prograde metamorphism of the deep interior up to the stoichiometric Fe-SeS eutectic temperature at all depths.

Table S5: Mass and elemental composition of the extracted bulk fluid in context

Table 5. Mass and elemental composition of the extracted bulk fluid (unequilibrated with itself) for each model, in context with accreted elements and Europa’s mass. *EM-CI* = endmember CI initial bulk composition, *EM-CM* = endmember CM initial bulk composition *MC-Scale* = Monte Carlo scaled initial composition, R/E = retained-to-extracted fluid mass ratio, M_{Ext} = mass extracted, M_{Eur} = mass of Europa, M_{Acc} = bulk mass initially accreted for each element.

	<i>EM-CI</i>						<i>EM-CM</i>		<i>MC-Scale</i>	
	R/E=0		R/E=1:10		Extract all at >5 wt. %		R/E=0		R/E=0	
	$M_{\text{Ext}}/M_{\text{Eur}}$ %	$M_{\text{Ext}}/M_{\text{Acc}}$ %								
H	2.00	99.48	1.97	97.58	1.54	76.55	1.39	97.22	0.26	67.36
C	0.46	12.99	0.23	6.58	0.15	4.10	0.30	13.25	0.03	3.57
O	17.35	36.97	16.45	35.05	12.76	27.18	12.15	27.53	2.25	5.72
Na	0.01	2.45	<0.01	0.95	<0.01	0.15	0.06	14.21	0.01	2.01
Mg	0.01	0.11	<0.01	0.03	<0.01	<0.01	0.05	0.41	<0.01	0.01
Al	<0.01	<0.01	<0.01	<0.01	<0.01	<0.01	<0.01	<0.01	<0.01	<0.01
Si	0.02	0.22	0.01	0.06	<0.01	<0.01	0.11	0.87	<0.01	0.01
S	0.21	3.77	0.18	3.36	0.07	1.29	0.22	8.01	0.06	2.59
Cl	0.01	81.16	0.01	79.28	0.01	61.15	0.02	97.28	0.01	90.44
K	<0.01	3.32	<0.01	3.04	<0.01	0.43	0.01	16.17	<0.01	93.48
Ca	0.26	27.08	0.23	24.43	0.09	9.54	0.28	21.22	0.07	4.23
Fe	<0.01	<0.01	<0.01	<0.01	<0.01	<0.01	<0.01	<0.01	<0.01	<0.01
Total	20.34	20.34	19.09	19.09	14.61	14.61	14.58	14.58	2.69	2.69

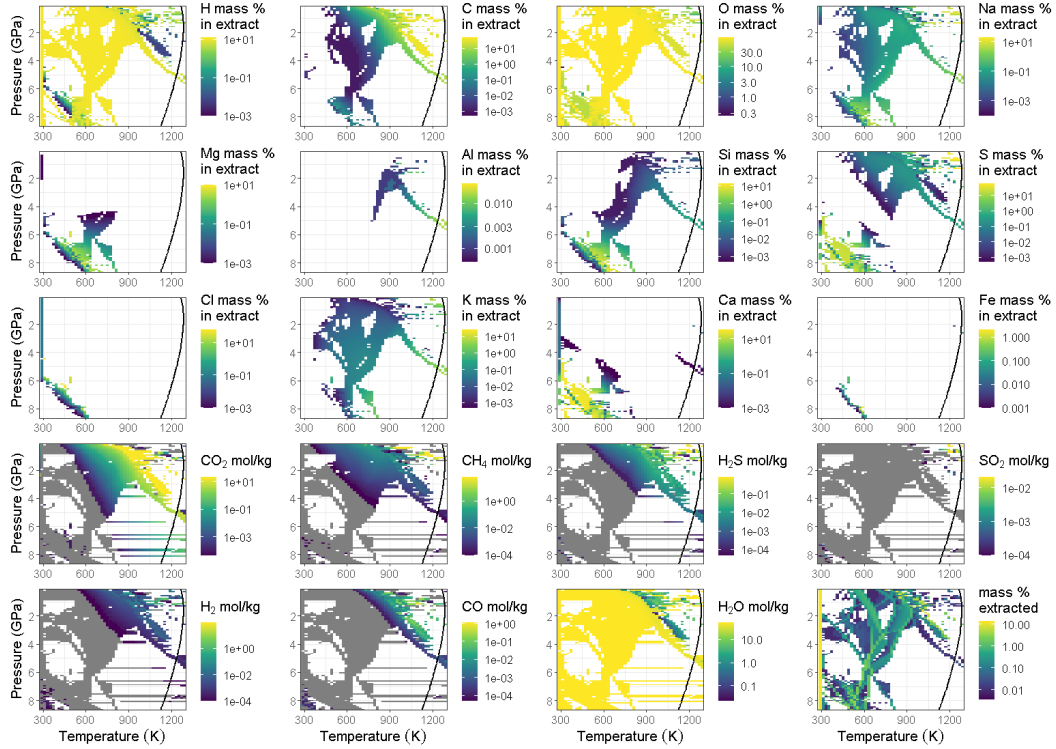
Figure S7: Extracted fluid composition for $EM-CI$ $R/E = 0$ 

Figure 7. Composition of the fluid extracted from the deep interior at different pressures with increasing temperature for the $EM-CI$ $R/E = 0$ model. The solid curve shows the Fe-SeS eutectic temperature. Integrating up to the eutectic yields the total amounts exsolved from the deep interior. Blank areas signify that no fluids containing the specific element shown in the plot were extracted at those pressures and temperatures. Rows 1–3: elemental abundance of the extracted fluid (solvents and solutes). Rows 4–5: molecular solvent moles per kilogram of extracted fluid. Grey areas in the solvent plots signify that fluids were extracted at those pressures and temperatures, but did not contain the specific solvent shown in the plot. Bottom-right plot: total extracted mass.

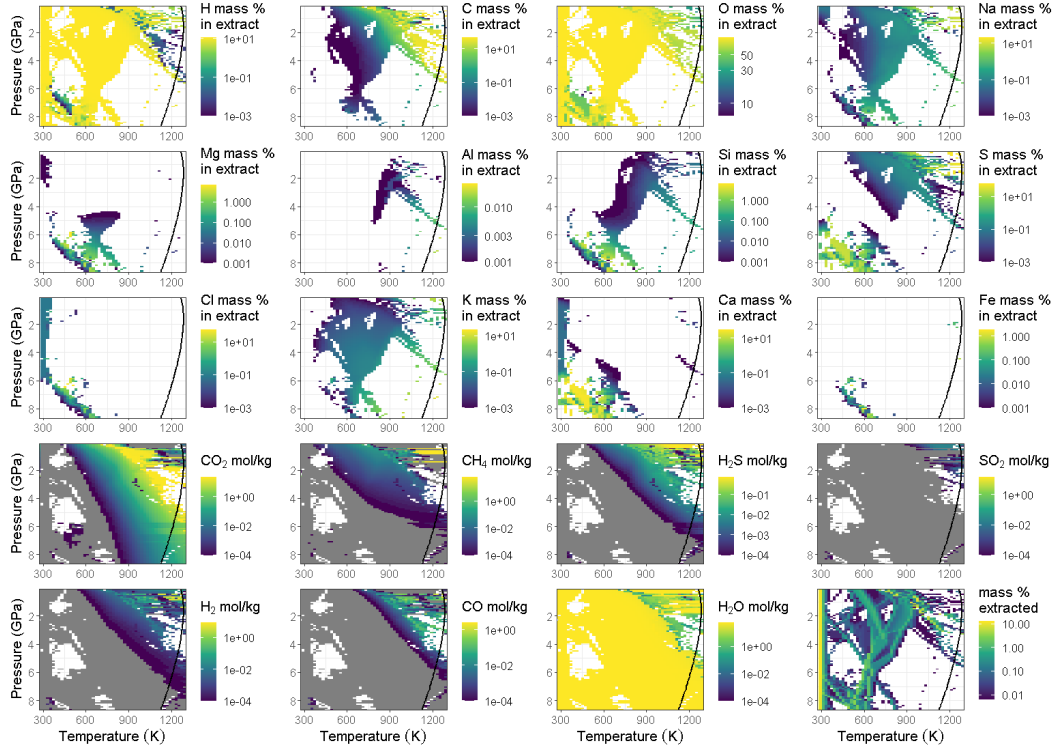
Figure S8: Extracted fluid composition for *EM-CI* $R/E = 0.1$ 

Figure 8. Composition of the fluid extracted from the deep interior at different pressures with increasing temperature for the *EM-CI* $R/E = 0.10$ model. The solid curve shows the Fe-SeS eutectic temperature. Integrating up to the eutectic yields the total amounts exsolved from the deep interior. Blank areas signify that no fluids containing the specific element shown in the plot were extracted at those pressures and temperatures. Rows 1–3: elemental abundance of the extracted fluid (solvents and solutes). Rows 4–5: molecular solvent moles per kilogram of extracted fluid. Grey areas in the solvent plots signify that fluids were extracted at those pressures and temperatures, but did not contain the specific solvent shown in the plot. Bottom-right plot: total extracted mass.

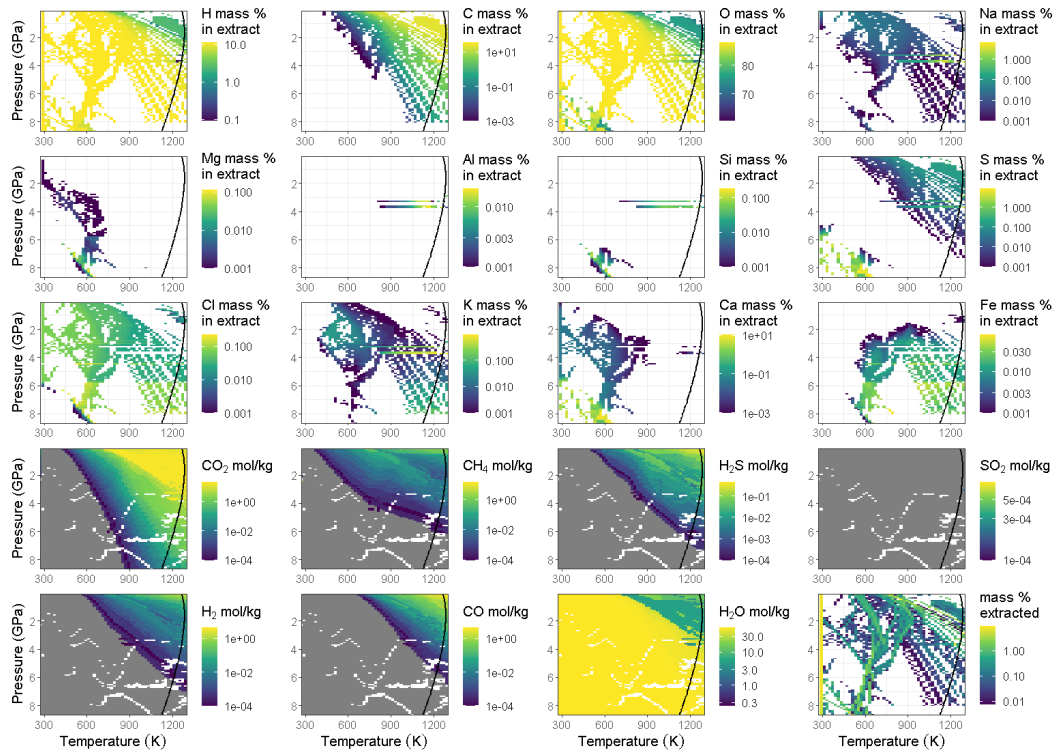
Figure S9: Extracted fluid composition for *EM-CI*, Retaining 5 wt.% fluid

Figure 9. Composition of the fluid extracted from the deep interior at different pressures with increasing temperature for the *EM-CI* Retain 5 wt. % model. The solid curve shows the Fe-SeS eutectic temperature. Integrating up to the eutectic yields the total amounts exsolved from the deep interior. Blank areas signify that no fluids containing the specific element shown in the plot were extracted at those pressures and temperatures. Rows 1–3: elemental abundance of the extracted fluid (solvents and solutes). Rows 4–5: molecular solvent moles per kilogram of extracted fluid. Grey areas in the solvent plots signify that fluids were extracted at those pressures and temperatures, but did not contain the specific solvent shown in the plot. Bottom-right plot: total extracted mass.

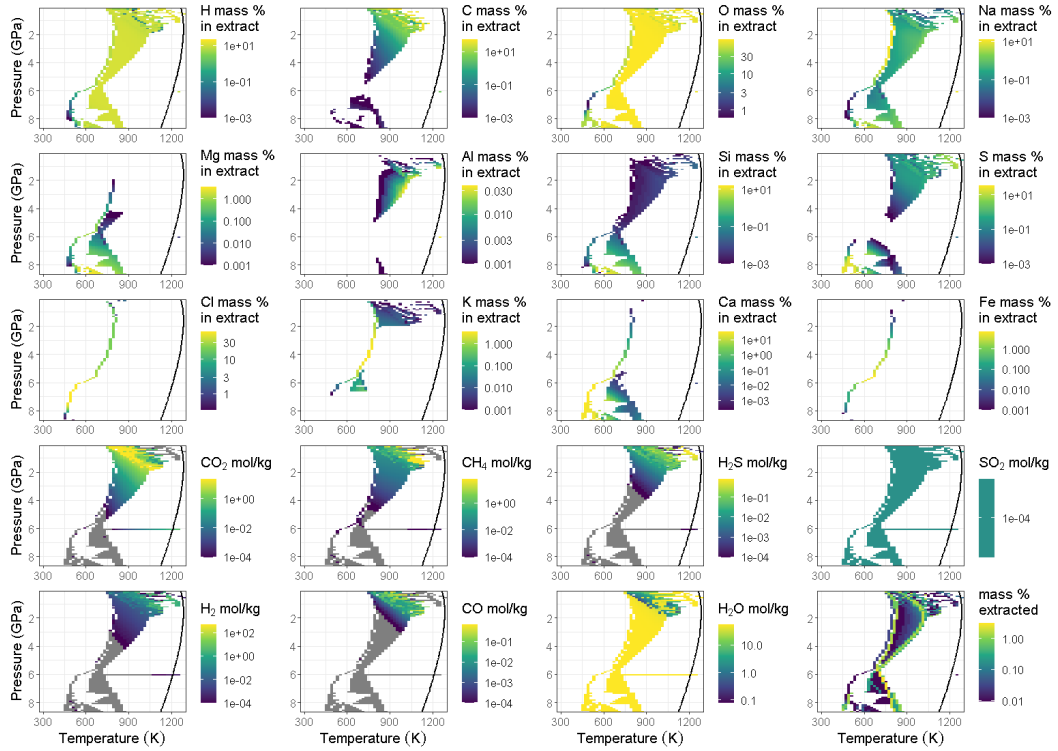
Figure S10: Extracted fluid composition for *MC-Scale* $R/E = 0$ 

Figure 10. Composition of the fluid extracted from the deep interior at different pressures with increasing temperature for the *MC-Scale* $R/E = 0$ model. The solid curve shows the Fe-SeS eutectic temperature. Integrating up to the eutectic yields the total amounts exsolved from the deep interior. Blank areas signify that no fluids containing the specific element shown in the plot were extracted at those pressures and temperatures. Rows 1–3: elemental abundance of the extracted fluid (solvents and solutes). Rows 4–5: molecular solvent moles per kilogram of extracted fluid. Grey areas in the solvent plots signify that fluids were extracted at those pressures and temperatures, but did not contain the specific solvent shown in the plot. Bottom-right plot: total extracted mass.

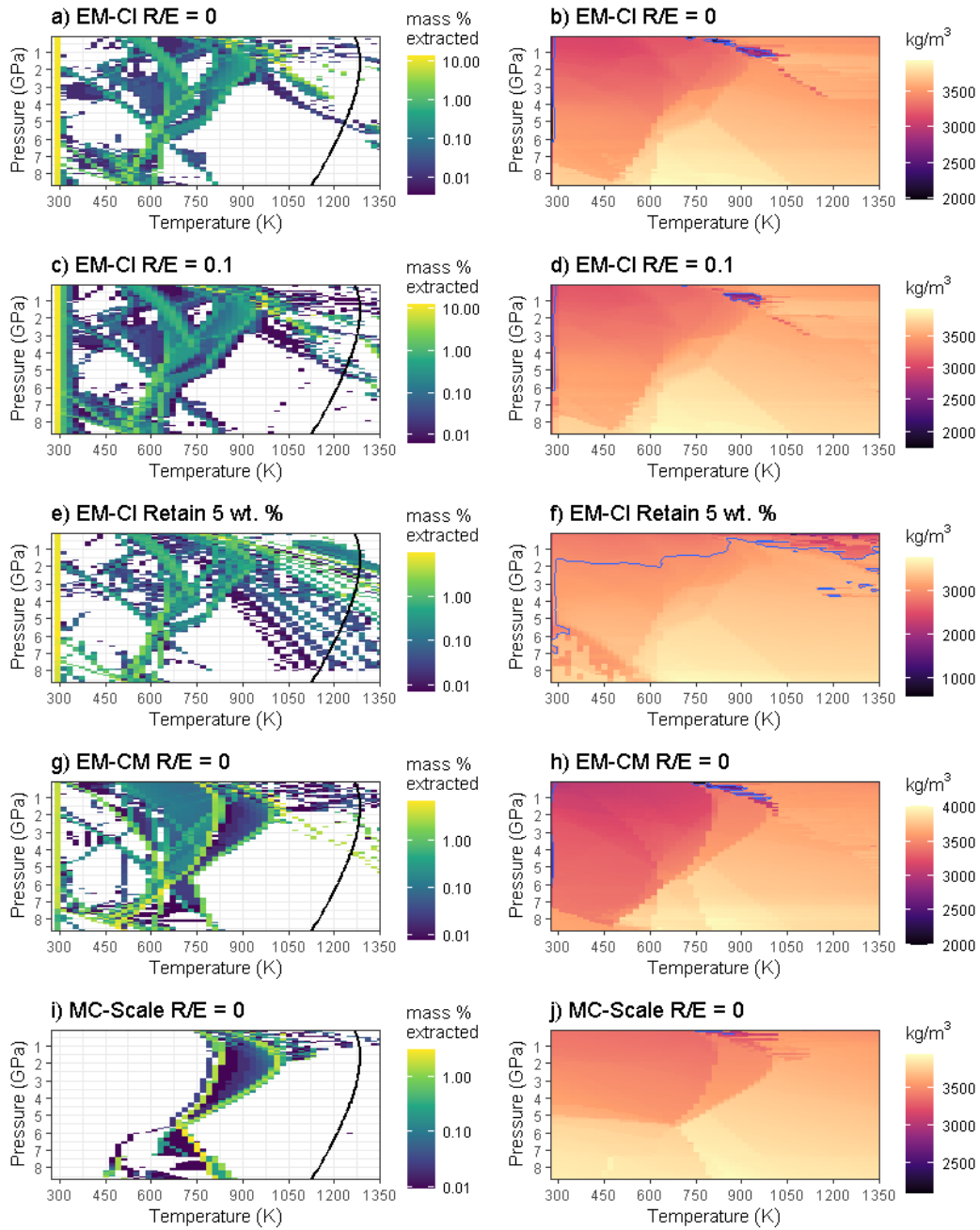
Figure S11: Effect of fluid extraction on the deep interior's density

Figure 11. Mass % of fluid transferred into the ocean reservoir during prograde metamorphism of the undifferentiated bulk composition at all depths (left column) and resulting density of the deep interior (right column). Panels in the left column are reproduced from Main Text Figure 2 and Figures S7–S10. The solid black curve represents the Fe–Se eutectic temperature bracketing the minimum temperature to segregate a Fe \pm S core. The blue contour line is an isopycnic line of constant density $\rho = 3000 \text{ kg m}^{-3}$.

Figure S12: Changing mineralogy at 0.5 GPa in prograde metamorphism/fluid extraction

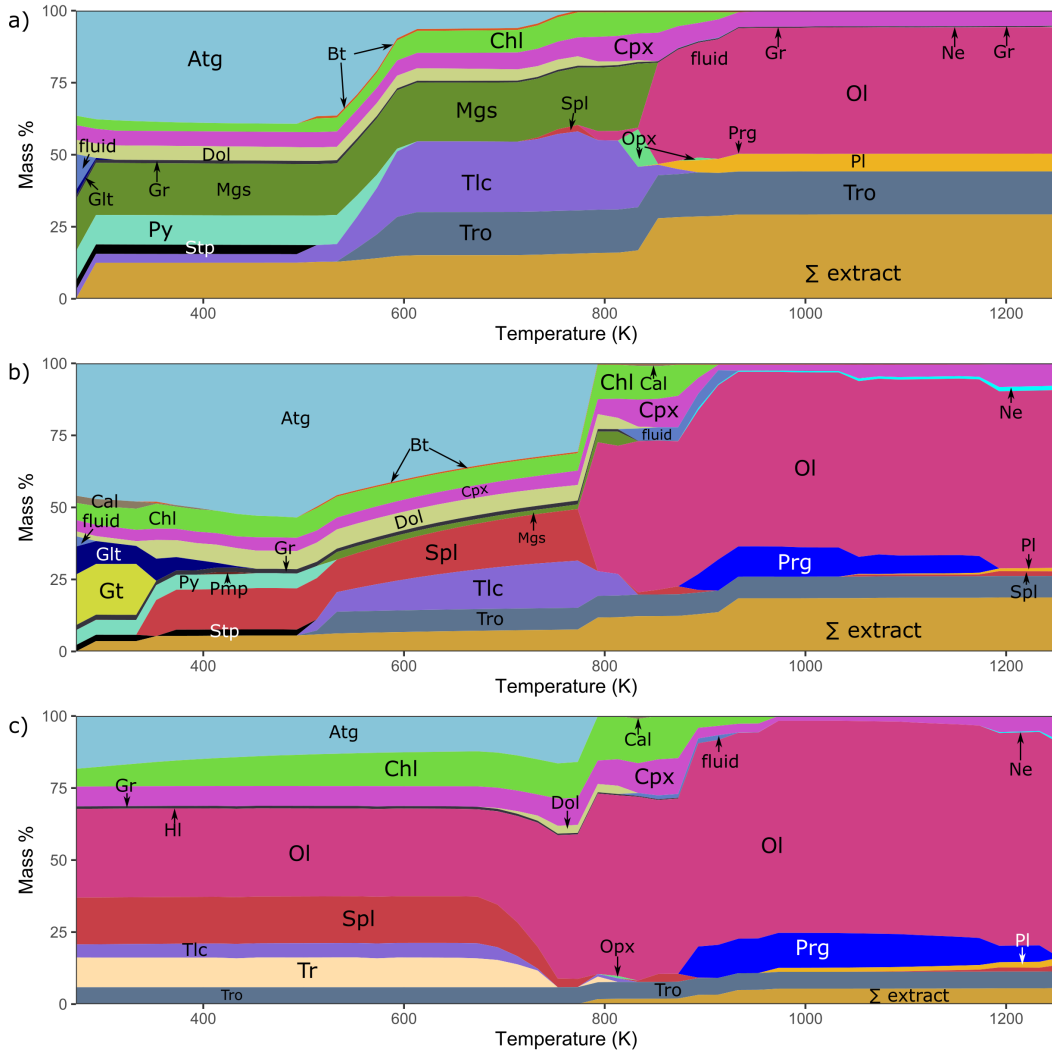


Figure 12. Phase changes and fluid extracted at 500 MPa for a) *EM-CI* $R/E = 0$, b) *EM-CM* $R/E = 0$, and c) *MC-Scale* $R/E = 0$. Phase abbreviations are: Atg = antigorite, Bt = biotite, Chl = chlorite, Cpx = clinopyroxene, Dia = diamond, Dol = dolomite, Glt = greenalite, Gr = graphite, Grt = garnet, Gt = goethite, Hl = halite, Lws = lawsonite, Lz = lizardite, Mgs = magnesite, Ne = nepheline, Ol = olivine, Opx = orthopyroxene, Pl = plagioclase, Pmp = pumpellyite, Prg = pargasite, Py = pyrite, Spl = spinel, Stp = stilpnomelane, Tlc = talc, Tro = troilite. Two immiscible clinopyroxene phases have been binned together. "Σ Extract" is the cumulative extracted fluid with increasing temperature. Free volatiles, i.e., "fluid" can appear in the heating path plots because the phases shown are the result of the sequence: temperature increase + equilibration \rightarrow fluid extraction \rightarrow equilibration, i.e., thermodynamic equilibration of the phase assemblage after extraction of free fluid may release fluids again.

Figure S13: Changing mineralogy at 3 GPa in prograde metamorphism/fluid extraction

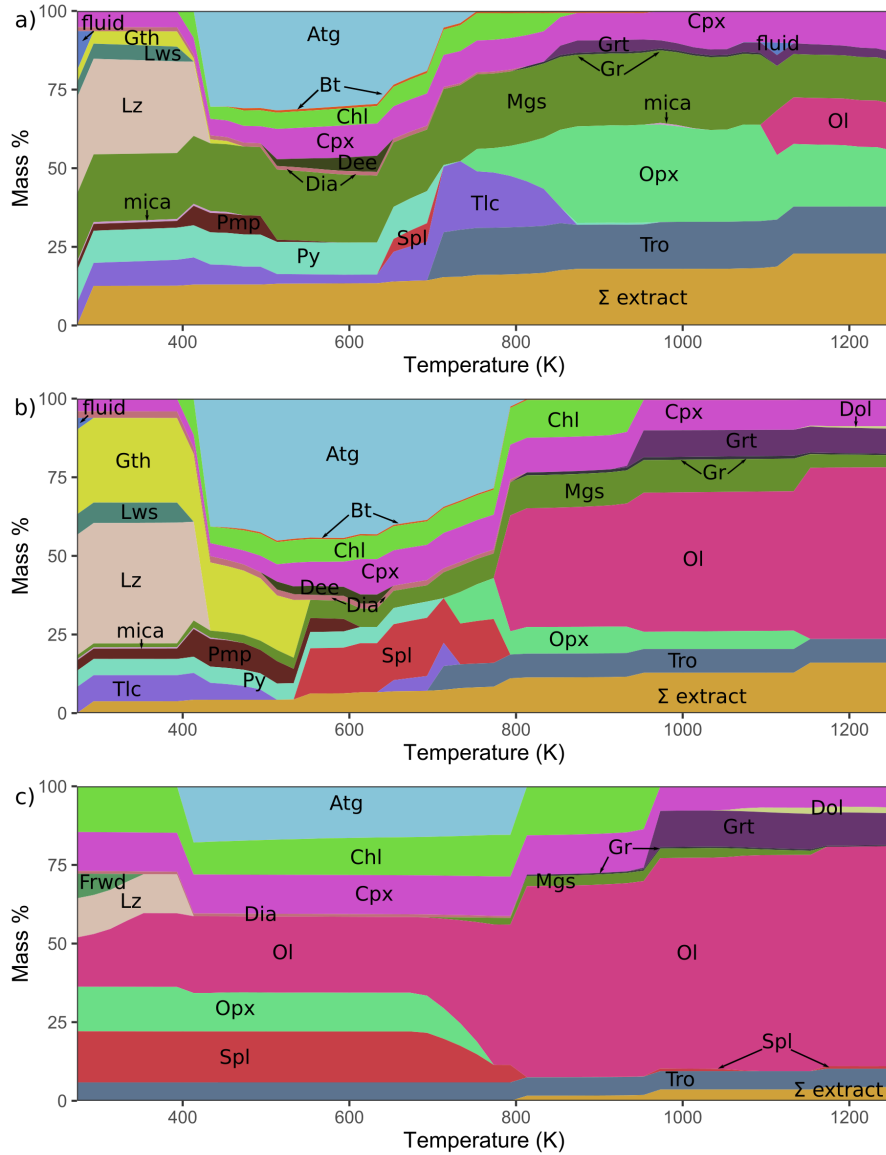


Figure 13. Phase changes and fluid extracted at 3 GPa for a) *EM-CI* $R/E = 0$, b) *EM-CM* $R/E = 0$, and c) *MC-Scale* $R/E = 0$. Phase abbreviations are: Atg = antigorite, Bt = biotite, Chl = chlorite, Cpx = clinopyroxene, Dee = deerite, Dia = diamond, Dol = dolomite, Grt = garnet, Gth = goethite, Gr = graphite, Hal = halite, Lws = lawsonite, Lz = lizardite, Mgs = magnesite, Ol = olivine, Opx = orthopyroxene, Pmp = pumpellyite, Py = pyrite, Spl = spinel, Tlc = talc, Tro = troilite. Two immiscible clinopyroxene phases have been binned together. "Mica" comprises a solid solution of celadonite, ferrocaldonite, muscovite and pargasite. "Σ Extract" is the cumulative extracted fluid with increasing temperature. Free volatiles, i.e., "fluid" can appear in the heating path plots because the phases shown are the result of the sequence: temperature increase + equilibration \rightarrow fluid extraction \rightarrow equilibration, i.e. thermodynamic equilibration of the phase assemblage after extraction of free fluid may release fluids again.

Text S6: Mechanisms and limits of volatile sequestration and loss to space

The volatile extraction and outgassing considered in this work can be summarized in two consecutive steps: 1) formation of a condensed liquid ocean by the volatiles released from Europa's bulk accreted body on the pathway towards the formation of a Fe-core, and 2) outgassing from the liquid ocean as gases exceed their solubility limit. The outgassing of ~ 27 MPa CO_2 (Main Text Table 1) is an upper limit, based on the assumption that Europa was formed by CI carbonaceous chondrites, which are the most volatile-rich chondrites. Such a scenario leads to an excessively massive hydrosphere (17.8 wt. %), inconsistent with Europa's present-day hydrosphere. We note that for larger, less volatile-rich bodies, the amounts of outgassed primordial volatiles are on the same order of that calculated in this work: 5–25 MPa of H_2O and in excess of 1–5.5 MPa of CO_2 are calculated to have been lost from Mars in the first 12 Myr after accretion (Erkaev et al., 2014; Odert et al., 2018). The mantles and crusts of Mars and other terrestrial bodies would be substantially devolatilized after this primary catastrophic outgassing (Lammer et al., 2013). Secondary, long-term outgassing, is of a significantly lower magnitude (e.g., compare primary outgassing estimates from Erkaev et al. (2014) and Odert et al. (2018), with secondary, nominally volcanic, outgassing in Craddock and Greeley (2009)), and not the focus of this work. We also note that massive primordial atmospheres have been predicted for Triton (~ 160 MPa pCO_2 Lunine & Nolan, 1992), Ganymede and Callisto (Kuramoto & Matsui, 1994), which have exceedingly thin exospheres at present. In addition, for the CI chondrite and CM chondrite bulk compositions, we predict that the mass of water devolatilized from the interior exceeds Europa's present-day hydrosphere (Figure S6 and Table S5), signifying that the difference between the present hydrosphere mass and the amount exsolved from the interior (1.5×10^{21} – 5.5×10^{21} kg H_2O , equivalent to 62–209 MPa pH_2O) would have to have been lost to space.

Sequestration by clathrates

An alternative to loss of CO_2 by the formation of an atmosphere and ultimate loss to space, is the formation of clathrate hydrates. Calculating how a potential clathrate layer at Europa's seafloor affects the thermal properties and lifetime of the ocean is beyond the scope of this work, primarily because it would require a geodynamic simulation accounting for complex feedback (e.g. Kalousová & Sotin, 2020). Nevertheless, we provide further context and summarize what the fate of clathrates would be below, based on known and approximated thermodynamic properties. Whether CO_2 clathrates are stable in Europa's ocean depends on the pressure and temperature, assuming sufficient CO_2 feedstock is present. The thermodynamically favored CO_2 clathrate structure for Europa's ocean would be sI. For large amounts of CO_2 produced here, we calculate sI clathrates with a $\text{CO}_2/\text{H}_2\text{O}$ molar ratio of 0.159 at 273.15 K and equilibrium pressure (1.243 MPa), using the formulation from Sloan and Koh (2008, p. 268). We calculate a clathrate density of 1106 kg/m^3 from:

$$\rho = \frac{N_w M_w + (N_{Lg} M_g \theta_L) + (N_{Sg} M_g \theta_S)}{N_A V_{sI}} \times 1000 \quad (7)$$

where N_w (= 46) is the number of water molecules per sI crystal cell, M_w is the molecular mass of water, N_{Lg} (= 6) and N_{Sg} (= 2) are the number of guest species molecules in the large and small cavities of sI clathrates respectively, M_g is the molecular mass of the clathrate guest species (44 g/mol for CO_2), θ_L (= 0.9808) and θ_S (= 0.7248) are the occupancy fractions for the large and small cavities occupied by the guest species, N_A is Avogadro's number and V_{sI} is the volume of sI clathrate crystal cells (12×10^{-8} cm^3). Equilibrium pressures for ocean temperatures $\gtrsim 277.2$ K are

higher than 200 MPa, meaning that CO₂ clathrates would not be stable in Europa’s ocean.

We assume that the clathrates sink if their density exceeds the density of the liquid ocean. Using the Pitzer and Sterner (1994) equation of state for H₂O-CO₂ fluids implemented in *Perple_X*, we calculate that the density of the exsolved ocean composition is comparable to that of seawater, never exceeding the density of the sI CO₂ clathrates (Fig. S14), and therefore the clathrates will tend to sink. This would result in total clathrate thicknesses of 3.4–77 km mantling Europa’s seafloor, using the outgassing calculation of 2.65×10^{19} – 6.40×10^{20} kg CO₂ (Main Text Table 1) and a seafloor at 140 km beneath the surface (Vance et al., 2018). Previous work by Bouquet, Mousis, Glein, Danger, and Waite (2019) and Prieto-Ballesteros et al. (2005) concur that CO₂ clathrates would sink to the bottom of Europa’s seafloor if the composition of Europa’s ocean was that of pure or low salinity water. However, equations of state up to 200 MPa adequately describing the density of mixed COHS-fluids including Ca-Na-Mg-K-CO₃-SO₄-Cl salts are currently lacking, and if Europa’s ocean became progressively saltier in time, perhaps as a result of progressive freezing of the ice shell, the density of the ocean would exceed the density of the clathrates, and so any clathrates present in the ocean would tend to float towards the surface (Fig. S14). Finally, calculations have shown that magmatism at Europa’s seafloor is likely to have occurred over geologic time (Běhounková et al., 2021), so clathrates are unlikely to remain stable at Europa’s seafloor for 4.5 Gyr. However: 1) the predicted spatial distribution of dissipation favors magmatism at the poles (Běhounková et al., 2021), so clathrates may remain stable nearer to the equator, and 2) effusive volcanic events may provide silicate rocks at the seafloor that would efficiently react with and sequester aqueous CO₂.

Nevertheless, assuming that the ocean temperature has remained low enough to stabilize clathrates, and that the viscosity of high pressure ice on Ganymede and Titan’s seafloors (Choblet et al., 2017; Kalousová & Sotin, 2020) applies to a CO₂ clathrate blanket on Europa’s seafloor, then long-term stability of the liquid ocean is still predicted for seafloor mantling layers < 80 km thick and reasonable heat fluxes (> 6 mW/m²) from the silicate interior into the bottom of the ice or clathrate layer (Kalousová & Sotin, 2020). Melt and heat transport from the bottom of the clathrate layer to the ocean would occur either through hot plume conduits or solid state convection (Choblet et al., 2017; Kalousová & Sotin, 2020). If efficient depletion of CO₂ took place through carbonate formation or clathration, Europa’s ocean, like Earth’s atmosphere, could have a high N/C ratio. On the other hand, if CO₂ was not substantially lost from the hydrosphere after outgassing, the N/C ratio of the ocean should be low, reflecting periodic resupply from destabilized clathrates, or a primordial ocean composition.

Loss to space

Independent measurements have tentatively detected plumes at Europa (Jia et al., 2018; Roth et al., 2014; Sparks et al., 2016), which provide a plausible process for volatile loss from the ocean. We estimate the mass ejection rate of a representative conic plume as:

$$\frac{m}{dt} = \frac{\rho \pi r^2 v^3}{3} \quad (8)$$

assuming a representative mass $m = 10^6$ kg, radius $r = 135$ km and ejection velocity $v = 100$ – 1000 m s⁻¹ (Roth et al., 2014; Sparks et al., 2016). Plume density ρ is obtained from:

$$\rho = \frac{m}{V} \quad (9)$$

where plume volume V is approximated as a cone:

$$V = \frac{\pi r^2 h}{3} \quad (10)$$

with height $h = 200$ km (Sparks et al., 2016). We estimate an ejection rate of 5×10^2 – 5×10^3 kg/s, and 7.2×10^{19} – 7.2×10^{20} kg H₂O lost over 4.56 Gyr, or about 1.4–24 % Europa’s present ocean mass over the lifetime of the solar system. These represent upper limits since the estimation assumes constant plume activity, and in addition, most of the water would return to the surface given ejection velocities lower than the escape velocity of ~ 2.03 km/s.

Gases exceeding their solubility limit in Europa’s warmer primordial ocean, however, are much more likely to escape Europa’s gravitational pull. Placing precise constraints on the rate of atmospheric escape is not within the scope of this work, but we mention a number of possible mechanisms prevalent in the Jovian system to motivate further study. While infrared spectroscopy has revealed likely CO₂ ice and possible carbonate signatures presently at Europa’s surface (Hansen & McCord, 2008; McCord et al., 1999, 1998), these do not appear to be significant compared to the massive early outgassing of CO₂ calculated in this work. Small bodies may lose much of their heavy atmospheric species through early runaway greenhouse-type episodes, i.e., along with the efficient hydrodynamic escape of H and H₂ (e.g. Lammer et al., 2010). The volatile mixture exsolved from the ocean is CO₂-rich (CO₂/(H₂O + CO₂) = 0.997–0.999; Main Text Table 1), which would limit diffusive thermal escape of hydrogen to space by the infrared cooling effect of CO₂. Alternatively, sputtering caused by incident extreme ultraviolet of the young sun and charged particle flux could directly eject atmospheric species. Additionally, neutral molecules can be ionized, picked up by Jupiter’s magnetic field and accelerated away by plasma flow, or back towards the primordial atmosphere, where sputtering resumes. This may result in net dissociation of CO₂, decreasing infrared cooling and leading to a large expansion of the thermosphere, further accelerating loss (e.g. Tian et al., 2009). Constraining the long term impact history of Europa is hampered by the young surface age, but impacts that blew away the early atmosphere may also be possible.

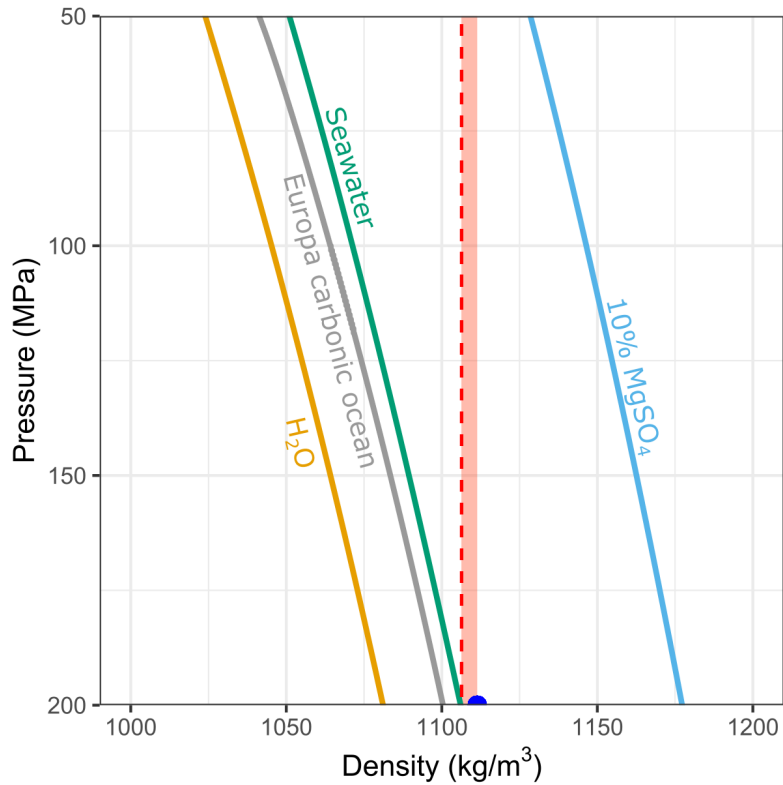
Figure S14: Density of CO₂ clathrates in Europa's ocean

Figure 14. Density of Europa's exsolved carbonic ocean (from the *EM-CI* R/E = 0 model), compared to pure water, seawater and a 10 wt. % MgSO₄ ocean, from Vance et al. (2018). The red dashed line shows the density of CO₂ clathrates in Europa's carbonic ocean at 273.15 K, from the equilibrium pressure to seafloor pressures. These clathrates would sink in a carbonic ocean but float in a 10 wt. % MgSO₄ ocean. The blue circle shows the equilibrium pressure and density of CO₂ clathrates at 277.23 K. At > 277.23 K, CO₂ clathrates would not be stable in Europa's ocean. The red shaded area shows the range of CO₂ clathrate densities stable in Europa's ocean.

Text S7: Compensating for insufficient volatiles extracted from *MC-Scale* with comets

Prograde metamorphism of the *MC-Scale* model yields an extracted hydrosphere less massive than Europa’s present-day hydrosphere (Figs. S6 and S10, and Table S5), so we performed a chemical equilibrium model with CHIM-XPT to compensate for the missing ocean mass after metamorphism, by adding cometary material (Table S2). *MC-Scale* produced a 2.63 mass % hydrosphere, so we added 7.31 mass % cometary material to produce a 10 mass % hydrosphere. The resulting ocean composition is reduced, basic, and carbon, silicon, sodium and sulfide-rich (Fig. S15). Graphite, greenalite, pyrite and talc are only stable at the seafloor, while quartz saturates and precipitates throughout the ocean column. Calcite saturates at the bottom, the calcium silicate hydrate tobermorite ($\text{Ca}_{0.833}\text{SiO}_2(\text{OH})_{1.667}(\text{H}_2\text{O})_{0.5}$) saturates in the middle of the ocean, and methane saturates and is exsolved near the top. The mass of precipitates would form a 38.2 km layer at the seafloor while the total mass of exsolved CH_4 would yield a ~ 8 MPa envelope.

Figure S15: Ocean column composition for *MC-Scale* plus cometary material

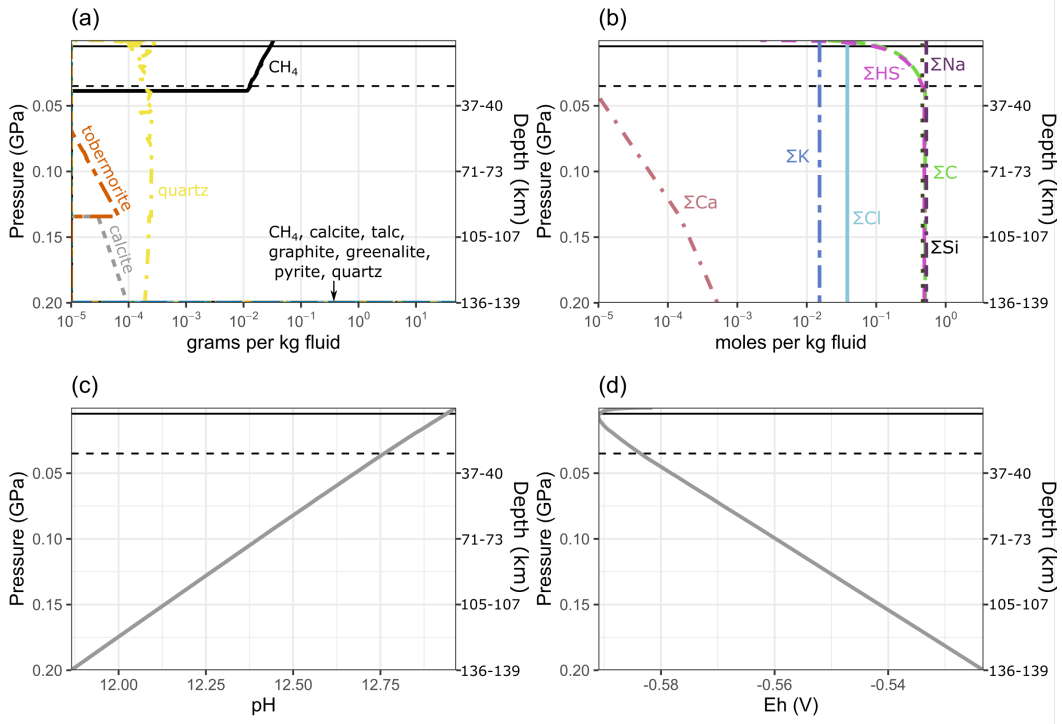


Figure 15. Ocean column compositions from the seafloor to the surface, for *MC-Scale*, $R/E = 0$, with added cometary material. Solid and horizontal lines show the pressure at the base of a current 5 km and 30 km ice shell respectively (see Main Text §3.3). a) Minerals precipitated and gases exsolved with decreasing depth in the water column. b) Total dissolved components in the water column. Dissolved components shown here are the sum of those particular components distributed among all species in solution. For example, component ΣC represents the sum of carbon in aqueous HCO_3^- , CH_4 , CO_2 , and organics, among other species. Concentrations $< 10^{-5}$ mol/kg not shown. c) pH, and d) redox potential of the ocean column.

Table S6: Adjusted mass of Europa’s hydrosphere for *MC-Scale* plus cometary material

Table 6. Adjusted mass of Europa’s hydrosphere after accounting for sediments predicted to precipitate on the seafloor and mass of gases exsolved at low pressure in the ocean column, for the *MC-Scale* model with cometary material added to form a 10 mass % hydrosphere. ”Thickness” = globally averaged thickness of the precipitate layer at Europa’s seafloor, for a hydrosphere depth of 140 km (see Main Text §3.3). ”Adjusted hydrosphere mass” = 10 mass % hydrosphere minus the mass of minerals precipitated and gases exsolved from the water column. M_{Eur} = mass of Europa.

Mineral precipitates	Concentration g/kg fluid	Mass kg
calcite	38.70	1.86×10^{20}
graphite	56.27	2.70×10^{20}
greenalite	129.35	6.24×10^{20}
pyrite	72.31	3.47×10^{20}
quartz	220.73	1.06×10^{21}
talc	79.33	3.81×10^{20}
tobermorite	0.02	1.10×10^{17}
	Mean density kg/m ³	Thickness km
Total precipitates	2881 ^a	38.20 ^a
Gases exsolved	Concentration g/kg fluid	Mass kg
CH ₄ gas	38.84	1.86×10^{20}
	Mass kg	$A_{\text{Hyd}}/M_{\text{Eur}}$ Mass %
Adjusted hydrosphere (A_{Hyd})	4.61×10^{21}	9.61

^aDoes not include tobermorite precipitated, since it is not thermodynamically stable at the seafloor (see Fig. S15).

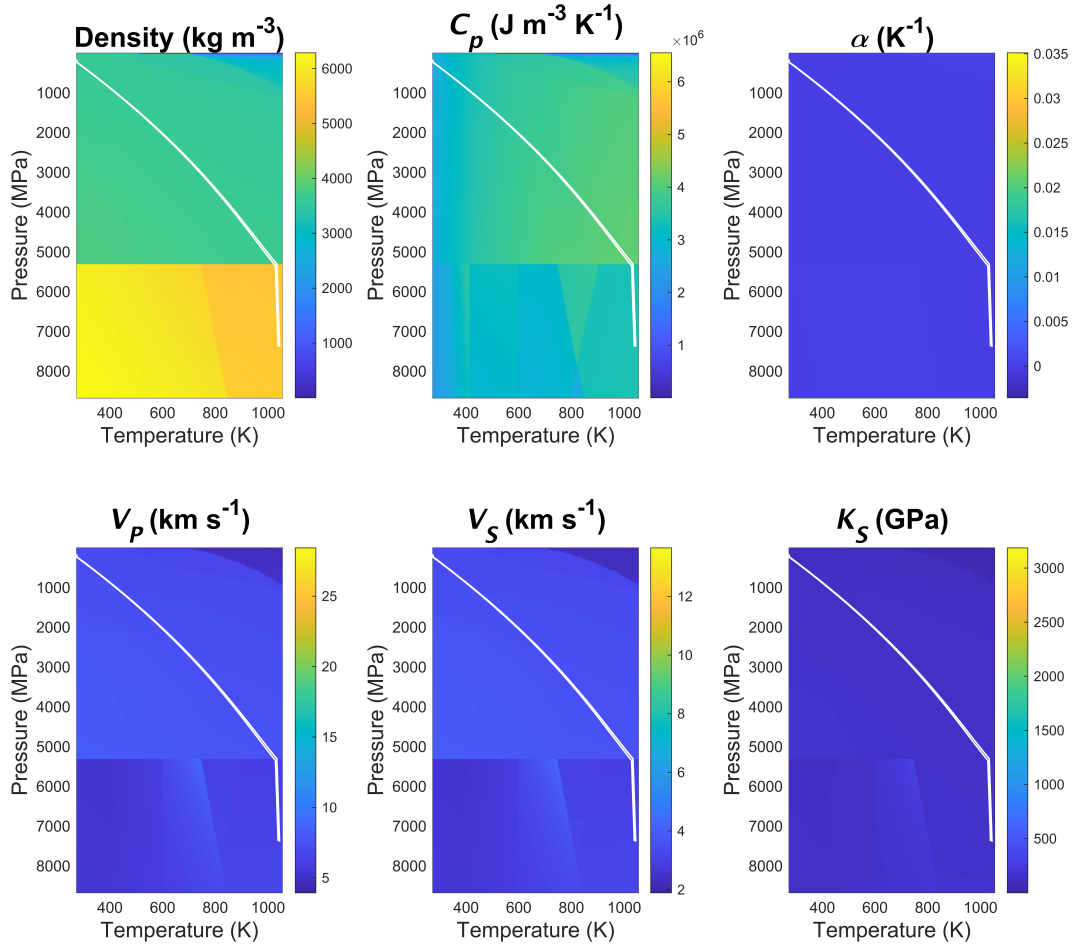
Figure S16: Final radial properties of Europa

Figure 16. Radial properties and structure of the interior of Europa for an ocean with the properties of seawater. White curves are pressure-temperature profiles corresponding to a Europa with a ~ 5 km surface ice Ih shell (slightly warmer, i.e., steeper profile) and a ~ 30 km surface ice Ih shell (slightly cooler).

References

- Airieau, S., Farquhar, J., Thiemens, M., Leshin, L., Bao, H., & Young, E. (2005, August). Planetesimal sulfate and aqueous alteration in CM and CI carbonaceous chondrites. *Geochimica et Cosmochimica Acta*, 69(16), 4167–4172. Retrieved from <http://www.sciencedirect.com/science/article/pii/S0016703705002437> doi: 10.1016/j.gca.2005.01.029
- Anderson, J. D., Schubert, G., Jacobson, R. A., Lau, E. L., Moore, W. B., & Sjogren, W. L. (1998). Europa's differentiated internal structure: Inferences from four Galileo encounters. *Science*, 281(5385), 2019–2022. Retrieved from <http://science.sciencemag.org/content/281/5385/2019> doi: 10.1126/science.281.5385.2019
- Badro, J., Brodholt, J. P., Piet, H., Siebert, J., & Ryerson, F. J. (2015). Core formation and core composition from coupled geochemical and geophysical constraints. *Proceedings of the National Academy of Sciences of the United States of America*, 112(40), 12310–12314. Retrieved from <http://www.ncbi.nlm.nih.gov/pmc/articles/PMC4603515/> doi: 10.1073/pnas.1505672112
- Bardyn, A., Baklouti, D., Cottin, H., Fray, N., Briois, C., Paquette, J., ... Hilchenbach, M. (2017, July). Carbon-rich dust in comet 67P/Churyumov-Gerasimenko measured by COSIMA/Rosetta. *Monthly Notices of the Royal Astronomical Society*, 469(Suppl.2), S712–S722. Retrieved 2020-06-25, from https://academic.oup.com/mnras/article/469/Suppl_2/S712/4670835 doi: 10.1093/mnras/stx2640
- Bjerga, A. (2014). *Evolution of talc- and carbonate-bearing alterations in ultramafic rocks on Leka (central Norway)* (Doctoral dissertation, The University of Bergen, Bergen). Retrieved 2021-04-04, from <https://hdl.handle.net/1956/7893> (Accepted: 2014-04-01T07:58:09Z Publisher: The University of Bergen)
- Bjerga, A., Konopásek, J., & Pedersen, R. (2015, June). Talc-carbonate alteration of ultramafic rocks within the Leka Ophiolite Complex, Central Norway. *Lithos*, 227, 21–36. Retrieved from <https://www.sciencedirect.com/science/article/pii/S0024493715001085> doi: 10.1016/j.lithos.2015.03.016
- Bland, P. A., Cressey, G., & Menzies, O. N. (2004, January). Modal mineralogy of carbonaceous chondrites by X-ray diffraction and Mössbauer spectroscopy. *Meteoritics & Planetary Science*, 39(1), 3–16. Retrieved 2020-03-04, from <https://doi.org/10.1111/j.1945-5100.2004.tb00046.x> (Publisher: John Wiley & Sons, Ltd) doi: 10.1111/j.1945-5100.2004.tb00046.x
- Bouquet, A., Mousis, O., Glein, C. R., Danger, G., & Waite, J. H. (2019, oct). The role of clathrate formation in Europa's ocean composition. *The Astrophysical Journal*, 885(1), 14. Retrieved from <https://doi.org/10.3847/2F1538-4357/2Fab40b0> doi: 10.3847/1538-4357/ab40b0
- Brearley, A. J. (2006, January). The Action of Water. In *Meteorites and the Early Solar System II* (p. 584). Retrieved from <https://ui.adsabs.harvard.edu/abs/2006mess.book..584B> (Journal Abbreviation: Meteorites and the Early Solar System II)
- Bretscher, A., Hermann, J., & Pettke, T. (2018, October). The influence of oceanic oxidation on serpentinite dehydration during subduction. *Earth and Planetary Science Letters*, 499, 173–184. Retrieved from <https://www.sciencedirect.com/science/article/pii/S0012821X18304230> doi: 10.1016/j.epsl.2018.07.017
- Běhouňková, M., Tobie, G., Choblet, G., Kervazo, M., Melwani Daswani, M., Dumoulin, C., & Vance, S. D. (2021, February). Tidally Induced Mag-

- matic Pulses on the Oceanic Floor of Jupiter's Moon Europa. *Geophysical Research Letters*, 48(3), e2020GL090077. Retrieved 2021-02-05, from <https://doi.org/10.1029/2020GL090077> (Publisher: John Wiley & Sons, Ltd) doi: 10.1029/2020GL090077
- Canup, R. M., & Ward, W. R. (2009). Origin of Europa and the Galilean satellites. In R. T. Pappalardo, W. B. McKinnon, & K. Khurana (Eds.), *Europa* (pp. 59–83). Tucson, AZ: University of Arizona Press.
- Cerpa, N. G., Padrón-Navarta, J. A., & Arcay, D. (2020, March). Uncertainties in the stability field of UHP hydrous phases (10-A phase and phase E) and deep-slab dehydration: potential implications for fluid migration and water fluxes at subduction zones.. Retrieved 2021-04-04, from <https://meetingorganizer.copernicus.org/EGU2020/EGU2020-4783.html> doi: 10.5194/egusphere-egu2020-4783
- Chatterjee, N. D., & Froese, E. (1975, December). A thermodynamic study of the pseudobinary join muscovite-paragonite in the system $KAlSi_3O_8$ - $NaAlSi_3O_8$ - Al_2O_3 - SiO_2 - H_2O . *American Mineralogist*, 60(11-12), 985–993.
- Choblet, G., Tobie, G., Sotin, C., Kalousová, K., & Grasset, O. (2017, March). Heat transport in the high-pressure ice mantle of large icy moons. *Icarus*, 285, 252–262. Retrieved from <http://www.sciencedirect.com/science/article/pii/S0019103516302524> doi: 10.1016/j.icarus.2016.12.002
- Clay, P. L., Burgess, R., Busemann, H., Ruzié-Hamilton, L., Joachim, B., Day, J. M. D., & Ballentine, C. J. (2017, November). Halogens in chondritic meteorites and terrestrial accretion. *Nature*, 551(7682), 614–618. Retrieved from <https://doi.org/10.1038/nature24625> doi: 10.1038/nature24625
- Connolly, J. A. D. (2005). Computation of phase equilibria by linear programming: A tool for geodynamic modeling and its application to subduction zone decarbonation. *Earth and Planetary Science Letters*, 236(1-2), 524–541. Retrieved 2018-08-08, from <http://linkinghub.elsevier.com/retrieve/pii/S0012821X05002839> doi: 10.1016/j.epsl.2005.04.033
- Connolly, J. A. D. (2009). The geodynamic equation of state: What and how. *Geochemistry, Geophysics, Geosystems*, 10(10). Retrieved 2018-03-22, from <https://agupubs.onlinelibrary.wiley.com/doi/abs/10.1029/2009GC002540> doi: 10.1029/2009GC002540
- Connolly, J. A. D., & Galvez, M. E. (2018). Electrolytic fluid speciation by Gibbs energy minimization and implications for subduction zone mass transfer. *Earth and Planetary Science Letters*, 501, 90–102. Retrieved 2019-01-07, from <https://linkinghub.elsevier.com/retrieve/pii/S0012821X18304904> doi: 10.1016/j.epsl.2018.08.024
- Connolly, J. A. D., & Podladchikov, Y. Y. (1998, March). Compaction-driven fluid flow in viscoelastic rock. *Geodinamica Acta*, 11(2-3), 55–84. Retrieved from <https://www.tandfonline.com/doi/abs/10.1080/09853111.1998.11105311> (Publisher: Taylor & Francis) doi: 10.1080/09853111.1998.11105311
- Craddock, R. A., & Greeley, R. (2009, December). Minimum estimates of the amount and timing of gases released into the martian atmosphere from volcanic eruptions. *Icarus*, 204(2), 512–526. Retrieved from <http://www.sciencedirect.com/science/article/pii/S001910350900311X> doi: 10.1016/j.icarus.2009.07.026
- Day, J. M., Corder, C. A., Assayag, N., & Cartigny, P. (2019). Ferrous oxide-rich asteroid achondrites. *Geochimica et Cosmochimica Acta*. Retrieved from <http://www.sciencedirect.com/science/article/pii/S0016703719302121> doi: 10.1016/j.gca.2019.04.005
- Desch, S. J., Kalyaan, A., & Alexander, C. M. O. (2018). The Effect of Jupiter's Formation on the Distribution of Refractory Elements and Inclusions in Me-

- teorites. *The Astrophysical Journal Supplement Series*, 238(1), 11. Retrieved from <http://stacks.iop.org/0067-0049/238/i=1/a=11>
- Dhooghe, F., De Keyser, J., Altwegg, K., Briois, C., Balsiger, H., Berthelier, J.-J., ... Wurz, P. (2017, December). Halogens as tracers of protosolar nebula material in comet 67P/Churyumov–Gerasimenko. *Monthly Notices of the Royal Astronomical Society*, 472(2), 1336–1345. Retrieved 2020-06-25, from <http://academic.oup.com/mnras/article/472/2/1336/4062198/Halogens-as-tracers-of-protosolar-> doi: 10.1093/mnras/stx1911
- Erkaev, N., Lammer, H., Elkins-Tanton, L., Stökl, A., Odert, P., Marcq, E., ... Güdel, M. (2014, August). Escape of the martian protoatmosphere and initial water inventory. *Planetary evolution and life*, 98, 106–119. Retrieved from <http://www.sciencedirect.com/science/article/pii/S0032063313002353> doi: 10.1016/j.pss.2013.09.008
- Estrada, P. R., Mosqueira, I., Lissauer, J. J., D’Angelo, G., & Cruikshank, D. (2009). Formation of Jupiter and conditions for accretion of the Galilean satellites. In R. T. Pappalardo, W. B. McKinnon, & K. Khurana (Eds.), *Europa* (pp. 27–58). Tucson, AZ: University of Arizona Press.
- Ferrand, T. P., Hilaret, N., Incel, S., Deldicque, D., Labrousse, L., Gasc, J., ... Schubnel, A. (2017, May). Dehydration-driven stress transfer triggers intermediate-depth earthquakes. *Nature Communications*, 8(1), 15247. Retrieved from <https://doi.org/10.1038/ncomms15247> doi: 10.1038/ncomms15247
- Flynn, G. J., Consolmagno, G. J., Brown, P., & Macke, R. J. (2018, September). Physical properties of the stone meteorites: Implications for the properties of their parent bodies. *Geochemistry*, 78(3), 269–298. Retrieved 2020-06-25, from <https://linkinghub.elsevier.com/retrieve/pii/S0009281916302860> doi: 10.1016/j.chemer.2017.04.002
- Fowler, A. P., Zierenberg, R. A., Reed, M. H., Palandri, J., Óskarsson, F., & Gunnarsson, I. (2019, January). Rare earth element systematics in boiled fluids from basalt-hosted geothermal systems. *Geochimica et Cosmochimica Acta*, 244, 129–154. Retrieved from <http://www.sciencedirect.com/science/article/pii/S0016703718305751> doi: 10.1016/j.gca.2018.10.001
- Fredriksson, K., & Kerridge, J. F. (1988, March). Carbonates and sulfates in CI chondrites - Formation by aqueous activity on the parent body. *Meteoritics*, 23, 35–44.
- Freedman, A. J. E., Bird, D. K., Arnorsson, S., Fridriksson, T., Elders, W. A., & Fridleifsson, G. O. (2009, November). Hydrothermal minerals record CO₂ partial pressures in the Reykjanes geothermal system, Iceland. *American Journal of Science*, 309(9), 788–833. Retrieved 2020-10-13, from <http://www.ajsonline.org/cgi/doi/10.2475/09.2009.02> doi: 10.2475/09.2009.02
- Frost, B. R. (1991, December). Chapter 1. Introduction to oxygen fugacity and its petrological importance. In D. H. Lindsley (Ed.), *Oxide Minerals* (pp. 1–10). Berlin, Boston: De Gruyter. Retrieved 2021-03-19, from <https://www.degruyter.com/document/doi/10.1515/9781501508684-004/html> doi: 10.1515/9781501508684-004
- García-Arias, M. (2020, December). Consistency of the activity–composition models of Holland, Green, and Powell (2018) with experiments on natural and synthetic compositions: A comparative study. *Journal of Metamorphic Geology*, 38(9), 993–1010. Retrieved 2021-04-05, from <https://doi.org/10.1111/jmg.12557> (Publisher: John Wiley & Sons, Ltd) doi: 10.1111/jmg.12557
- Gorce, J., Caddick, M., & Bodnar, R. (2019, August). Thermodynamic constraints on carbonate stability and carbon volatility during subduction.

- Earth and Planetary Science Letters*, 519, 213–222. Retrieved from <https://www.sciencedirect.com/science/article/pii/S0012821X19302596>
doi: 10.1016/j.epsl.2019.04.047
- Gounelle, M., & Zolensky, M. E. (2001, October). A terrestrial origin for sulfate veins in CI1 chondrites. *Meteoritics & Planetary Science*, 36(10), 1321–1329. Retrieved 2020-04-06, from <https://doi.org/10.1111/j.1945-5100.2001.tb01827.x> (Publisher: John Wiley & Sons, Ltd) doi: 10.1111/j.1945-5100.2001.tb01827.x
- Green, E., Holland, T. J. B., & Powell, R. (2007, July). An order-disorder model for omphacitic pyroxenes in the system jadeite-diopside-hedenbergite-acmite, with applications to eclogitic rocks. *American Mineralogist*, 92(7), 1181–1189. Retrieved 2020-06-27, from <https://pubs.geoscienceworld.org/ammin/article/92/7/1181-1189/134540>
doi: 10.2138/am.2007.2401
- Hansen, G. B., & McCord, T. B. (2008, January). Widespread CO₂ and other non-ice compounds on the anti-Jovian and trailing sides of Europa from Galileo/NIMS observations. *Geophysical Research Letters*, 35(1). Retrieved 2020-10-08, from <https://doi.org/10.1029/2007GL031748> (Publisher: John Wiley & Sons, Ltd) doi: 10.1029/2007GL031748
- Holland, T. J. B., Baker, J., & Powell, R. (1998, 06). Mixing properties and activity-composition relationships of chlorites in the system mgo-feo-al₂o₃-sio₂-h₂o. *European Journal of Mineralogy*, 10(3), 395-406. Retrieved from <http://dx.doi.org/10.1127/ejm/10/3/0395> doi: 10.1127/ejm/10/3/0395
- Holland, T. J. B., Green, E. C. R., & Powell, R. (2018, May). Melting of Peridotites through to Granites: A Simple Thermodynamic Model in the System KNCF-MASHTOCr. *Journal of Petrology*, 59(5), 881–900. Retrieved 2019-01-07, from <https://academic.oup.com/petrology/article/59/5/881/4996852>
doi: 10.1093/petrology/egy048
- Hussmann, H., & Spohn, T. (2004). Thermal-orbital evolution of Io and Europa. *Icarus*, 171(2), 391 - 410. Retrieved from <http://www.sciencedirect.com/science/article/pii/S0019103504001952>
doi: <https://doi.org/10.1016/j.icarus.2004.05.020>
- Jennings, E. S., Holland, T. J. B., Shorttle, O., Maclennan, J., & Gibson, S. A. (2016, December). The Composition of Melts from a Heterogeneous Mantle and the Origin of Ferropicrite: Application of a Thermodynamic Model. *Journal of Petrology*, egw065. Retrieved 2020-06-27, from <https://academic.oup.com/petrology/article-lookup/doi/10.1093/petrology/egw065>
doi: 10.1093/petrology/egw065
- Jia, X., Kivelson, M. G., Khurana, K. K., & Kurth, W. S. (2018, June). Evidence of a plume on Europa from Galileo magnetic and plasma wave signatures. *Nature Astronomy*, 2(6), 459–464. Retrieved from <https://doi.org/10.1038/s41550-018-0450-z> doi: 10.1038/s41550-018-0450-z
- Kalousová, K., & Sotin, C. (2020, September). Dynamics of Titan’s high-pressure ice layer. *Earth and Planetary Science Letters*, 545, 116416. Retrieved from <http://www.sciencedirect.com/science/article/pii/S0012821X20303605>
doi: 10.1016/j.epsl.2020.116416
- Kuramoto, K., & Matsui, T. (1994, October). Formation of a hot proto-atmosphere on the accreting giant icy satellite: Implications for the origin and evolution of Titan, Ganymede, and Callisto. *Journal of Geophysical Research: Planets*, 99(E10), 21183–21200. Retrieved 2021-01-29, from <https://doi.org/10.1029/94JE01864> (Publisher: John Wiley & Sons, Ltd) doi: 10.1029/94JE01864
- Kuskov, O., & Kronrod, V. (2005). Internal structure of Europa and Callisto. *Icarus*, 177(2), 550 - 569. Retrieved from

- <http://www.sciencedirect.com/science/article/pii/S0019103505001806>
doi: <https://doi.org/10.1016/j.icarus.2005.04.014>
- Lammer, H., Chassefière, E., Karatekin, O., Morschhauser, A., Niles, P. B., Mousis, O., ... Pham, L. (2013, January). Outgassing History and Escape of the Martian Atmosphere and Water Inventory. *Space Science Reviews*, 174(1-4), 113–154. Retrieved from <http://dx.doi.org/10.1007/s11214-012-9943-8>
doi: 10.1007/s11214-012-9943-8
- Lammer, H., Selsis, F., Chassefière, E., Breuer, D., Grießmeier, J.-M., Kulikov, Y. N., ... White, G. J. (2010, January). Geophysical and Atmospheric Evolution of Habitable Planets. *Astrobiology*, 10(1), 45–68. Retrieved 2021-04-13, from <http://www.liebertpub.com/doi/10.1089/ast.2009.0368> doi: 10.1089/ast.2009.0368
- Leclère, H., Faulkner, D., Llana-Fúnez, S., Bedford, J., & Wheeler, J. (2018, August). Reaction fronts, permeability and fluid pressure development during dehydration reactions. *Earth and Planetary Science Letters*, 496, 227–237. Retrieved 2020-06-26, from <https://linkinghub.elsevier.com/retrieve/pii/S0012821X18302759>
doi: 10.1016/j.epsl.2018.05.005
- Le Roy, L., Altwegg, K., Balsiger, H., Berthelier, J.-J., Bieler, A., Briois, C., ... Tzou, C.-Y. (2015, November). Inventory of the volatiles on comet 67P/Churyumov-Gerasimenko from Rosetta/ROSINA. *Astronomy & Astrophysics*, 583, A1. Retrieved 2020-06-25, from <http://www.aanda.org/10.1051/0004-6361/201526450> doi: 10.1051/0004-6361/201526450
- Li, J., & Fei, Y. (2014). 3.15 - Experimental constraints on core composition. In H. D. Holland & K. K. Turekian (Eds.), *Treatise on geochemistry* (Second ed., p. 527 - 557). Oxford: Elsevier. Retrieved from <http://www.sciencedirect.com/science/article/pii/B978008095975700214X>
doi: <https://doi.org/10.1016/B978-0-08-095975-7.00214-X>
- Lodders, K., & Fegley, B. (1998). *The planetary scientist's companion*. New York: Oxford University Press.
- Lunine, J. I., & Nolan, M. C. (1992, November). A massive early atmosphere on Triton. *Icarus*, 100(1), 221–234. Retrieved from <http://www.sciencedirect.com/science/article/pii/0019103592900312>
doi: 10.1016/0019-1035(92)90031-2
- Mayne, M. J., Moya, J.-F., Stevens, G., & Kaislaniemi, L. (2016, May). Rcrust: a tool for calculating path-dependent open system processes and application to melt loss. *Journal of Metamorphic Geology*, 34(7), 663–682. Retrieved 2018-07-25, from <https://doi.org/10.1111/jmg.12199> doi: 10.1111/jmg.12199
- McCord, T. B., Hansen, G. B., Fanale, F. P., Carlson, R. W., Matson, D. L., Johnson, T. V., ... Granahan, J. C. (1998, May). Salts on Europa's Surface Detected by Galileo's Near Infrared Mapping Spectrometer. *Science*, 280(5367), 1242. Retrieved from <http://science.sciencemag.org/content/280/5367/1242.abstract> doi: 10.1126/science.280.5367.1242
- McCord, T. B., Hansen, G. B., Matson, D. L., Johnson, T. V., Crowley, J. K., Fanale, F. P., ... Ocampo, A. (1999, May). Hydrated salt minerals on Europa's surface from the Galileo near-infrared mapping spectrometer (NIMS) investigation. *Journal of Geophysical Research: Planets*, 104(E5), 11827–11851. Retrieved 2020-10-08, from <https://doi.org/10.1029/1999JE900005> (Publisher: John Wiley & Sons, Ltd) doi: 10.1029/1999JE900005
- McKinnon, W. B., & Zolensky, M. E. (2003). Sulfate Content of Europa's Ocean and Shell: Evolutionary Considerations and Some Geological and Astrobiological Implications. *Astrobiology*, 3(4), 879–897. Retrieved 2020-04-06, from <https://doi.org/10.1089/153110703322736150> (Publisher: Mary Ann

- Liebert, Inc., publishers) doi: 10.1089/15311070322736150
- Menzel, M. D., Garrido, C. J., & López Sánchez-Vizcaíno, V. (2020, February). Fluid-mediated carbon release from serpentinite-hosted carbonates during dehydration of antigorite-serpentinite in subduction zones. *Earth and Planetary Science Letters*, 531, 115964. Retrieved from <https://www.sciencedirect.com/science/article/pii/S0012821X19306569> doi: 10.1016/j.epsl.2019.115964
- Miller, S., van der Zee, W., Olgaard, D., & Connolly, J. (2003, July). A fluid-pressure feedback model of dehydration reactions: experiments, modelling, and application to subduction zones. *Physical Properties of Rocks and other Geomaterials, a Special Volume to honour Professor H. Kern*, 370(1), 241–251. Retrieved from <http://www.sciencedirect.com/science/article/pii/S0040195103001896> doi: 10.1016/S0040-1951(03)00189-6
- Nozaka, T., Wintsch, R. P., & Meyer, R. (2017, June). Serpentinization of olivine in troctolites and olivine gabbros from the Hess Deep Rift. *Lithos*, 282–283, 201–214. Retrieved from <https://www.sciencedirect.com/science/article/pii/S0024493716304674> doi: 10.1016/j.lithos.2016.12.032
- Odert, P., Lammer, H., Erkaev, N., Nikolaou, A., Lichtenegger, H., Johnstone, C., ... Tosi, N. (2018, June). Escape and fractionation of volatiles and noble gases from Mars-sized planetary embryos and growing protoplanets. *Icarus*, 307, 327–346. Retrieved from <http://www.sciencedirect.com/science/article/pii/S0019103517301677> doi: 10.1016/j.icarus.2017.10.031
- Padrón-Navarta, J. A., Sánchez-Vizcaíno, V. L., Hermann, J., Connolly, J. A., Garrido, C. J., Gómez-Pugnaire, M. T., & Marchesi, C. (2013, September). Tschermak’s substitution in antigorite and consequences for phase relations and water liberation in high-grade serpentinites. *Serpentinites from mid-oceanic ridges to subduction*, 178, 186–196. Retrieved from <http://www.sciencedirect.com/science/article/pii/S0024493713000327> doi: 10.1016/j.lithos.2013.02.001
- Palandri, J. L., & Reed, M. H. (2004, March). Geochemical models of metasomatism in ultramafic systems: serpentinization, rodingitization, and sea floor carbonate chimney precipitation. *Geochimica et Cosmochimica Acta*, 68(5), 1115–1133. Retrieved from <http://www.sciencedirect.com/science/article/pii/S0016703703005921> doi: 10.1016/j.gca.2003.08.006
- Palme, H., Lodders, K., & Jones, A. (2014, January). 2.2 - Solar System Abundances of the Elements. In H. D. Holland & K. K. Turekian (Eds.), *Treatise on Geochemistry (Second Edition)* (pp. 15–36). Oxford: Elsevier. Retrieved from <http://www.sciencedirect.com/science/article/pii/B9780080959757001182> doi: 10.1016/B978-0-08-095975-7.00118-2
- Pan, D., Spanu, L., Harrison, B., Sverjensky, D. A., & Galli, G. (2013, April). Dielectric properties of water under extreme conditions and transport of carbonates in the deep Earth. *Proceedings of the National Academy of Sciences*, 110(17), 6646. Retrieved from <http://www.pnas.org/content/110/17/6646.abstract> doi: 10.1073/pnas.1221581110
- Pätzold, M., Andert, T., Hahn, M., Asmar, S. W., Barriot, J.-P., Bird, M. K., ... Scholten, F. (2016, February). A homogeneous nucleus for comet 67P/Churyumov–Gerasimenko from its gravity field. *Nature*, 530(7588), 63–65. Retrieved 2020-06-25, from <http://www.nature.com/articles/nature16535> doi: 10.1038/nature16535
- Pitzer, K. S., & Sterner, S. M. (1994, August). Equations of state valid con-

- tinuously from zero to extreme pressures for H₂O and CO₂. *The Journal of Chemical Physics*, 101(4), 3111–3116. Retrieved 2021-04-13, from <http://aip.scitation.org/doi/10.1063/1.467624> doi: 10.1063/1.467624
- Prieto-Ballesteros, O., Kargel, J. S., Fernández-Sampedro, M., Selsis, F., Martínez, E. S., & Hogenboom, D. L. (2005, October). Evaluation of the possible presence of clathrate hydrates in Europa's icy shell or seafloor. *Europa Icy Shell*, 177(2), 491–505. Retrieved from <http://www.sciencedirect.com/science/article/pii/S0019103505001351> doi: 10.1016/j.icarus.2005.02.021
- Reed, M. H. (1998). Calculation of simultaneous chemical equilibria in aqueous-mineral-gas systems and its application to modeling hydrothermal processes. In J. P. Richards (Ed.), *Techniques in Hydrothermal Ore Deposits Geology* (Vol. 10, pp. 109–124). Littleton, CO: Society of Economic Geologists, Inc.
- Richard, G., Monnereau, M., & Rabinowicz, M. (2007, March). Slab dehydration and fluid migration at the base of the upper mantle: implications for deep earthquake mechanisms. *Geophysical Journal International*, 168(3), 1291–1304. Retrieved 2020-06-27, from <https://doi.org/10.1111/j.1365-246X.2006.03244.x> doi: 10.1111/j.1365-246X.2006.03244.x
- Ronnet, T., Mousis, O., & Vernazza, P. (2017). Pebble Accretion at the Origin of Water in Europa. *The Astrophysical Journal*, 845(2), 92. Retrieved 2018-12-18, from <http://stacks.iop.org/0004-637X/845/i=2/a=92?key=crossref.e075ce27e4a38f6e8b1624cbb3608530> doi: 10.3847/1538-4357/aa80e6
- Roth, L., Saur, J., Retherford, K. D., Strobel, D. F., Feldman, P. D., McGrath, M. A., & Nimmo, F. (2014, January). Transient Water Vapor at Europa's South Pole. *Science*, 343(6167), 171. Retrieved from <http://science.sciencemag.org/content/343/6167/171.abstract> doi: 10.1126/science.1247051
- Saxena, S., & Eriksson, G. (2015). Thermodynamics of Fe-S at ultra-high pressure. *Calphad*, 51, 202 - 205. Retrieved from <http://www.sciencedirect.com/science/article/pii/S0364591615300249> doi: <https://doi.org/10.1016/j.calphad.2015.09.009>
- Schubert, G., Sohl, F., & Hussmann, H. (2009). Interior of Europa. In R. T. Pappalardo, W. B. McKinnon, & K. Khurana (Eds.), *Europa* (pp. 353–367). Tucson: University of Arizona Press.
- Scott, H., Williams, Q., & Ryerson, F. (2002). Experimental constraints on the chemical evolution of large icy satellites. *Earth and Planetary Science Letters*, 203(1), 399 - 412. Retrieved from <http://www.sciencedirect.com/science/article/pii/S0012821X02008506> doi: [https://doi.org/10.1016/S0012-821X\(02\)00850-6](https://doi.org/10.1016/S0012-821X(02)00850-6)
- Singerling, S. A., & Brearley, A. J. (2018). Primary iron sulfides in CM and CR carbonaceous chondrites: Insights into nebular processes. *Meteoritics & Planetary Science*, 53(10), 2078–2106. Retrieved 2020-03-04, from <https://doi.org/10.1111/maps.13108> (Publisher: John Wiley & Sons, Ltd) doi: 10.1111/maps.13108
- Sloan, E. D., & Koh, C. A. (2008). *Clathrate hydrates of natural gases* (3. ed ed.) (No. 119). Boca Raton, FL: CRC Press, Taylor & Francis. (OCLC: 836511793)
- Sohl, F., Spohn, T., Breuer, D., & Nagel, K. (2002). Implications from galileo observations on the interior structure and chemistry of the galilean satellites. *Icarus*, 157(1), 104 - 119. Retrieved from <http://www.sciencedirect.com/science/article/pii/S0019103502968284> doi: <https://doi.org/10.1006/icar.2002.6828>
- Sonzogni, Y., Treiman, A. H., & Schwenzer, S. P. (2017). Serpentinite with

- and without brucite: A reaction pathway analysis of a natural serpentine in the Josephine ophiolite, California. *Journal of Mineralogical and Petrological Sciences*, 112(2), 59–76. Retrieved 2021-04-14, from <https://www.jstage.jst.go.jp/article/jmps/112/2/112-160509/-article> doi: 10.2465/jmps.160509
- Sotin, C., Grasset, O., & Mocquet, A. (2007). Mass-radius curve for extrasolar Earth-like planets and ocean planets. *Icarus*, 191(1), 337–351. Retrieved 2018-10-23, from <http://linkinghub.elsevier.com/retrieve/pii/S0019103507001601> doi: 10.1016/j.icarus.2007.04.006
- Sotin, C., & Tobie, G. (2004). Internal structure and dynamics of the large icy satellites. *Comptes Rendus Physique*, 5(7), 769 - 780. Retrieved from <http://www.sciencedirect.com/science/article/pii/S163107050400146X> doi: <https://doi.org/10.1016/j.crhy.2004.08.001>
- Sparks, W. B., Hand, K. P., McGrath, M. A., Bergeron, E., Cracraft, M., & Deustua, S. E. (2016, September). Probing for evidence of plumes on Europa with HST/STIS. *The Astrophysical Journal*, 829(2), 121. Retrieved from <http://dx.doi.org/10.3847/0004-637X/829/2/121> (Publisher: American Astronomical Society) doi: 10.3847/0004-637x/829/2/121
- Steenstra, E. S., & van Westrenen, W. (2018). A synthesis of geochemical constraints on the inventory of light elements in the core of Mars. *Icarus*, 315, 69 - 78. Retrieved from <http://www.sciencedirect.com/science/article/pii/S0019103518302045> doi: <https://doi.org/10.1016/j.icarus.2018.06.023>
- Sverjensky, D. A., Harrison, B., & Azzolini, D. (2014, March). Water in the deep Earth: The dielectric constant and the solubilities of quartz and corundum to 60kb and 1200°C. *Geochimica et Cosmochimica Acta*, 129, 125–145. Retrieved from <http://www.sciencedirect.com/science/article/pii/S0016703713007151> doi: 10.1016/j.gca.2013.12.019
- Tian, F., Kasting, J. F., & Solomon, S. C. (2009, January). Thermal escape of carbon from the early Martian atmosphere. *Geophysical Research Letters*, 36(2). Retrieved 2021-04-03, from <https://doi.org/10.1029/2008GL036513> (Publisher: John Wiley & Sons, Ltd) doi: 10.1029/2008GL036513
- Tobie, G., Choblet, G., & Sotin, C. (2003). Tidally heated convection: Constraints on Europa’s ice shell thickness. *Journal of Geophysical Research: Planets*, 108(E11). Retrieved 2019-01-08, from <https://doi.org/10.1029/2003JE002099> doi: 10.1029/2003JE002099
- Tobie, G., Mocquet, A., & Sotin, C. (2005). Tidal dissipation within large icy satellites: Applications to Europa and Titan. *Europa Icy Shell*, 177(2), 534–549. Retrieved from <http://www.sciencedirect.com/science/article/pii/S0019103505001582> doi: 10.1016/j.icarus.2005.04.006
- Vance, S. D., Panning, M. P., Stähler, S., Cammarano, F., Bills, B. G., Tobie, G., ... Banerdt, B. (2018). Geophysical investigations of habitability in ice-covered ocean worlds. *Journal of Geophysical Research: Planets*, 123(1), 180-205. Retrieved from <https://agupubs.onlinelibrary.wiley.com/doi/abs/10.1002/2017JE005341> doi: 10.1002/2017JE005341
- Verba, C., O’Connor, W., Rush, G., Palandri, J., Reed, M., & Ideker, J. (2014, April). Geochemical alteration of simulated wellbores of CO₂ injection sites within the Illinois and Pasco Basins. *International Journal of Greenhouse Gas Control*, 23, 119–134. Retrieved from <http://www.sciencedirect.com/science/article/pii/S1750583614000309> doi: 10.1016/j.ijggc.2014.01.015

- Walder, P., & Pelton, A. D. (2005). Thermodynamic modeling of the Fe-S system. *Journal of Phase Equilibria and Diffusion*, *26*(1), 23–38. Retrieved from <https://doi.org/10.1007/s11669-005-0055-y> doi: 10.1007/s11669-005-0055-y
- Warner, M. (2004, March). Free water and seismic reflectivity in the lower continental crust. *Journal of Geophysics and Engineering*, *1*(1), 88–101. Retrieved 2021-04-06, from <https://doi.org/10.1088/1742-2132/1/1/012> doi: 10.1088/1742-2132/1/1/012
- Wilson, C. R., Spiegelman, M., van Keken, P. E., & Hacker, B. R. (2014, September). Fluid flow in subduction zones: The role of solid rheology and compaction pressure. *Earth and Planetary Science Letters*, *401*, 261–274. Retrieved 2020-06-26, from <https://linkinghub.elsevier.com/retrieve/pii/S0012821X14003628> doi: 10.1016/j.epsl.2014.05.052
- Wood, B. J., Li, J., & Shahar, A. (2013). Carbon in the core: Its influence on the properties of core and mantle. *Reviews in Mineralogy and Geochemistry*, *75*(1), 231. Retrieved from <http://dx.doi.org/10.2138/rmg.2013.75.8> doi: 10.2138/rmg.2013.75.8
- Zhang, H. (2003). Internal structure models and dynamical parameters of the Galilean satellites. *Celestial Mechanics and Dynamical Astronomy*, *87*(1), 189–195. Retrieved from <https://doi.org/10.1023/A:1026188029324> doi: 10.1023/A:1026188029324
- Zolensky, M., Barrett, R., & Browning, L. (1993, July). Mineralogy and composition of matrix and chondrule rims in carbonaceous chondrites. *Geochimica et Cosmochimica Acta*, *57*(13), 3123–3148. Retrieved from <https://www.sciencedirect.com/science/article/pii/001670379390298B> doi: 10.1016/0016-7037(93)90298-B
- Zolotov, M. Y., & Kargel, J. S. (2009). On the chemical composition of Europa’s icy shell, ocean, and underlying rocks. In R. T. Pappalardo, W. B. McKinnon, & K. Khurana (Eds.), *Europa* (p. 431). University of Arizona Press Tucson, AZ. Retrieved from <https://uapress.arizona.edu/book/europa>